Hadron Production via e^+e^- Collisions with Initial State Radiation

V.P. Druzhinin, S.I. Eidelman, S.I. Serednyakov, E.P. Solodov

Budker Institute of Nuclear Physics SB RAS, Novosibirsk, 630090, Russia and Novosibirsk State University, Novosibirsk, 630090, Russia

A novel method of studying e^+e^- annihilation into hadrons using initial state radiation at e^+e^- colliders is described. After brief history of the method, its theoretical foundations are considered. Numerous experiments in which exclusive cross sections of e^+e^- annihilation into hadrons below the center-of-mass energy of 5 GeV have been measured are presented. Some applications of the results obtained to fundamental tests of the Standard Model are listed.

PACS numbers:

arXiv:1105.4975v2 [hep-ex] 12 Aug 2011

Contents

I. Introduction 2
- A. Why is low energy e^+e^- annihilation interesting? 2
- B. Idea of ISR 2
- C. Calculation of ISR and accuracy 3
- D. Monte Carlo generators 5

II. Experimental Techniques 5
- A. Tagged and untagged ISR 5
- B. Hadronic mass resolution and mass scale calibration 7
- C. ISR luminosity 8
- D. Comparison with e^+e^- scan 9
- E. Colliders and detectors using ISR 10
- F. PEP-II and BABAR 11
- G. KEKB and BELLE 11
- H. DAΦNE and KLOE 12

III. Production of light quark mesons 13
- A. Overview 13
- B. $e^+e^- \to \pi^+\pi^-$ 13
- C. $e^+e^- \to \pi^+\pi^-\pi^0$ 15
- D. $e^+e^- \to K^+K^-\pi^0$, $K^0_S K^\pm\pi^\mp$, $K^+K^-\eta$ 16
- E. $e^+e^- \to \pi^+\pi^-\pi^+\pi^-$, $\pi^+\pi^-2\pi^0$ 19
- F. $e^+e^- \to K^+K^-\pi^+\pi^-$, $K^+K^-\pi^0\pi^0$ 20
- G. $e^+e^- \to 2(K^+K^-)$ 24
- H. $e^+e^- \to 5$ mesons 24
- I. $e^+e^- \to 3(\pi^+\pi^-)$, $2(\pi^+\pi^-\pi^0)$ 29
- J. Summary 30

IV. Baryon form factors 31
- A. General formulae 31
- B. Measurement of time-like baryon form factors 33
- C. $e^+e^- \to p\bar{p}\gamma$ 33
- D. $e^+e^- \to \Lambda\bar{\Lambda}\gamma$ 33
- E. $e^+e^- \to \Sigma^0\bar{\Sigma}^0$, $\Lambda\bar{\Sigma}^0$ $(\Sigma^0\bar{\Lambda})$ 34
- F. Summary 35

V. Decays of the J/ψ and $\psi(2S)$ 36
- A. Leptonic decays 36
- B. Decays to light mesons and baryons 37

VI. ISR studies in the charmonium region 40
- A. Final states with open charm 41
- B. New charmonium-like states 42

VII. Some implications for theory and perspectives 43

VIII. Conclusions 47

Acknowledgments 47

References 47

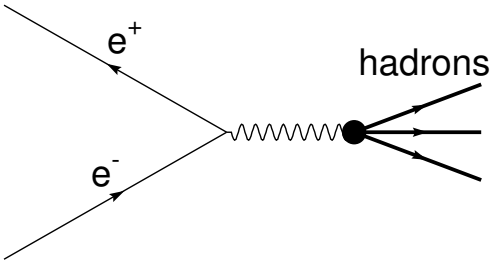


FIG. 1 The lowest-order Feynman diagram describing the process of e^+e^- annihilation into hadrons.

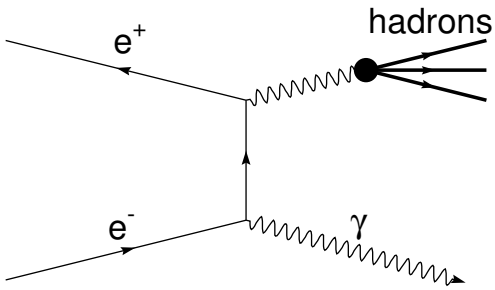


FIG. 2 The lowest-order Feynman diagram describing the initial state radiation process $e^+e^- \to \gamma+$ hadrons.

I. INTRODUCTION

A. Why is low energy e^+e^- annihilation interesting?

Studies of low energy e^+e^- annihilation into hadrons are of great interest for theory and have numerous applications. According to current concepts, e^+e^- annihilation into hadrons proceeds via an intermediate virtual photon which produces a pair of quarks, $q\bar{q}$, followed by the hadronization of quarks into observed hadrons. This process is described by the lowest-order Feynman diagram shown in Fig. 1. When the initial energy of e^+e^-, or equivalently of the intermediate virtual photon, is large enough, the process of hadronization is well described by Quantum Chromodynamics (QCD). At small energies, lower than 2–3 GeV, produced hadrons are relatively soft and intensively interact with each other forming hadronic resonances. At the moment QCD fails to describe this energy region. Because of that, it is vitally important to gain sufficient information from experiment to be used as an input to various QCD-based theoretical models. QCD sum rules are an example of how measurements of total and exclusive cross sections can be used to extract such fundamental parameters of theory as the strong coupling constant α_s, quark and gluon condensates (Shifman *et al.*, 2000).

Precise knowledge of vacuum polarization effects based on the total cross section of e^+e^- annihilation into hadrons is necessary to estimate the hadronic contributions to the running fine-structure constant and thus determine its value at the Z boson mass, $\alpha(M_Z^2)$, a key component of the high-precision tests of the Standard Model (Actis *et al.*, 2010; Burkhardt *et al.*, 1989; Burkhardt and Pietrzyk, 2005; Eidelman and Jegerlehner, 1995; Hagiwara *et al.*, 2003).

Improvement of the precision with which the total cross section of e^+e^- annihilation into hadrons is known is also needed for a more accurate estimation of the hadronic contribution to the muon anomalous magnetic moment since it is one of the crucial limiting factors in a search for New Physics (Bennett *et al.*, 2006; Bouchiat and Michel, 1961; Gourdin and de Rafael, 1969).

There is an important relation between spectral functions in e^+e^- annihilation into hadrons with isospin $I = 1$ and corresponding τ lepton decays based on conservation of vector current (CVC) and isospin symmetry (Thacker and Sakurai, 1971; Tsai, 1971). While first detailed tests of such relations showed satisfactory agreement between such spectral functions (Eidelman and Ivanchenko, 1991; Kawamoto and Sanda, 1978), higher accuracy reached in both e^+e^- and τ lepton sectors revealed possible systematic effects not accounted for in the e^+e^- and/or τ experiments (Davier *et al.*, 2003a,b). Understanding of these effects is crucial for improving the accuracy with which the hadronic contributions to the muon anomalous magnetic moment can be estimated from τ decays to two and four pions as was first suggested by (Alemany *et al.*, 1998).

Detailed measurements of the energy dependence of various exclusive cross sections allow to improve our knowledge of vector mesons and look for new states, both of light (Druzhinin, 2007) and heavy quarks (Eichten *et al.*, 2008).

B. Idea of ISR

In e^+e^- collider experiments exclusive and total hadronic cross sections are usually measured by scanning the accessible energy range. The process of e^+e^- annihilation is accompanied by emission of one or several photons from the initial state. The lowest-order Feynman diagram describing initial-state radiation (ISR) is shown in Fig. 2. The quantity measured directly in the experiment is the visible cross section

$$\sigma_{\rm vis} = \frac{N}{L}, \tag{1}$$

where N is the number of selected events of the process $e^+e^- \to$ hadrons $+ n\gamma$, $n = 0, 1, 2, \ldots$, and L is the integrated luminosity of the collider collected at the center-of-mass (c.m.) e^+e^- energy $2E_0$. The visible cross section can be related to the Born cross section σ_0 corresponding to the lowest-order diagram of Fig. 1 via the

integral (Kuraev and Fadin, 1985), providing the 10^{-3} accuracy:

$$\sigma_{\rm vis} = \int\limits_0^{1-m^2_{\rm min}/s} \varepsilon(s,x)W(s,x)\sigma_0(s(1-x))\mathrm{d}x, \qquad (2)$$

where $s = 4E_0^2$, x is an effective fraction of the beam energy E_0 carried by photons emitted from the initial state, $m_{\rm min}$ is the minimal possible invariant mass of the final hadrons, $\varepsilon(s,x)$ is the detection efficiency for the process $e^+e^- \to$ hadrons $+ n\gamma$ as a function of x and s. The so-called radiator function $W(s,x)$ taking into account higher-order QED contributions, in particular, from the diagram in Fig. 2, is fully calculable in QED (Actis *et al.*, 2010). Due to the photon emission from the initial state the visible cross section depends on the Born cross section at all energies below the nominal e^+e^- c.m. energy $2E_0$.

In conventional scanning experiments the influence of ISR is suppressed by the requirements of the energy and momentum balance between the final hadrons and the initial e^+e^- state. In this case the detection efficiency has x dependence close to the step function: $\varepsilon(s,x) = \varepsilon_0(s)$ for $x < x_0$, and zero for $x > x_0$. At small x_0, the equation (2) can be rewritten:

$$\sigma_{\rm vis} = \varepsilon_0(s)\sigma_0(s)(1+\delta(s)), \qquad (3)$$

where $1+\delta(s)$ is the radiative correction factor, which takes into account higher-order QED corrections. To calculate this factor it is necessary to know s dependence of σ_0 in the range from $s(1-x_0)$ to s. For slowly varying cross sections, δ is about 10%, and can be determined with accuracy better than 1% using existing data on the cross section energy dependence. Thus, in scanning experiments, from the data collected at the c.m. energy $\sqrt{s}$ the cross section $\sigma_0(s)$ is determined directly.

Another approach is also possible. Equation (2) can be rewritten in the differential form:

$$\frac{\mathrm{d}\sigma_{\rm vis}(s,m)}{\mathrm{d}m} = \frac{2m}{s}\varepsilon(s,m)W(s,x)\sigma_0(m), \qquad (4)$$

where we have made a transformation to the variable $m = \sqrt{s(1-x)}$, the invariant mass of the hadronic system. At non-zero x the dominant contribution to the visible cross section comes from the one-photon ISR (Fig. 2). With the inclusion of the ISR photon momentum into the selection conditions on the energy and momentum balance, the non-zero detection efficiency for ISR events can be obtained in a wide range of the hadronic invariant mass. So, from the measurement of the mass spectrum for the process $e^+e^- \to$ hadrons $+\,\gamma$ at fixed c.m. energy $\sqrt{s}$ the cross section $\sigma_0(m)$ can be extracted in the invariant mass range from threshold to the mass close to $\sqrt{s}$.

The idea of utilizing initial-state radiation from a high-mass state to explore electron-positron processes at all energies below that state was outlined long ago in Refs. (Baier and Fadin, 1968; Baier and Khoze, 1965). A possibility of exploiting such processes at high luminosity ϕ- and B-factories was discussed in Refs. (Arbuzov *et al.*, 1998; Benayoun *et al.*, 1999; Binner *et al.*, 1999; Konchatnij and Merenkov, 1999) and motivated studies described in this paper.

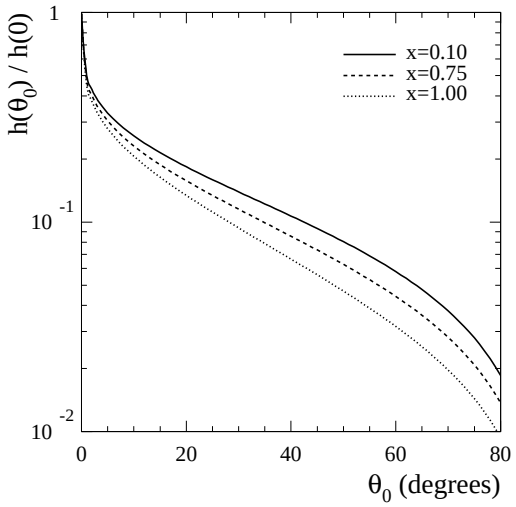


FIG. 3 The relative probability for the ISR photon to be emitted into the polar angle range $\theta_0 < \theta < 180^\circ - \theta_0$ for three representative values of x.

Analysis of ISR events at e^+e^--factories provides independent and contiguous measurements of hadronic cross sections in the low-energy region and also contributes to the spectroscopy of low-mass resonances.

C. Calculation of ISR and accuracy

In the lowest order (Fig. 2) the probability of the initial-state radiation of the photon with the energy xE_0 and the polar angle θ is as follows (Baier and Khoze, 1965; Bonneau and Martin, 1971):

$$w_0(\theta,x) = \frac{\alpha}{\pi x}\left[\frac{(1-x+\frac{x^2}{2})\sin^2\theta - \frac{x^2}{2}\sin^4\theta}{\left(\sin^2\theta + \frac{4m_e^2}{s}\cos^2\theta\right)^2} - \frac{4m_e^2}{s}\frac{(1-2x)\sin^2\theta - x^2\cos^4\theta}{\left(\sin^2\theta + \frac{4m_e^2}{s}\cos^2\theta\right)^2}\right], \qquad (5)$$

where α is the fine-structure constant, and m_e is the electron mass.

The ISR photon is predominantly emitted at small angles with respect to the beam axis. In Fig. 3 we present the dependence of the function $W_0(\theta_0,x)/W_0(0,x)$ on the

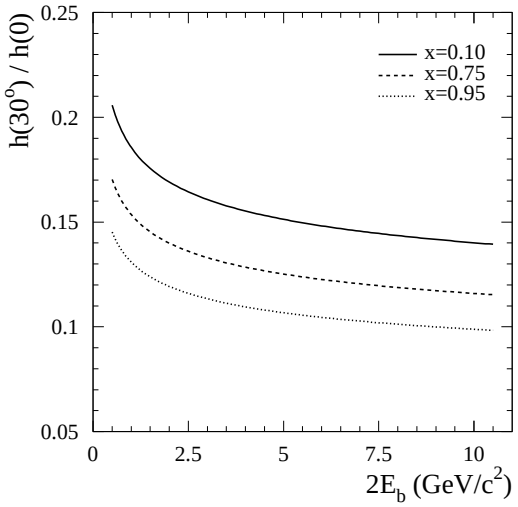


FIG. 4 The relative probability for the ISR photon to be emitted into the polar angle range $30^\circ < \theta < 150^\circ$ as a function of the e^+e^- c.m. energy for three representative values of x.

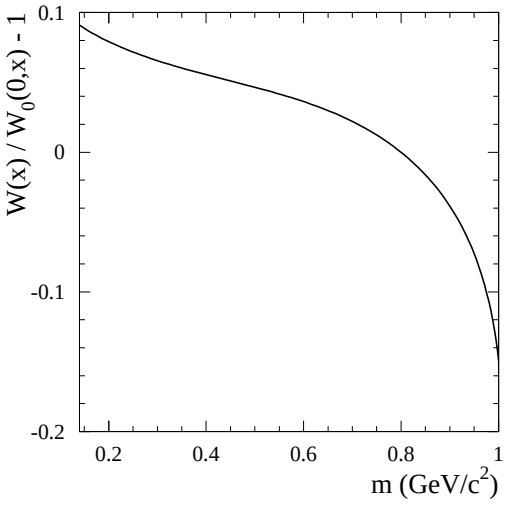


FIG. 5 The mass ($m = 2E_0\sqrt{1-x}$) dependence of the relative difference between the radiator function $W(x)$ from Ref. (Kuraev and Fadin, 1985) and the lowest-order function $W_0(0,x)$ for $2E_0 = 1.02$ GeV.

polar angle limit θ_0, where

$$W_0(\theta_0, x) = \int_{\theta_0}^{\pi-\theta_0} w_0(\theta, x) \sin\theta \mathrm{d}\theta. \qquad (6)$$

The integration is performed for three values of x at $2E_0 = 10.58$ GeV, the c.m. energy of B-factories. It can be seen that the angular distribution of the ISR photon weakly depends on x and that a considerable fraction of the photons is emitted at large angles. In the next section we will discuss two approaches to study ISR events, a tagged and untagged one. In the tagged approach the ISR photon should be detected, i.e., emitted at a large angle, into the fiducial volume of the detector. At B-factories ($2E_0 = 10.58$ GeV) about 10% of high-energy ISR photons have $30^\circ < \theta < 150^\circ$. This angular range approximately corresponds to the fiducial volume of the electromagnetic calorimeter of the BABAR detector. The fraction of the large-angle ISR increases with decrease of the energy as shown in Fig. 4. The compact expressions for W_0 can be written for two practically applicable cases. For the range of integration $\theta_0 < \theta < \pi - \theta_0$, $\theta_0 \gg m_e/\sqrt{s}$

$$W_0(\theta_0, x) = \frac{\alpha}{\pi x}\left[(2 - 2x + x^2)\ln\frac{1+\cos\theta_0}{1-\cos\theta_0} - x^2\cos\theta_0\right]. \qquad (7)$$

For the full range of polar angles $0 < \theta < \pi$

$$W_0(0, x) = \frac{\alpha}{\pi x}(\ln\frac{s}{m_e^2} - 1)(2 - 2x + x^2). \qquad (8)$$

The formulae given above describe ISR processes in the lowest QED order. To estimate a contribution of higher-order diagrams (loops and related to extra photon emission) the function $W(x)$ from Ref. (Kuraev and Fadin, 1985) can be used, which takes into account soft multiphoton emission and α^2 terms in the leading logarithmic approximation. In this approximation the accuracy $\Delta W/W$ is expected to be better than 1%. The relative difference between $W(x)$ and $W_0(0,x)$ as a function of the invariant mass of the final hadronic system is shown in Fig. 5 for $2E_0 = 1.02$ GeV, the c.m. energy of the ϕ-factory in Frascati. It is seen that the radiative correction to the lowest-order radiator function reaches 15%. It should be noted that the size of the radiation correction depends on experimental conditions. For example, in Ref. (Aubert *et al.*, 2006a) the function $W(x)$ is calculated at $2E_0 = 10.58$ GeV with conditions that the highest-energy ISR photon has a polar angle in the range $20^\circ < \theta < 160^\circ$ and that the invariant mass of the hadronic system combined with the ISR photon is greater than 8 GeV/c^2. The latter condition restricts the maximum energy of extra photons emitted from the initial state. With these conditions the radiative correction factor $1 + \delta = W(20^\circ, x)/W_0(20^\circ, x)$ is close to unity with the maximum deviation δ of about 2%.

To provide accuracy better than 1% required for the measurement of the exclusive hadronic cross sections at low energies, the calculation of the radiator function should include the higher-order radiative correction, in particular, due to emission of extra photons. Several theoretical papers are devoted to study radiative corrections to ISR processes, for example, (Arbuzov *et al.*, 1998; Binner *et al.*, 1999; Czyż *et al.*, 2003; Khoze *et al.*, 2001, 2002; Rodrigo *et al.*, 2002). The approaches of Refs. (Binner *et al.*, 1999; Czyż *et al.*, 2003; Rodrigo *et al.*, 2002) allow one to develop genera-

tors of Monte Carlo (MC) events and are used in analyses of experimental data. In Ref. (Binner *et al.*, 1999) the photon emission at large angles only is considered; radiative corrections are calculated in the leading logarithmic approximation with the structure function technique (Caffo *et al.*, 1994, 1997). The accuracy of the method is determined by neglecting sub-leading α^2 contributions and estimated in Ref. (Rodrigo *et al.*, 2001) to be about 1%. In Refs. (Czyż *et al.*, 2003; Rodrigo *et al.*, 2002) the one-loop corrections and exact matrix element for emission of two hard photons are calculated. The accuracy of this next-to-leading order (NLO) calculation is estimated to be about 0.5% (Rodrigo *et al.*, 2002) due to the higher-order effects.

D. Monte Carlo generators

The calculation of the radiator function is usually performed by the Monte Carlo method. A special computer code referred to as an "event generator" provides events (sets of the four-momenta of the final particles) distributed over the phase space according to the matrix element squared of the process under study. The phase space can be restricted by some conditions on the angles and energies of the generated ISR photons. These conditions should be looser than the actual experimental conditions used for event selection.

The interaction of the generated particles with the detector and the detector response are then simulated. In modern experiments the detector simulation is based on the GEANT4 (Agostinelli *et al.*, 2003) package. The simulated events are reconstructed with the program chain used for experimental data. The detection efficiency is determined as the ratio of the mass spectrum of simulated events that passed selection criteria to the spectrum of generated events.

Most of ISR analyses discussed in this paper are based on two event generators. Historically, EVA was the first ISR Monte Carlo generator. The AfkQed package used in the BABAR experiment at the SLAC B-factory is a development of the EVA generator (Binner *et al.*, 1999; Czyż and Kühn, 2001) initially designed to simulate ISR production of the 2π and 4π final states with an ISR photon emitted at large angles. The soft-photon radiation from the initial state is generated with the structure function method (Caffo *et al.*, 1994, 1997). Two extra photons are emitted in the directions of the initial electron and positron. The program has a modular structure allowing to implement easily new hadronic modes. The AfkQed package includes generation of 2π, 3π, 4π, 5π, 6π, $\eta\pi^+\pi^-$ states, modes with kaons $K\bar{K}+n\pi$ $n=0,1,2,3,4$, and protons $p\bar{p}$, $p\bar{p}2\pi$. The generation of the process $e^+e^-\to\mu^+\mu^-\gamma$ is also included into the AfkQed package. For this process both initial- and final-state radiation (FSR) diagrams and their interference are taken into account. For the charged particles the final-state radiation is generated using the PHOTOS package (Barberio *et al.*, 1991).

The Phokhara event generator is used in the BABAR and Belle experiments at the B-factories, and in the KLOE experiment at the ϕ-factory. Its latest version 6.1 (PHOKHARA web site, 2009) includes generation of the 2π, 3π, 4π, $K\bar{K}$, $p\bar{p}$, and $\Lambda\bar{\Lambda}$ hadronic states, and the process $e^+e^-\to\mu^+\mu^-\gamma$. The initial-state radiation is generated in NLO (Czyż *et al.*, 2003; Rodrigo *et al.*, 2002), i.e., one or two photons can be emitted by the initial electron and positron. The generator can be used for simulation of both tagged and untagged ISR measurements. For the processes $e^+e^-\to\mu^+\mu^-\gamma$, $e^+e^-\to\pi^+\pi^-\gamma$, and $e^+e^-\to K^+K^-\gamma$, NLO FSR radiative corrections are implemented. In particular, a hard ISR photon can be accompanied by emission of a soft photon from the final state.

For all the hadronic states except the two-body 2π and $K\bar{K}$ as well as $\pi^+\pi^-\pi^0$, the structure of the electromagnetic hadronic current entering the matrix element of the process $e^+e^-\to$ hadrons is model dependent and the object of a study by itself. This model dependence is the second source of the theoretical uncertainty. For most of the measurements of multihadron cross sections its contribution significantly exceeds the 0.5-1.0% uncertainty of the radiator function. To estimate the model uncertainty, the distributions of hadrons in data are compared to the corresponding simulated distributions. Usually, the difference between the detection efficiency obtained with different models of the hadronic currents is taken as an estimate of the model uncertainty.

II. EXPERIMENTAL TECHNIQUES

A. Tagged and untagged ISR

There are two approaches for studying ISR events. In the first approach, the untagged one, detection of the ISR photon is not required, but all the final hadrons must be detected and fully reconstructed. The ISR events are selected by the requirement that the recoil mass against the hadronic system be close to zero. The mass dependence of the detection efficiency for the process $e^+e^-\to\pi^+\pi^-\gamma$ at $2E_0=10.58$ GeV is shown in Fig. 6. The efficiency is calculated with the Phokhara event generator in leading-order mode. The detector acceptance for charged pions is assumed to be limited by the condition $30^\circ<\theta<150^\circ$ which corresponds to the polar angle coverage of the BABAR detector. The solid curve in Fig. 6 represents the efficiency for the case of untagged ISR photons. For two-pion masses below 3 GeV/c^2 the detection efficiency is about 10% and changes very slowly with mass. At these relatively low invariant masses, pions are produced in a narrow cone around the vector opposite to the ISR photon momentum and therefore can be detected only if the ISR photon is emitted at a large angle. The dotted curve in Fig. 6 represents the detection efficiency for the case of a tagged ISR photon. The photon polar angle is

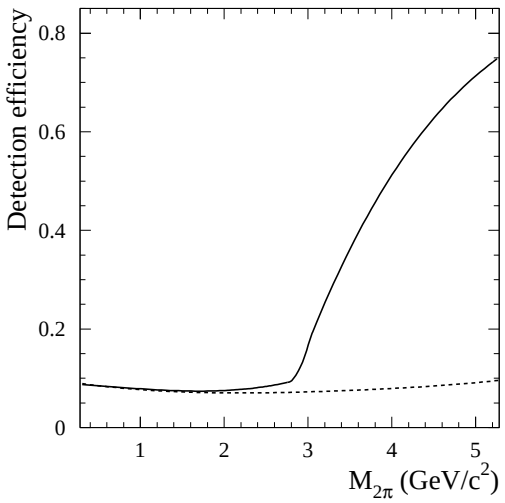


FIG. 6 The detection efficiency for the process $e^+e^- \to \pi^+\pi^-\gamma$ at $2E_0 = 10.58$ GeV as a function of the 2π invariant mass for untagged (solid curve) and tagged (dotted curve) ISR photons.

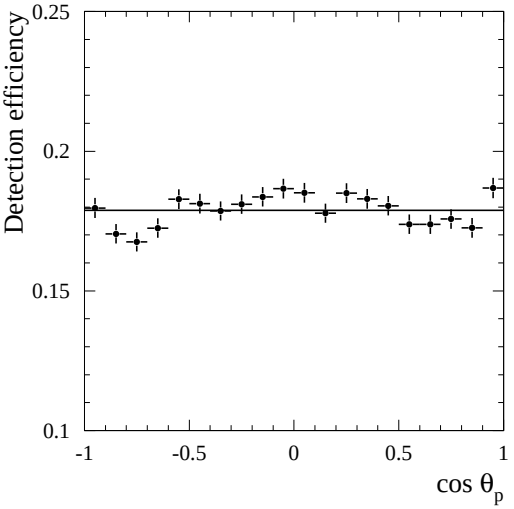


FIG. 7 The $\cos\theta_p$ dependence of the detection efficiency for the process $e^+e^- \to p\bar{p}\gamma$ (Aubert *et al.*, 2006a), where θ_p is the proton angle measured in the $p\bar{p}$ rest frame with respect to the ISR photon direction. The horizontal line indicates the detection efficiency averaged over $\cos\theta_p$.

required to be in the range from 30° to 150°. It is seen that tagged and untagged efficiencies are very close in the mass range below 3 GeV/c^2. For higher masses the small-angle ISR begins to contribute to the untagged efficiency leading to its rapid increase, whereas the efficiency for the case of a tagged ISR photon varies insignificantly.

At B-factories the untagged approach is used for measurements of exclusive cross sections for masses of produced hadronic systems above 3.5 GeV/c^2. The untagged detection efficiency is very sensitive to the angular distributions of the final hadrons. Therefore this approach is suitable for the measurement of hadronic processes with well defined dynamics, for example, $e^+e^- \to D\bar{D}$ or $e^+e^- \to D^*\bar{D}$. For multihadron final states this strong sensitivity to hadron angular distributions can lead to a sizeable systematic uncertainty of the measurement.

All measurements of exclusive cross sections of e^+e^- annihilation into light hadrons at B-factories were performed using the tagged approach. In contrast to the case of untagged ISR, the efficiency for events with a detected photon depends weakly on the angular distributions of the final hadrons. As an example, the angular dependence of the detection efficiency for the process $e^+e^- \to p\bar{p}\gamma$ (Aubert *et al.*, 2006a) is shown in Fig. 7, where θ_p is the proton angle in the $p\bar{p}$ rest frame measured with respect to the ISR photon direction. This advantage of the tagged ISR approach allows one to measure the cross section for multihadron final states with a relatively small model uncertainty.

Since ISR photons are emitted predominantly along the beam axis, in untagged ISR measurements the additional condition that $\cos\theta_\gamma$ is close to ± 1 can be used, where θ_γ is the polar angle of the momentum recoil against the hadronic system in the e^+e^- c.m. frame. In particular, in Refs. (Aloisio *et al.*, 2005; Ambrosino *et al.*, 2009) the condition $\theta_\gamma < 15°$ or $\theta_\gamma > 165°$ is used to select $e^+e^- \to \pi^+\pi^-\gamma$ events at the ϕ-factory. This condition allows to significantly reduce background from the decay $\phi \to 3\pi$ and almost completely remove the FSR background, i.e., $e^+e^- \to \pi^+\pi^-\gamma$ events with the photon emitted from the final state. It should be noted that the FSR contribution related to radiation by pions is negligible in B-factory experiments due to the smallness of the pion electromagnetic form factor at $s = 112$ GeV^2. At this energy, the structure-dependent contribution, for example, of the processes $e^+e^- \to f_0\gamma$ and $e^+e^- \to f_2\gamma$ is also expected to be small. Theoretical estimations for the cross sections of these processes at large s are absent in literature. An estimate was made for the process $e^+e^- \to p\bar{p}$ in Ref.(Aubert,2006a). The FSR contribution (including a structure-dependent part) was found to be less than 10^{-3} for the $p\bar{p}$ mass below 4.5 GeV. The detection efficiency for the process $e^+e^- \to \pi^+\pi^-\gamma$ at $2E_0 = 1.02$ GeV with the condition on θ_γ described above is shown in Fig. 8. The pion polar angles are required to be in the range 50°–130°. Due to this restriction the detection efficiency falls rapidly with decreasing 2π mass. The untagged approach was used in Refs. (Aloisio *et al.*, 2005; Ambrosino *et al.*, 2009) to measure the $e^+e^- \to \pi^+\pi^-$ cross section in the mass range from 0.592 to 0.975 GeV. The tagged approach allows one to access the near-threshold mass region. The detection efficiency for $\pi^+\pi^-\gamma$ events with a detected photon ($50° < \theta_\gamma < 130°$) is shown in Fig. 8 by the dashed curve. This selection was also used in the KLOE experiment (Ambrosino *et al.*, 2011; Muller, 2009) and allowed to reduce the lower mass boundary for the

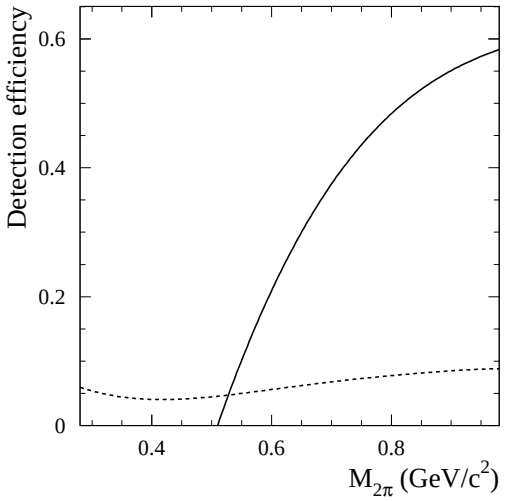


FIG. 8 The mass dependence of the detection efficiency for the process $e^+e^- \to \pi^+\pi^-\gamma$ at $2E_0 = 1.02$ GeV for two selections, untagged ($\theta_\gamma < 15^\circ$ or $\theta_\gamma > 165^\circ$) and tagged ($50^\circ < \theta_\gamma < 130^\circ$), shown by the solid and dashed curves, respectively. The pion polar angles range from 50° to 130°.

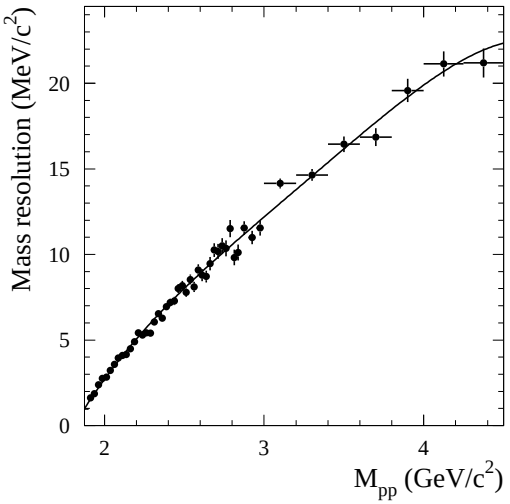


FIG. 9 The mass dependence of the $p\bar{p}$ mass resolution obtained from MC simulation for the process $e^+e^- \to p\bar{p}\gamma$ in Ref. (Aubert *et al.*, 2006a). The curve represents the result of a polynomial fit.

cross section measurement from 0.592 to 0.316 GeV.

B. Hadronic mass resolution and mass scale calibration

The detector resolution on the hadronic invariant mass and the accuracy of the mass scale calibration are important experimental parameters for the ISR cross section measurements.

The mass resolution σ_m is usually determined using MC simulation as RMS of the $(m_{\rm meas} - m_{\rm true})$ distribution, where $m_{\rm meas}$ and $m_{\rm true}$ are the measured and generated invariant masses, respectively. The experimental value of the mass resolution can be extracted from the fit of the measured line shape of a narrow resonance, for example, J/ψ.

In general, the invariant mass can be represented as a sum of the two terms: $m_{\rm meas} = \Sigma_i m_i + \Delta m(\vec{p_1}, \vec{p_2}, \ldots)$, where m_i are masses of stable hadrons produced in the process under study, and Δm is the term depending on the final particle momenta $\vec{p_i}$. The mass resolution σ_m is determined by the precision of the measurement of the momenta of the charged hadron tracks and photons from π^0 decays. Since $\Sigma_i m_i$ has no sizeable spread, and the Δm term and its uncertainty are minimal near threshold and grow with the mass increase, it is expected that σ_m also increases with mass. As an example, the mass resolution versus the proton-antiproton mass for the ISR process $e^+e^- \to p\bar{p}\gamma$ (Aubert *et al.*, 2006a) is shown in Fig.9.

At B-factories the mass resolution for multihadron systems consisting of light quarks varies from 4–7 MeV/c^2 at the mass of 1.5 GeV/c^2 to 6–11 MeV/c^2 at 3 GeV/c^2; the worse values are for hadron states with neutral pions. The hadronic cross sections in the mass region between the ϕ- and J/ψ-meson resonances do not contain structures with a width comparable to the detector resolution. The 25-MeV/c^2 mass bin was chosen for a study of most of the processes with light hadrons. With such a bin size the distortion of the mass spectrum shape because of resolution effects is small. A smaller bin size was used for analyses of the processes $e^+e^- \to p\bar{p}\gamma$ and $e^+e^- \to \pi^+\pi^-\gamma$. For the former, it is important to study a near-threshold enhancement in the mass dependence of the proton electromagnetic form factor. The good $p\bar{p}$ mass resolution for masses below 2 GeV/c^2 (see Fig.9) allows to measure the cross section in this region with the 5 MeV/c^2 mass bin (Aubert *et al.*, 2006a). The $e^+e^- \to \pi^+\pi^-$ cross section near the ρ-meson peak was measured in the BABAR experiment with the mass interval of 2 MeV/c^2 (Aubert *et al.*, 2009a), which is significantly smaller than the $\pi^+\pi^-$ mass resolution (about 6 MeV/c^2 at the ρ peak). The unfolding of resolution effects from the high-statistics (about one-half million events) mass spectrum was performed with the procedure described in Ref. (Malaescu, 2009). The procedure uses a mass-transfer matrix that gives the probability that an event with true mass in an interval i is reconstructed with $m_{\rm meas}$ in interval j. The transfer matrix is usually obtained using MC simulation and corrected to take into account a difference in the resolution between data and simulation.

The measurement of the $e^+e^- \to \pi^+\pi^-$ cross section at the ϕ-factory (Ambrosino *et al.*, 2009) with the KLOE detector was performed with the 0.01 GeV^2 step in the squared mass $s' = m^2_{2\pi}$ corresponding to a mass bin width of 6.5 MeV/c^2 near the ρ peak. The mass reso-

lution of the KLOE detector is about 1.3 MeV/c^2 at the ρ mass. The resolution effects are substantial only in the mass region of the ω-ρ interference. For comparison with theory, these effects were removed by unfolding the mass spectrum using the Bayesian method (D'Agostini, 1995).

For the J/ψ and $\psi(2S)$ produced in ISR processes the observed line shapes are fully determined by the detector resolution. In this case better mass resolution leads to the larger signal-to-background ratio. For the process $e^+e^- \to 2(\pi^+\pi^-)\pi^0\gamma$ (Aubert *et al.*, 2007c) in the mass region of the J/ψ and $\psi(2S)$ mesons discussed in Section V, the value of the mass resolution obtained from the fit to the J/ψ spectrum is about 9 MeV/c^2, in good agreement with MC simulation.

For the final states containing charmed and charmonium mesons ($J/\psi\pi^+\pi^-$, $D\bar{D}$, ...), the typical resolution in the 4–5 GeV/c^2 mass range is about 5 MeV/c^2. The corresponding cross sections were measured with the 20-25 MeV/c^2 mass bin. For these final states the influence of the limited mass resolution on the cross section measurement is negligible.

The precision of the absolute mass scale calibration can be tested by comparison of the measured mass values for known resonances with their nominal values. For many multihadron states (see Sec. V) the mass calibration is performed at the J/ψ mass. The difference between the measured and nominal (Eidelman *et al.*, 2004) J/ψ masses is found to be less than 1 MeV/c^2 (see, for example, Refs. (Aubert *et al.*, 2007c, 2008b)). For the 3π final state the mass scale shift was determined at the ω- and ϕ-meson masses (Aubert *et al.*, 2004b): $m_\omega - m_\omega^{\rm nominal} = -(0.2 \pm 0.1)$ MeV/c^2 and $m_\phi - m_\phi^{\rm nominal} = -(0.6 \pm 0.2)$ MeV/c^2. We conclude that for the measurements of hadronic cross sections at B-factories the mass scale is defined with a relative accuracy better than or about 5×10^{-4}.

C. ISR luminosity

It is clear that a radiation of a hard photon significantly decreases the cross section, so the ISR technique can be efficient at high-luminosity colliders only. To compare the effectiveness of the ISR method for the measurement of hadronic cross sections with direct e^+e^- experiments, it is useful to introduce the concept of ISR luminosity. The mass spectrum for the ISR process $e^+e^- \to X\gamma$ is expressed in terms of the ISR differential luminosity dL/dm and the Born cross section for the process $e^+e^- \to X$ as

$$\frac{dN}{dm} = \varepsilon(m)(1+\delta(m))\sigma_0(m)\frac{dL}{dm}, \qquad (9)$$

where $1+\delta(m) = W(m)/W_0(m)$ is the radiative correction factor discussed in Sec. I.C. The ISR luminosity is proportional to the total integrated luminosity L collected in an experiment and the lowest-order radiator function given by Eq.(7) or Eq.(8) depending on the angular range used for determination of the detection efficiency $\varepsilon(m)$:

$$\frac{{\rm d}L}{{\rm d}m} = W_0(m)\frac{2m}{s}L. \qquad (10)$$

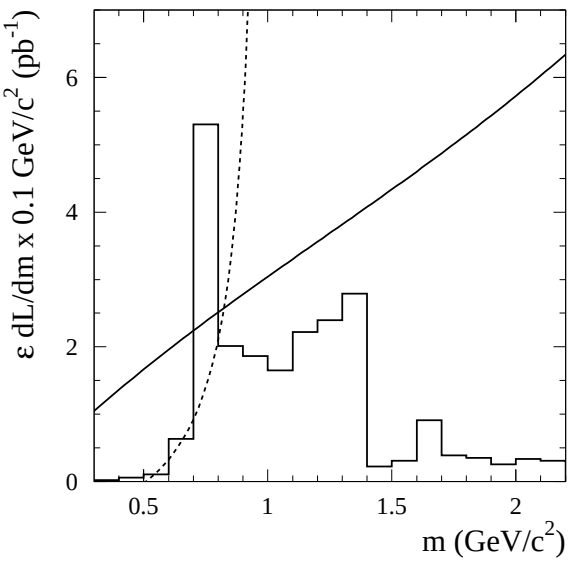


FIG. 10 The mass dependence of the ISR differential luminosity multiplied by the detection efficiency. The solid curve shows the $\varepsilon {\rm d}L/{\rm d}m$ for the B-factory ($2E_0 = 10.58$ GeV, $L = 500$ fb^{-1}, tagged ISR photon), while the dashed curve shows the same function for the ϕ-factory ($2E_0 = 1.02$ GeV, $L = 240$ pb^{-1}, untagged ISR photon). The histogram represents integrated luminosities collected in direct e^+e^- experiments with the SND detector (Achasov *et al.*, 2002) at the Novosibirsk VEPP-2M collider (below 1.4 GeV/c^2), and with the DM1 (Bisello *et al.*, 1981) and DM2 (Antonelli *et al.*, 1992) detectors at the Orsay DCI collider (above 1.4 GeV/c^2).

The mass dependence of the ISR differential luminosity multiplied by the detection efficiency for the BABAR experiment is shown in Fig. 10 for masses below 2.2 GeV/c^2. The detection efficiency used was calculated in Sec. II.A for the process $e^+e^- \to \pi^+\pi^-\gamma$ with a tagged ISR photon. The integrated luminosity is taken to be 500 fb^{-1}. The dashed curve in Fig. 10 shows the same quantity calculated for the KLOE experiment with the integrated luminosity of 240 pb^{-1} and detection efficiency taken for the case of an untagged ISR photon (Fig. 8). The luminosity of 240 pb^{-1} was used in the recent measurement (Ambrosino *et al.*, 2009) of the $e^+e^- \to \pi^+\pi^-$ cross section in the 0.592–0.975 GeV/c^2 mass range. The total integrated luminosity collected by the KLOE is about an order of magnitude larger, 2.5 fb^{-1}. The KLOE ISR luminosity is shown only up to 0.92 GeV/c^2. It increases sharply and reaches 21 pb^{-1} at 0.975 GeV/c^2. It should be noted that the BABAR measurement of the $e^+e^- \to \pi^+\pi^-$ cross section (Aubert *et al.*, 2009a) is also based on a part of the recorded data corresponding to 232

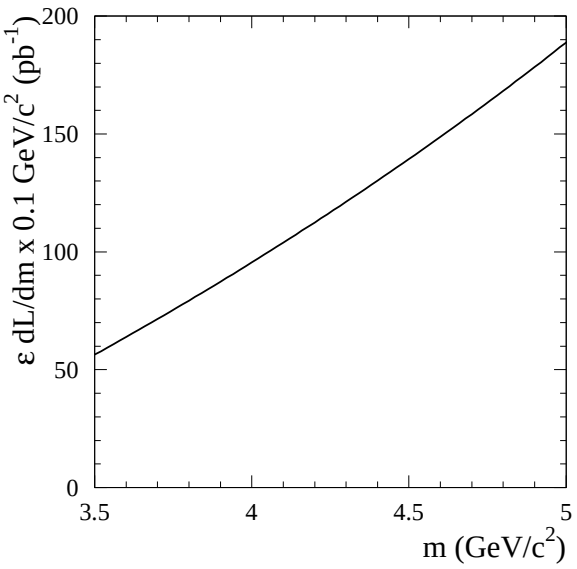


FIG. 11 The mass dependence of the ISR differential luminosity multiplied by the detection efficiency for experiments at the B-factory ($2E_0 = 10.58$ GeV, $L = 500$ fb^{-1}, untagged ISR photon) in the charm production mass region.

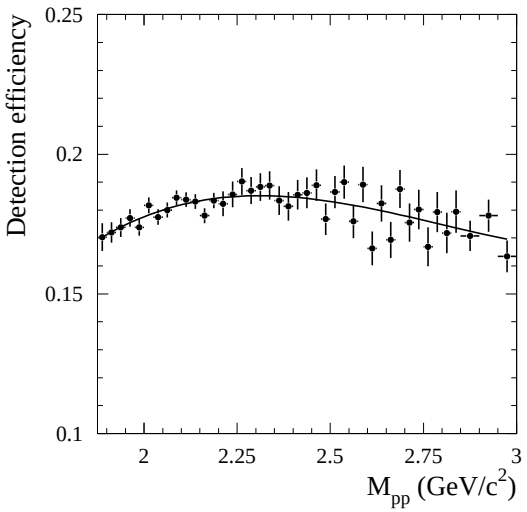


FIG. 12 The detection efficiency for the process $e^+e^- \to p\bar{p}\gamma$ (Aubert *et al.*, 2006a) as a function of the $p\bar{p}$ invariant mass. The curve represents the result of a polynomial fit.

fb^{-1}. The histogram in Fig. 10 shows the distribution of the integrated luminosities collected in some direct e^+e^- experiments. At masses below 1.4 GeV/c^2 the statistics of the SND experiment (Achasov *et al.*, 2002) recorded at the VEPP-2M collider is presented. This is the largest integrated luminosity collected in this mass region in a single experiment. The mass bin 1.0–1.1 GeV/c^2 does not include about 13 pb^{-1} taken by SND in vicinity of the ϕ-meson resonance. The significant part of the statistics from the 0.7–0.8 GeV/c^2 mass interval is collected in the ω-meson mass window 0.76–0.80 GeV/c^2. In the c.m. energy range 1.4–2.2 GeV/c^2 the experiments with the largest statistics are DM1 and DM2 at the Orsay DCI e^+e^- collider. The histogram at $m > 1.4$ GeV/c^2 shows a sum of the integrated luminosities collected with these detectors.

At low masses of the hadronic system the data samples of ISR events currently available at B-factories exceed the statistics collected in conventional e^+e^- experiments, especially at masses below 0.7 GeV/c^2 and above 1.4 GeV/c^2. The ISR luminosity of the ϕ-factory increases very rapidly with mass. For masses below 0.8 GeV/c^2 the luminosity currently used for ISR analysis (Ambrosino *et al.*, 2009) is comparable with that collected in direct e^+e^- experiments. For higher masses it exceeds both BABAR and e^+e^- luminosities.

The ISR luminosity for the mass region of charm production is presented in Fig. 11. It corresponds to the 500 fb^{-1} integrated luminosity collected at $2E_0 =$ 10.58 GeV/c^2 and is multiplied by the detection efficiency calculated for the case of an untagged ISR photon (Fig. 6). The ISR luminosity in this mass region significantly exceeds the integrated luminosity collected in direct e^+e^- experiments including the recent CLEO-c energy scan (Cronin-Hennessy *et al.*, 2009), 60 pb^{-1} at twelve points between 3.97 and 4.26 GeV.

Thus, the current data samples of ISR events produced at the B- and ϕ-factories are larger than those produced directly in e^+e^- collisions for all masses of interest excluding the regions near the narrow resonances (ω, ϕ, J/ψ, $\psi(2S)$). For masses above 1.4 GeV/c^2 this allows to significantly improve accuracy of the measurements of exclusive hadronic cross sections. In the mass region below 1.4 GeV/c^2 the results obtained with the ISR method are comparable to rather precise direct e^+e^- measurements.

D. Comparison with e^+e^- scan

The ISR technique offers some advantages over conventional e^+e^- measurements. One of them is that the entire hadronic mass range is accessible in one experiment. This allows one to avoid relative normalization uncertainties which inevitably arise when data from different experiments, or from different machine settings in one experiment, are combined.

The ISR measurements with a tagged photon have additional advantages. In many cases, particularly for final states with low invariant mass of the produced particles, the hadronic system is collimated along the direction opposite to the ISR photon. Therefore, the detection efficiency has low sensitivity to hadron angular distributions in the hadronic-system rest frame. In Fig.7 the angular dependence of the detection efficiency is shown for the process $e^+e^- \to p\bar{p}\gamma$ (Aubert *et al.*, 2006a). The angular dependence is close to uniform. This reduces the model dependence of the cross section measurement due

to the unknown relation between the values of the proton electric and magnetic form factors, and significantly facilitates data analysis. Note that in conventional experiments at e^+e^- or $p\bar{p}$ colliders the detector acceptance for the final $p\bar{p}$ or e^+e^- systems falls to zero when $\cos\theta_p$ approaches ± 1.

For ISR events the final hadrons have non-zero momenta at the production threshold and are therefore detected with full efficiency. In Fig.12 the detection efficiency for the process $e^+e^- \to p\bar{p}\gamma$ process (Aubert *et al.*, 2006a) is shown as a function of the $p\bar{p}$ invariant mass. No strong variation of the efficiency with mass is observed, while in direct e^+e^- measurements the detection efficiency vanishes at the threshold because of the low momenta of the produced particles. This feature of ISR hadron production was successfully used at BABAR for the measurements of the $e^+e^- \to p\bar{p}$ (Aubert *et al.*, 2006a) and $e^+e^- \to \pi^+\pi^-$ (Aubert *et al.*, 2009a) cross sections in near-threshold mass regions.

For the measurement of the $e^+e^- \to \pi^+\pi^-$ cross section, particle identification plays a crucial role. In the ISR process $e^+e^- \to \pi^+\pi^-\gamma$ at B-factories most of the final pions have momenta larger than 1 GeV/c. For such pion momenta a good $\pi/\mu/e$ separation is provided which allows one to almost completely remove the $e^+e^- \to e^+e^-\gamma$ and $e^+e^- \to \mu^+\mu^-\gamma$ backgrounds (Aubert *et al.*, 2009a). This is in contrast with direct e^+e^- measurements (Achasov *et al.*, 2006; Akhmetshin *et al.*, 2004a, 2007) in which it is difficult to separate $e^+e^- \to \pi^+\pi^-$ and $e^+e^- \to \mu^+\mu^-$ events in the most interesting ρ-meson mass region (0.60–0.95 GeV). As a result, a sum of the cross sections is measured. The contribution of the process $e^+e^- \to \mu^+\mu^-$ is then subtracted using its theoretically calculated cross section. This leads to an increase of statistical and systematic errors of the measurement.

It should be noted that the advantages of tagged ISR discussed above (weak mass and angular dependences of the detection efficiency) are completely absent for untagged ISR. In this case the mass and angular dependences are even stronger than those for events of direct e^+e^- annihilation.

A disadvantage of ISR is that the mass resolution and absolute mass scale calibration are much poorer than the beam energy spread and the accuracy of the beam energy setting in direct e^+e^- annihilation experiments. The influence of the resolution effects on the ISR measurement is discussed in Sec. II.B.

The main disadvantage of the ISR measurements is presence of a wide spectrum of background processes different from those in direct e^+e^- experiments. For example, in e^+e^- annihilation the main background process for $e^+e^- \to \pi^+\pi^-\pi^0$ is $e^+e^- \to \pi^+\pi^-\pi^0\pi^0$ with a lost π^0. For the ISR process $e^+e^- \to \pi^+\pi^-\pi^0\gamma$ with the 3π mass in the range $m_{3\pi} \pm \Delta m/2$, this background corresponds to the contribution of the process $e^+e^- \to \pi^+\pi^-\pi^0\pi^0\gamma$ with the 4π mass in the same range $m_{3\pi} \pm \Delta m/2$. The presence in ISR of $4\pi\gamma$ events with arbitrary masses, which may, in particular, be out of the $m_{3\pi} \pm \Delta m/2$ range, greatly increases background.

At the ϕ-factory and in future ISR measurements at the tau-charm factory in Beijing the background from FSR processes should be taken into account when the ISR photon is detected. The FSR contribution for the $e^+e^- \to \pi^+\pi^-$ measurements at KLOE is calculated with the PHOKHARA generator, which models FSR for pions using scalar QED, and also takes into account the radiative ϕ decays to $\pi^+\pi^\gamma$ via the $f_0(980)\gamma$ and $\rho\pi$ intermediate states. The pion electromagnetic form factor used in the generator is obtained from a fit to the $e^+e^- \to \pi^+\pi^-$ experimental data. In the case of the tau-charm factory, experimental information on exclusive hadronic cross sections in the energy range from 3.0 to 4.5 GeV obtained at B-factories can be used to estimate the FSR contribution. Additional theoretical input is required to estimate structure-dependent FSR.

Another background source is the non-ISR process of e^+e^- annihilation into hadrons containing a high-energy π^0. In particular, the events of the process $e^+e^- \to X\pi^0$ with an undetected soft photon or merged photons from the π^0 decay may almost completely imitate the $e^+e^- \to X\gamma$ events. This background is usually subtracted statistically using for normalization selected $e^+e^- \to X\pi^0$ events with a reconstructed π^0. In tagged ISR measurements at B-factories the process $e^+e^- \to X\pi^0$ becomes the dominant background source at relatively high masses, about 2 GeV/c^2. It limits the mass region for ISR studies of light hadrons to masses below 4.0–4.5 GeV/c^2.

In ISR measurements with an untagged ISR photon, the background from $e^+e^- \to X\pi^0$ can be significantly suppressed by requiring that the missing momentum in an event be directed along the beam axis. For untagged ISR, the main sources of background are ISR processes and two-photon processes $e^+e^- \to e^+e^-\gamma^*\gamma^* \to e^+e^-X$ in which initial electron and positron are scattered predominantly at small angles. The latter background can be suppressed by a condition on the missing mass, which should be close to zero for ISR events and has a wide distribution for two-photon events.

Background suppression and subtraction are the main sources of the systematic uncertainty on ISR measurements.

E. Colliders and detectors using ISR

ISR processes were studied in many e^+e^- experiments either as a source of useful physical information or as a source of background. For example, possibly the first study of the process $e^+e^- \to \pi^+\pi^-\gamma$ was performed more than 20 years ago with the ND detector at the VEPP-2M collider (Dolinsky *et al.*, 1991; Vasserman *et al.*, 1988). In this work, the FSR process $e^+e^- \to \rho \to \pi^+\pi^-\gamma$ was measured with the ISR process $e^+e^- \to \rho\gamma \to \pi^+\pi^-\gamma$ studied as a main source of background. Many inter-

esting ISR studies have been performed with the CLEO detector, see, e.g., Ref. (Adams *et al.*, 2006). Below we give a brief description of only three detectors: BABAR, Belle, and KLOE, which made a great contribution both to development of the ISR technique and ISR measurements of hadronic cross sections.

F. PEP-II and BABAR

The PEP-II B-factory at SLAC is a two-ring asymmetric-energy e^+e^- collider with energies of 9 GeV for the electron and 3.1 GeV for the positron beam, operating at the c.m. energy of 10.58 GeV, at the maximum of the $\Upsilon(4S)$ resonance (Seeman *et al.*, 2001). The maximum luminosity achieved at PEP-II was slightly over 10^{34} cm^{-2} s^{-1}. The principal goal of the PEP-II B-factory and the BABAR detector is studies of CP violation in the B-meson system.

The BABAR detector (Fig.13) is described in detail elsewhere (Aubert *et al.*, 2002). Final states with charged particles are reconstructed in the BABAR tracking system, which comprises a five-layer silicon vertex tracker (SVT) and a 40-layer drift chamber (DCH) operating in a 1.5-T axial magnetic field. The vertex position is measured by the SVT with the accuracy of 50 μm. The momentum resolution for 1 GeV/c charged tracks is $\sigma_{p_t}/p_t = 0.5\%$. Charged-particle identification is provided by an internally reflecting ring-imaging Cherenkov detector (DIRC), and by energy loss measurements in the SVT and DCH. The hard ISR photon and photons from π^0 decays are detected in a CsI(Tl) electromagnetic calorimeter (EMC). The energy resolution for 1 GeV photons is about 3%; the angles of photons are measured with the 4 mrad accuracy. Muons are identified in the instrumented flux return (IFR) of the solenoid, which consists of iron plates interleaved with resistive plate chambers.

Experiments at the PEP-II collider with the BABAR detector were carried out from 1999 to 2008. The total integrated luminosity is close to 530 fb^{-1}. The ISR studies at BABAR started in 2001. The ISR research program includes a study of the light hadron production with a tagged ISR photon and charm and charmonium studies with an untagged photon.

G. KEKB and BELLE

The KEK B-Factory, KEK-B, is an asymmetric-energy (similar to PEP-II) e^+e^- collider with the 8-GeV electron and 3.5-GeV positron beams and the maximum luminosity of $2.1 \cdot 10^{34}$ cm^{-2} s^{-1} (Kurokawa *et al.*, 2003). The main physical goal of this project is to perform a detailed study of B-meson properties, in particular, CP-violation.

The Belle detector (Abashian *et al.*, 2002) (Fig.14) is configured inside a 1.5 T superconducting solenoid. The B-meson vertices are measured in a three-layer doublesided silicon vertex detector with about 50 μm impact parameter resolution for 1 GeV/c momentum track at $\theta \simeq \pi/2$. Track momenta are measured in a 50-layer wire drift chamber with a 0.4% momentum resolution at 1 GeV/c. Particle identification is provided by dE/dx measurements in the drift chamber, aerogel Cherenkov counters, and time-of-flight counters placed outside the drift chamber. Electromagnetic showers are detected in a CsI(Tl) calorimeter located inside the solenoid coil. The energy resolution is 2% for 1-GeV photons. An iron flux-return located outside the coil is instrumented to detect K_L-mesons and identify muons.

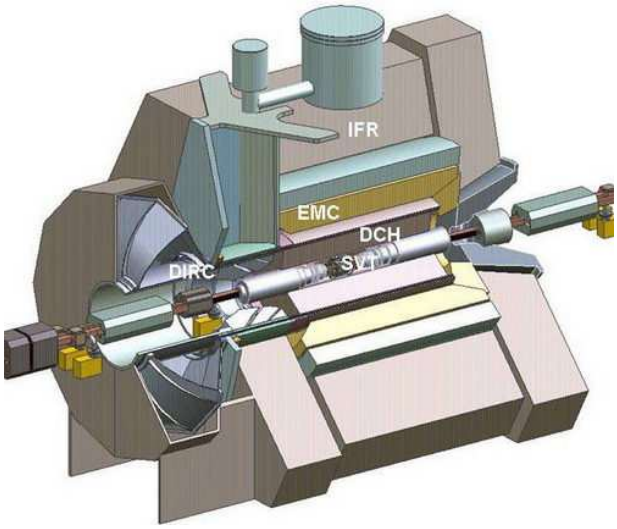


FIG. 13 View of the BABAR detector.

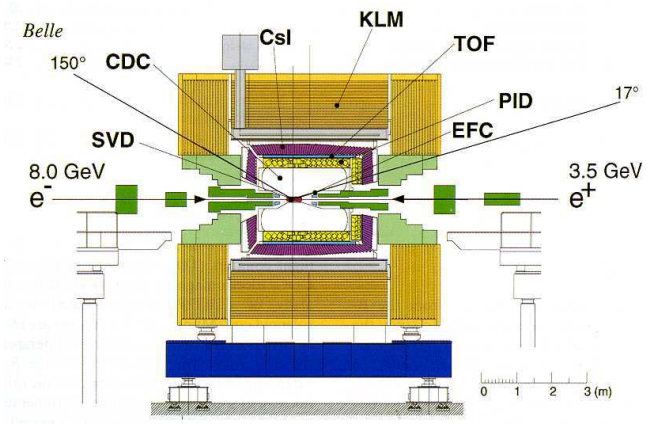


FIG. 14 Side view of the Belle detector.

Experiments with Belle started in 2000 and stopped in 2010. The Belle integrated luminosity reaches 1000 fb^{-1}. The ISR experiments are mainly devoted to the production of charm and charmonium hadronic states with mass above 4 GeV/c^2. ISR analysis of light mesons is in progress.

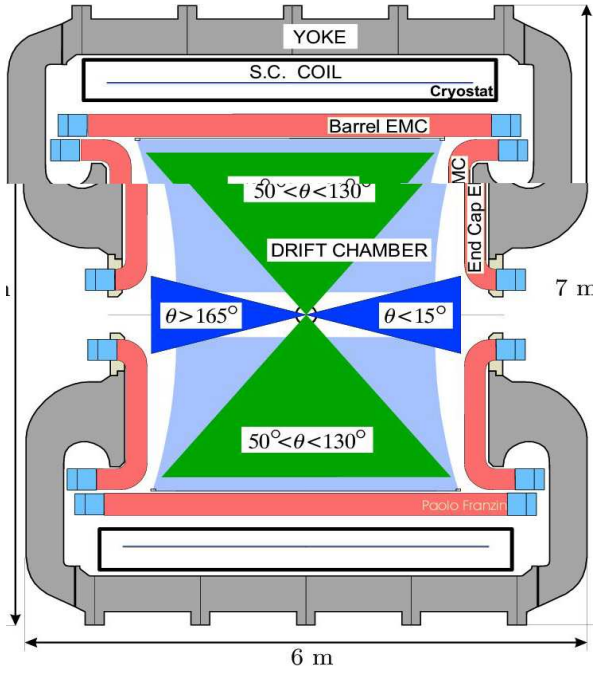


FIG. 15 KLOE detector (Muller, 2009). The polar-angle regions used to select tagged ($50^\circ < \theta_\gamma < 130^\circ$) and untagged ($\theta_\gamma < 15^\circ$ or $\theta_\gamma > 165^\circ$) ISR events are shown.

H. DAΦNE and KLOE

DAΦNE, the Frascati ϕ-factory (Franzini and Moulson, 2006), is in operation since 1999. The main goal of the DAΦNE project is a study of neutral and charged kaons, intensively produced at the energy corresponding to the maximum of $\phi(1020)$ resonance. Similar to PEP-II and KEK-B, DAΦNE uses two separate rings for storing electron and positrons, but beams have equal energies. The DAΦNE design luminosity is $5 \cdot 10^{32}$ cm^{-2} s^{-1}.

KLOE (Franzini and Moulson, 2006) (Fig.15) is the main DAΦNE detector. The detector consists of a large-volume drift chamber (DC) surrounded by a hermetic electromagnetic calorimeter (EMC). A superconducting coil provides an axial magnetic field of 0.52 T. In order to reduce neutral kaon regeneration and charged-particle multiple scattering, the gas mixture of 90% helium and 10% isobutane is used in the DC. Charged-track momenta are measured with the $\sigma_p/p = 0.4\%$ accuracy. The lead-scintillation fiber calorimeter provides the energy resolution for electromagnetic showers of $\sigma_E/E = 5.7\%/\sqrt{E(\mathrm{GeV})}$, and the time resolution of $\sigma_t = 54\mathrm{ps}/\sqrt{E(\mathrm{GeV})} \bigoplus 140\mathrm{ps}$.

The total integrated luminosity accumulated with KLOE is about 3 fb^{-1}. The only, but very important, ISR process studied at KLOE is $e^+e^- \to \pi^+\pi^-\gamma$.

III. PRODUCTION OF LIGHT QUARK MESONS

A. Overview

As already mentioned in the Introduction, e^+e^- annihilation into hadrons at c.m. energies below 2 GeV plays a very important role in many fundamental problems of particle physics. In particular, knowledge of its total cross section is mandatory for the calculation of the muon anomalous magnetic moment in Standard Model. For many years only e^+e^- scan experiments provided information on this reaction and determined the uncertainty of the SM prediction of the muon anomaly (Davier *et al.*, 2003a,b). Main information on light vector mesons has been also obtained in such measurements. Unfortunately, the collected data samples were not sufficient for a precise determination of parameters of excited vector mesons. Recently, due to a very high luminosity of the e^+e^- factories, DAFNE, KEK-B, and PEP-II, the ISR technique became a powerful tool for an independent study of e^+e^- annihilation at low energies.

The KLOE collaboration used the ISR method at the ϕ meson energy to study the reaction $e^+e^- \to \pi^+\pi^-$ and measure the pion electromagnetic form factor (Aloisio *et al.*, 2005; Ambrosino *et al.*, 2009, 2011; Muller, 2009). Recently, results on this process were also reported by the BABAR collaboration (Aubert *et al.*, 2009a).

A variety of high-multiplicity final states were studied at BABAR: $\pi^+\pi^-\pi^0$ (Aubert *et al.*, 2004b), $2(\pi^+\pi^-)$, $\pi^+\pi^-K^+K^-$ and $2(K^+K^-)$ (Aubert *et al.*, 2005b), $3(\pi^+\pi^-)$, $2(\pi^+\pi^-\pi^0)$ and $K^+K^-2(\pi^+\pi^-)$ (Aubert *et al.*, 2006b), $2(\pi^+\pi^-)\pi^0$, $2(\pi^+\pi^-)\eta$, $K^+K^-\pi^+\pi^-\pi^0$ and $K^+K^-\pi^+\pi^-\eta$ (Aubert *et al.*, 2007c), $K^+K^-\pi^+\pi^-$ and $K^+K^-\pi^0\pi^0$ (Aubert *et al.*, 2007b), $K^+K^-\pi^+\pi^-$, $K^+K^-\pi^0\pi^0$ and $K^+K^-K^+K^-$ (Aubert *et al.*, 2007b), $K^\pm K^0_S\pi^\mp$, $K^+K^-\pi^0$ and $K^+K^-\eta$ (Aubert *et al.*, 2008b). The final $K^+K^-\pi^+\pi^-$ state was also investigated by Belle (Shen *et al.*, 2009).

Studies of the exclusive channels of e^+e^- annihilation listed above allow to determine such fundamental parameters as mass, width and leptonic width of various vector mesons. In addition to the low-lying resonances, such as the ρ, ω and ϕ, where ISR studies can independently provide meaningful and competitive information, they are indispensable for a much more precise than before investigation of the excited vector states.

Moreover, detailed analysis of the dynamics shows that in many cases a multiparticle final state can be reached via different intermediate mechanisms. For example, four pions can be produced via $\omega\pi^0$, $a_1(1260)\pi$, $\rho^0 f_0$, ... In the following sections we show a complexity of the internal substructures observed in some channels, which are often used to extract parameters of the resonances involved in the substructures.

In general, amplitudes corresponding to different intermediate mechanisms interfere affecting the energy and angular distributions of the final particles. This interference should be taken into account to avoid additional systematic errors.

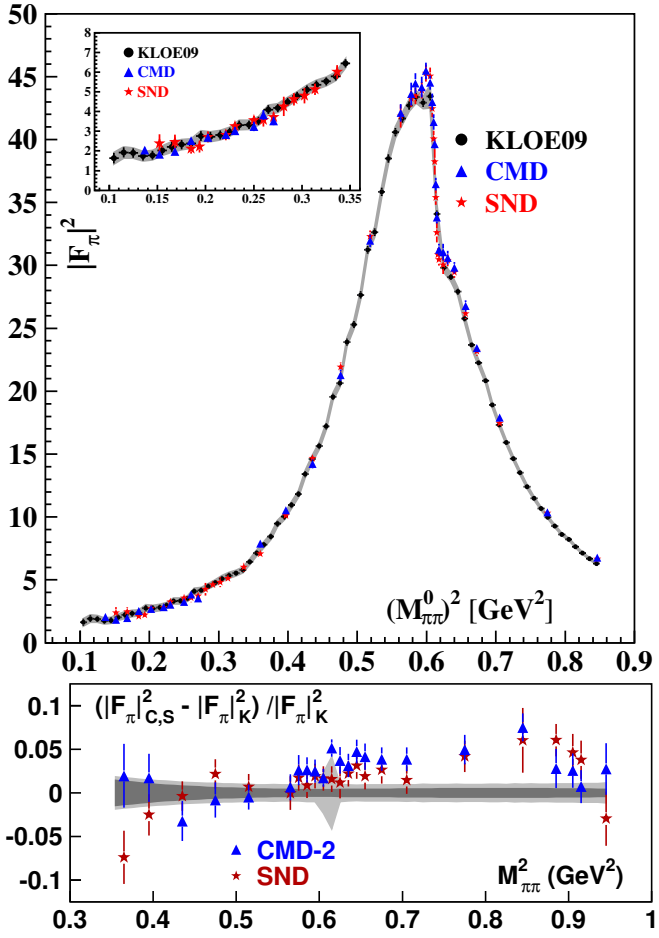


FIG. 16 Top: The pion form factor obtained by KLOE in the reaction $e^+e^- \to \pi^+\pi^-\gamma$ with a tagged ISR photon (Muller, 2009). Bottom: Relative difference between the KLOE result with an untagged ISR photon (Ambrosino *et al.*, 2009) and the direct e^+e^- measurements by SND (Achasov *et al.*, 2006) and CMD-2 (Akhmetshin *et al.*, 2007). The dark (light) band indicates the KLOE uncertainty (statistical and systematic errors combined in quadrature). For the SND and CMD-2 data, the combined statistical and systematic errors are shown.

Unless otherwise stated, all cross sections in the following sections are corrected for effects of initial-state radiation only. Neither final-state radiation nor vacuum polarization corrections have been applied.

B. $e^+e^- \to \pi^+\pi^-$

The reaction $e^+e^- \to \pi^+\pi^-$ was relatively well studied for c.m. energies up to 1.4 GeV in direct e^+e^- experiments. The most precise measurements were performed with the CMD-2 (Akhmetshin *et al.*, 2004a, 2007) and SND (Achasov *et al.*, 2006) detectors at the VEPP-2M

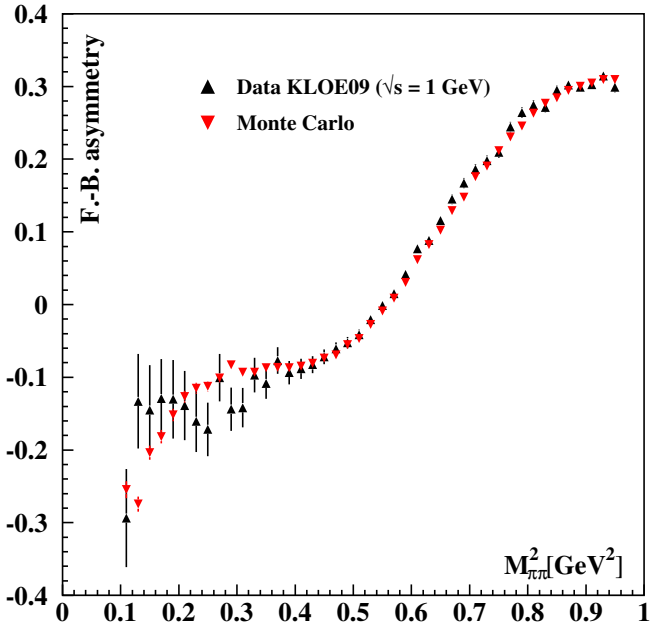


FIG. 17 Forward-backward asymmetry in the reaction $e^+e^- \to \pi^+\pi^-(\gamma)$ measured with the KLOE detector (Muller, 2009).

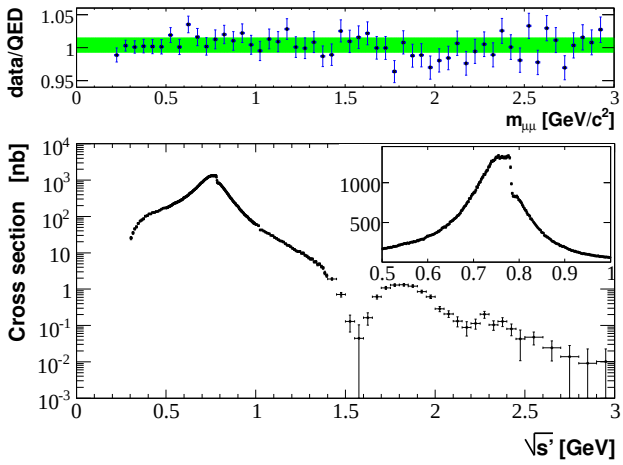


FIG. 18 Top: The QED test by the ratio of the $e^+e^- \to \mu^+\mu^-$ cross section in data to the theoretical one. Bottom: The $e^+e^- \to \pi^+\pi^-$ cross sections measured with the BABAR detector (Aubert *et al.*, 2009a).

collider. The CMD-2 measurements have a systematic uncertainty in the 1% range.

The dominant contribution to this process comes from the $\rho(770)$ meson production. A measurement of the $e^+e^- \to \pi^+\pi^-$ cross section in the $\rho(770)$ mass region was performed by KLOE using the ISR method (Aloisio *et al.*, 2005; Ambrosino *et al.*, 2009, 2011; Muller, 2009). For the first time it was demonstrated that the cross section determined by this method could have smaller statistical errors than direct e^+e^- measurements and could be competitive with them in a systematic uncertainty. Both untagged (Aloisio *et al.*, 2005; Ambrosino *et al.*, 2009) and tagged (Ambrosino *et al.*, 2011; Muller, 2009) ISR $\pi^+\pi^-\gamma$ events were studied with consistent results. While the tagged measurement has worse statistical errors and an additional source of the systematic uncertainty due to the FSR contribution, it covers the region of small invariant masses inaccessible for the untagged measurement. The result of the tagged measurement (Ambrosino *et al.*, 2011; Muller, 2009) represented as a pion electromagnetic form factor squared is shown in Fig. 16(top) together with the results of the direct e^+e^-measurements with the CMD-2 (Akhmetshin *et al.*, 2007) and SND (Achasov *et al.*, 2006) detectors. Comparison of the more precise untagged KLOE measurement (Ambrosino *et al.*, 2009) with the CMD-2 and SND data is given in Fig. 16(bottom). At invariant masses corresponding to the maximum of the ρ resonance and its high-mass tail the points from direct e^+e^-measurements lie systematically higher than those from KLOE. In this mass region the difference between the CMD-2 and KLOE measurements is definitely larger than their combined systematic uncertainty. The KLOE systematic error includes the experimental (0.6%) and theoretical (0.6%) uncertainties. Two main sources of the former are tracking and luminosity measurement. The latter is determined mostly by the accuracy of the radiator function calculated with the PHOKHARA event generator. Note that the KLOE Collaboration performed a dedicated study to validate a calculation of FSR effects using forward-backward asymmetry arising from the interference between the ISR and FSR amplitudes (Müller, 2009). The study showed that the assumption of point-like pions works reasonably well and can be used for the FSR calculation, see Fig. 17.

A structure seen at the top of the ρ-meson resonance is due to its interference with the much more narrow $\omega(782)$ resonance also decaying to $\pi^+\pi^-$. Because $\omega(782)$ mass is known precisely, the position of this structure can be used to test the accuracy of the mass scale calibration. Unfortunately, neither KLOE nor BABAR (see below) report the result of such a test.

The PEP-II B-factory also provided a large sample of the $e^+e^- \to \pi^+\pi^-\gamma$ events (about 530 thousand) and the $e^+e^- \to \pi^+\pi^-$ cross section (Aubert *et al.*, 2009a) was measured for the e^+e^- c.m. energies up to 3.0 GeV. In this experiment the $e^+e^- \to \pi^+\pi^-$ cross section is obtained from the ratio of the $\pi^+\pi^-$ and $\mu^+\mu^-$ mass spectra. Due to the normalization to the cross section of the theoretically well known process $e^+e^- \to \mu^+\mu^-\gamma$, the measurement becomes much less sensitive to the experimental uncertainties and to the theoretical uncertainty of the radiator function. A comparison of the measured $\mu^+\mu^-$ mass spectrum for the reaction $e^+e^- \to \mu^+\mu^-\gamma$ with the QED prediction is shown in Fig. 18(top). The data and the prediction are consistent within the estimated systematic uncertainty of 1.1%, dominated by the accuracy of the integrated luminosity measurement. Us-

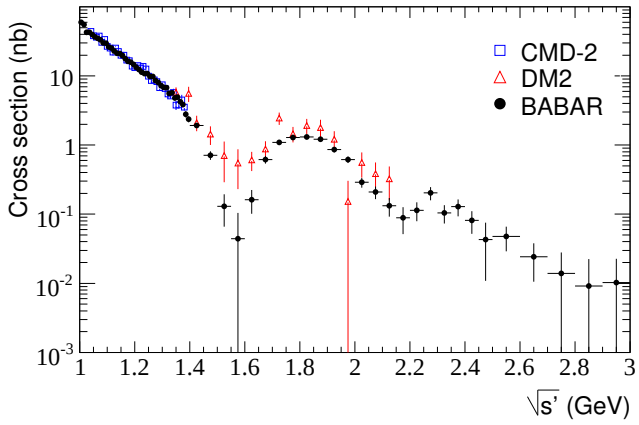


FIG. 19 The $e^+e^- \to \pi^+\pi^-$ cross section above 1 GeV measured with the BABAR detector (Wang , 2009). Comparison with the CMD-2 (Aulchenko *et al.*, 2005) and DM2 (Bisello *et al.*, 1989) measurements is shown.

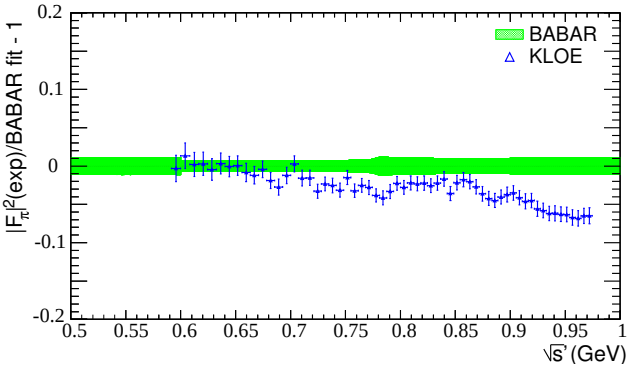


FIG. 20 The relative difference between the KLOE (Ambrosino *et al.*, 2009) and BABAR (Wang , 2009) measurements. The band corresponds to the BABAR statistical and systematic uncertainties combined in quadrature.

ing the bin-by-bin ratio to the cross section of the process $e^+e^- \to \mu^+\mu^-\gamma$ one minimizes theoretical uncertainties and reduces a systematic error at the ρ peak to 0.5% dominated by pion identification and ISR luminosity. Previously such a test was performed in e^+e^- scan experiments at the OLYA detector in the c.m. energy range from 640 MeV to 1400 MeV (Kurdadze *et al.*, 1984) and at the CMD-2 detector from 370 MeV to 520 MeV (Aulchenko *et al.*, 2006) with the achieved precision of comparison of 3% and 1%, respectively.

The measured cross section is shown in Fig. 18(bottom). For the first time a relatively high-statistics measurement is performed for c.m. energies above 1 GeV. The cross section in this energy range shown in Fig. 19 demonstrates some statistically significant structures which can be possibly explained by the interference between the wide ρ-like excited states. Note that the cross section shown in Fig. 18 is bare and includes FSR effects.

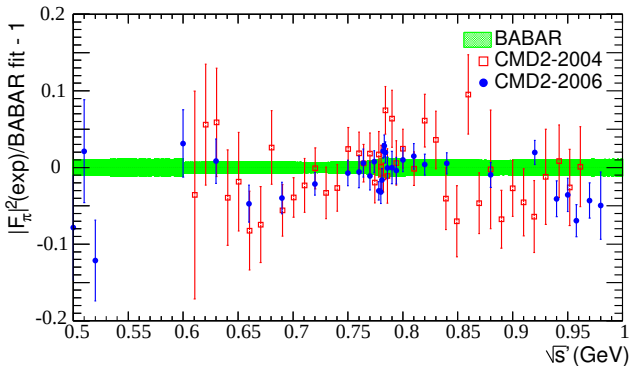


FIG. 21 The relative difference between the CMD-2 (Akhmetshin *et al.*, 2004a, 2007) and BABAR (Wang , 2009) measurements. The band corresponds to the BABAR statistical and systematic uncertainties combined in quadrature.

The claimed sub-percent level of systematic uncertainties on the $e^+e^- \to \pi^+\pi^-$ measurements can be verified by comparison of the results from these very different experiments. Above we found that the difference between the KLOE and CMD-2 measurements is larger than their combined systematic uncertainty. Figure 20 shows a relative difference between the KLOE and BABAR measurements. Again the deviations larger than declared systematic errors are seen indicating a presence of unaccounted systematic uncertainties in one or both experiments. Comparison between the CMD-2 and BABAR shown in Fig. 21 also reveals some non-statistical up to 5% deviations both below and above the ρ-resonance maximum. In the whole energy range BABAR data are in fair agreement with the SND (Achasov *et al.*, 2006) results within experimental uncertainties.

In Section VII we discuss the impact of these measurements on the problem of the muon anomaly.

C. $e^+e^- \to \pi^+\pi^-\pi^0$

A study of the three-pion production in the ISR process was reported by BABAR in Ref. (Aubert *et al.*, 2004b). The three-pion mass distribution for the $e^+e^- \to \pi^+\pi^-\pi^0\gamma$ reaction shown in Fig. 22 is dominated by the well known $\omega(782)$, $\phi(1020)$, and J/ψ resonances. For the $\omega(782)$ and $\phi(1020)$ resonances they determine the product of the leptonic width and the branching fraction to three pions consistent with other measurements and having comparable accuracy. Large data samples make possible the observation of two structures in the 1–2 GeV/c^2 mass region (see Fig. 23). The cross section below 1.4 GeV is in agreement with the SND measurement (Achasov *et al.*, 2002), but at higher energies a large deviation from the DM2 results (Antonelli *et al.*, 1992) is observed. The cross section in this region is fitted (see inset in Fig. 23) assuming the presence of two excited ω-like states, $\omega(1420)$ and $\omega(1650)$ (Amsler *et al.*,

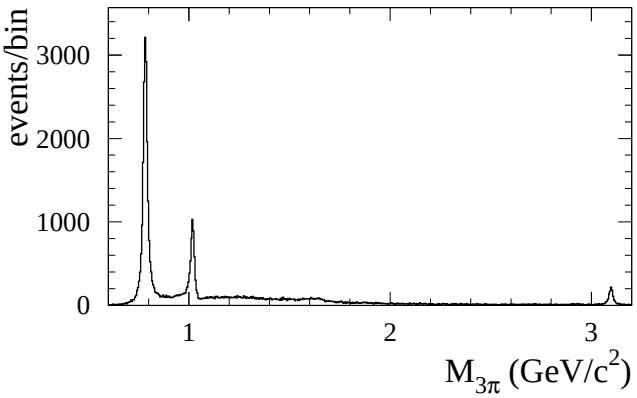


FIG. 22 The $m(\pi^+\pi^-\pi^0)$ distribution for the $e^+e^- \to \pi^+\pi^-\pi^0\gamma$ reaction measured with the BABAR detector (Aubert *et al.*, 2004b).

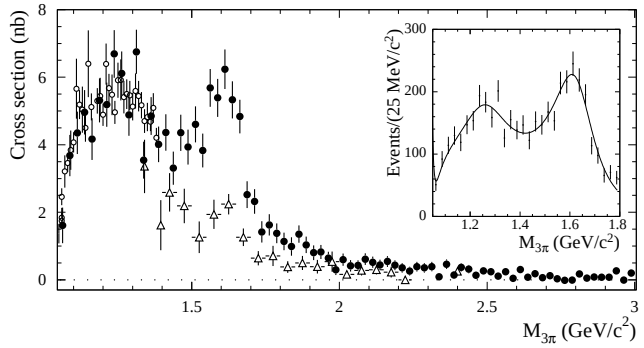


FIG. 23 The $e^+e^- \to \pi^+\pi^-\pi^0$ cross section measured with the BABAR detector (Aubert *et al.*, 2004b) in the 1-3 GeV/c^2 range compared with the SND (Achasov *et al.*, 2002) (open circles) and DM2 (Antonelli *et al.*, 1992) (triangles) data. The inset shows the mass distribution fitted with two resonances.

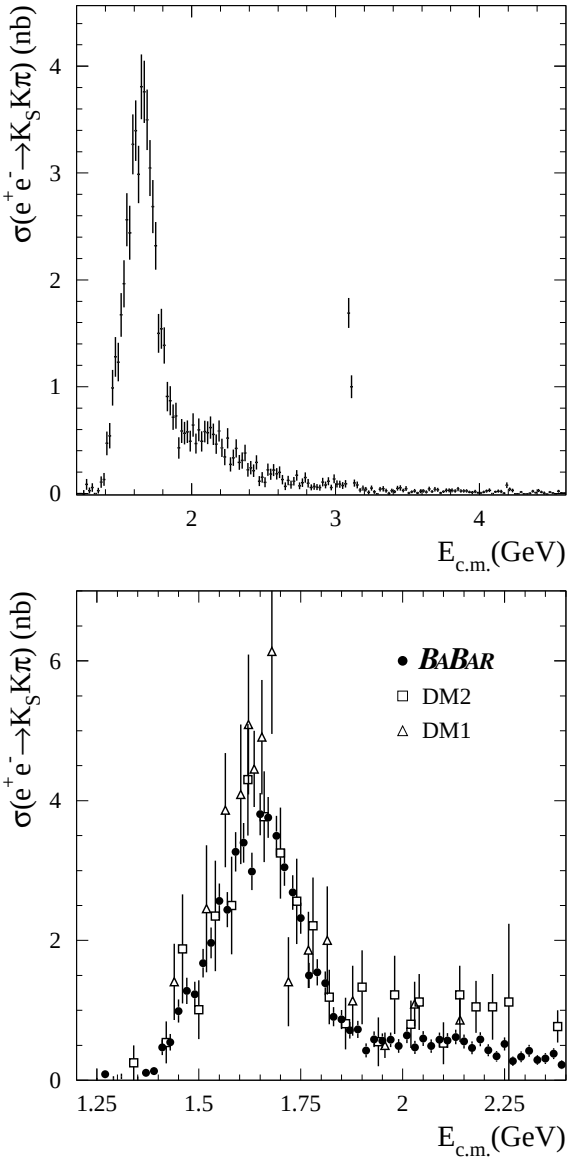


FIG. 24 The $e^+e^- \to K^0_S K^\pm\pi^\mp$ cross section measured by BABAR (Aubert *et al.*, 2008b) (top). Comparison of the BABAR measurement with the results of the previous DM1 (Buon *et al.*, 1982) and DM2 (Bisello *et al.*, 1991b) experiments (bottom).

2008). The parameters of these states are still not well determined. In this case they strongly depend on relative phases between the corresponding amplitudes and their phase differences with the $\omega(782)$ and $\phi(1020)$ amplitudes. The latter resonances have a much larger decay rate to the 3π mode. The obtained parameters of the $\omega(1420)$ and $\omega(1650)$ are summarized in Table II.

The three-body final state is a relatively simple process for a study of hadron dynamics. Its Dalitz plot analysis shows that the $\rho(770)^\pm\pi^\mp$ and $\rho(770)^0\pi^0$ intermediate states dominate at all energies. There is also a small contribution of the $\omega\pi$ intermediate state with ω decay to $\pi^+\pi^-$.

D. $e^+e^- \to K^+K^-\pi^0$, $K^0_S K^\pm\pi^\mp$, $K^+K^-\eta$

Figures 24 and 25 show the $e^+e^- \to K^+K^-\pi^0$ and $e^+e^- \to K^0_S K^\pm\pi^\mp$ cross sections measured in the BABAR experiment (Aubert *et al.*, 2008b) (top) and comparison of the BABAR results with DM1 (Buon *et al.*, 1982) and DM2 (Bisello *et al.*, 1991b) measurements below 2.4 GeV where the previous data are available (bottom). The BABAR data are about 10 times more precise. The "spike" at 3.1 GeV is due to J/ψ decays to these final states and will be discussed later.

In the $K^+K^-2\gamma$ final state the $\phi(1020)\eta$ and $\phi(1020)\pi$ intermediate states were also observed. The measured cross sections for these states, which were not previously studied, are shown in Figs. 26 and 27. The $e^+e^- \to \phi(1020)\eta$ is the best channel for a study of the excited ϕ state. The contributions of the ω-like states to this

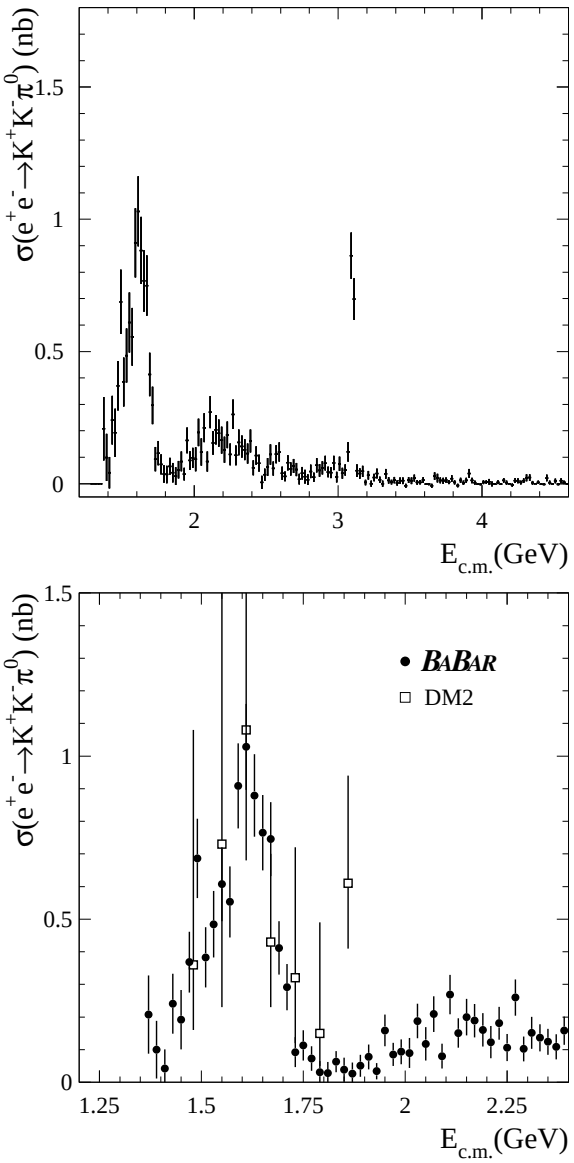


FIG. 25 The $e^+e^- \to K^+K^-\pi^0$ cross section measured by BABAR (Aubert *et al.*, 2008b)(top). Comparison of the BABAR measurement with the result of the DM2 experiment (Bisello *et al.*, 1991b) (bottom).

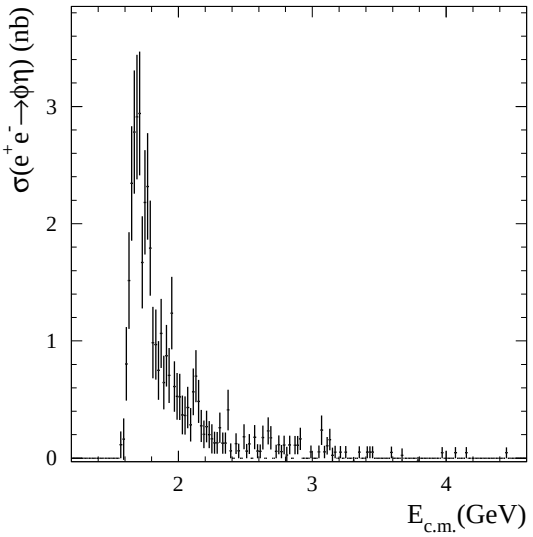


FIG. 26 The $e^+e^- \to \phi\eta$ cross sections measured with the BABAR detector (Aubert *et al.*, 2008b).

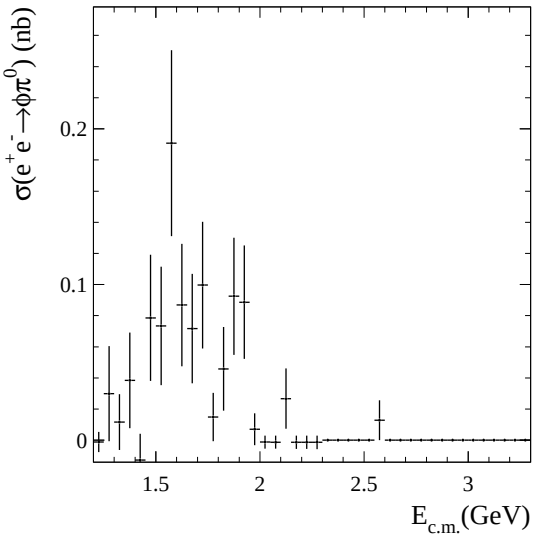


FIG. 27 The $\phi\pi^0$ cross sections measured with the BABAR detector (Aubert *et al.*, 2008b).

channel should be suppressed by the OZI rule.

The reaction $e^+e^- \to \phi(1020)\pi^0$ is promising for a search for exotic isovector resonances. For ordinary isovector states, the $\phi\pi^0$ decay should be suppressed by the OZI rule. The authors perform two fits of the cross section. In the first one they assume a single resonance and obtain for it mass and width of 1593 ± 32 MeV/c^2 and 203 ± 97 MeV, respectively. These parameters are compatible with those of the $\rho(1700)$ (Amsler *et al.*, 2008). A somewhat better quality of the fit is achieved if two resonances are assumed. The obtained parameters of the first resonance are $1570\pm36\pm62$ MeV/c^2 for the mass and $144\pm75\pm43$ MeV for the width, i.e., consistent with those of the $C(1480)$ state observed in Ref. (Bityukov *et al.*, 1987). The mass and width for the second resonance are $1909 \pm 17 \pm 25$ MeV/c^2 and $48 \pm 17 \pm 2$ MeV, respectively, compatible with the dip already observed in other experiments, predominantly in multipion final states (Antonelli *et al.*, 1996; Aubert *et al.*, 2006b; Baldini *et al.*, 1988; Frabetti *et al.*, 2000). With the limited statistics available at the moment they cannot draw a firm conclusion: an OZI-violating decay of the $\rho(1700)$ cannot be excluded.

Figure 28 shows the Dalitz plots for the $K^+K^-\pi^0$ and $K^0_SK^\pm\pi^\mp$ final states. It is seen that the $K\bar{K}^*(892)$ and $K\bar{K}^*_2(1430)$ intermediate states give the main contribution to the $K\bar{K}\pi$ production. For the $K^0_SK^\pm\pi^\mp$ final

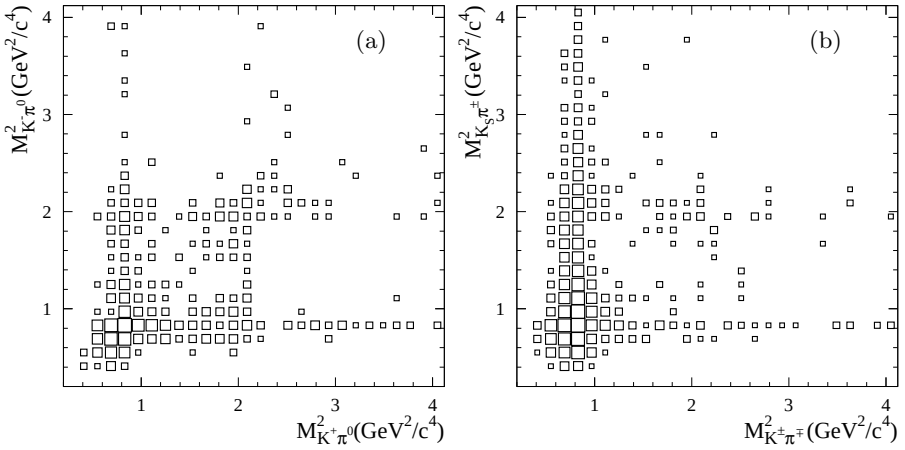


FIG. 28 The Dalitz plot distribution for the $K^+K^-\pi^0$ (a) and $K^0_SK^\pm\pi^\mp$ final state (b) from Ref. (Aubert *et al.*, 2008b). A sum over all accessible c.m. energies of the hadronic final states is given.

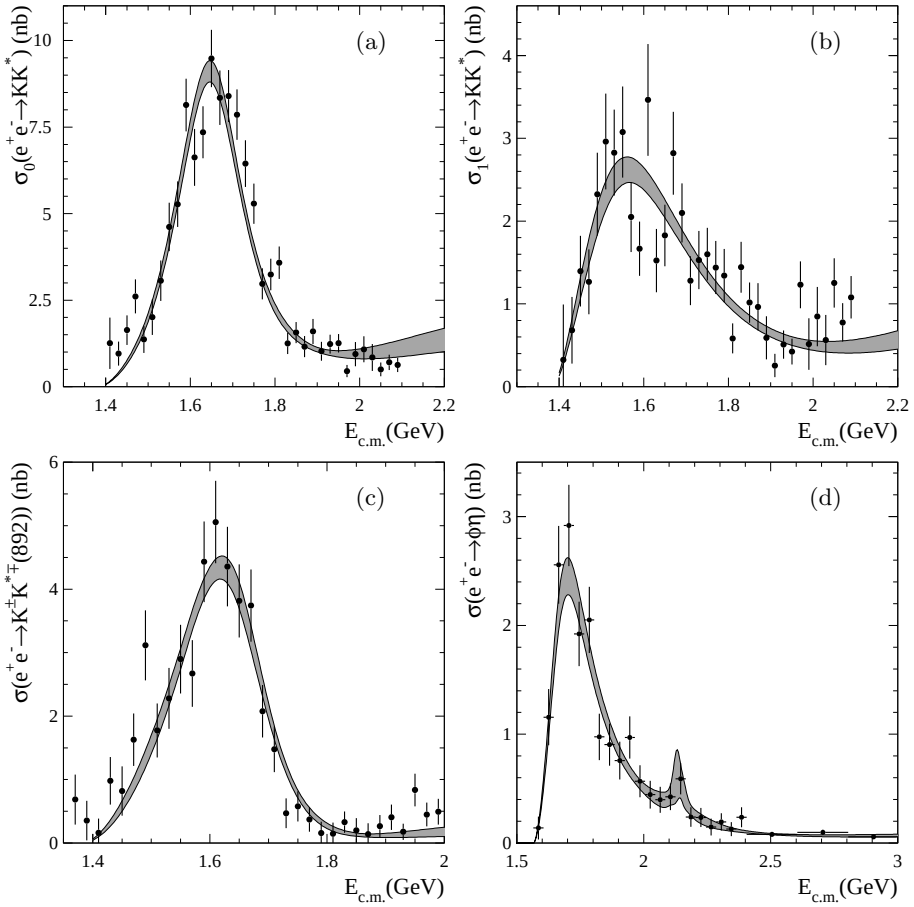


FIG. 29 Isoscalar (a) and isovector (b) components of the $e^+e^-\to K\bar{K}\pi$ cross section; the $e^+e^-\to K^\pm K^*(892)^\mp$ cross section obtained using $e^+e^-\to K^+K^-\pi^0$ events (c), and the $e^+e^-\to\phi\eta$ cross section (d) (Aubert *et al.*, 2008b). The points with error bars are data and the gray band represents the fit and its uncertainty.

TABLE I Parameters of the isoscalar and isovector resonances obtained in Ref. (Aubert *et al.*, 2008b) from the global fit to the isoscalar and isovector amplitudes using the $e^+e^- \to K^\pm K^*(892)^\mp, K^0_S K^\pm\pi^\mp$ and $e^+e^- \to \phi\eta$ cross sections.

R with $I=0$	ϕ'	ϕ''
$\Gamma^R_{ee}\mathcal{B}^R_{KK^*(892)}$(eV)	408 ± 49	-
$\Gamma^R_{ee}\mathcal{B}^R_{\phi\eta}$(eV)	172 ± 31	1.9 ± 1.0
m_R(MeV)	1723 ± 20	2139 ± 35
Γ_R(MeV)	371 ± 75	76 ± 62
R with $I=1$	ρ'	
$\Gamma^R_{ee}\mathcal{B}^R_{KK^*(892)}$(eV)	135 ± 12	
m_R(MeV)	1506 ± 16	
Γ_R(MeV)	437 ± 24	

state both the neutral $K^0\bar{K}^{*0}$ and charged $K^\pm K^{*\mp}$ combinations are involved. Since the $K^0\bar{K}^{*0}$ and $K^\pm K^{*\mp}$ amplitudes are the sum and the difference of the isovector and isoscalar amplitudes, respectively, the Dalitz plot population for the $K^0_S K^\pm\pi^\mp$ mode is asymmetric and strongly depends on isospin composition. From the Dalitz plot analysis the moduli and relative phase of the isoscalar and isovector amplitudes both for the $K\bar{K}^*(892)$ and $K\bar{K}^*_2(1430)$ intermediate states were determined. The obtained isoscalar and isovector $e^+e^- \to K\bar{K}^*(892)$ cross sections are shown in Fig. 29 (a,b).

The global fit to the $e^+e^- \to \phi(1020)\eta$ and $e^+e^- \to K^+K^-\pi^0$ cross sections, isovector and isoscalar $K\bar{K}^*(892)$ amplitudes, and their relative phase was performed to determine parameters of the ϕ and ρ excitations decaying into these final states. The fit results are shown in Fig. 29 and summarized in Table I. The obtained mass and width of the ϕ' and ρ' are in reasonable agreement with the parameters of the $\rho(1450)$ and $\phi(1680)$ resonances measured in other experiments (see Ref. (Amsler *et al.*, 2008) for references). The parameters of the ϕ'', which is seen in the $\phi\eta$ final state, are close to those for the $Y(2175)$ state observed in the $\phi f_0(980)$ final state. This state will be discussed in Sec. III.F.

E. $e^+e^- \to \pi^+\pi^-\pi^+\pi^-$, $\pi^+\pi^-2\pi^0$

The reactions $e^+e^- \to \pi^+\pi^-\pi^+\pi^-$, $\pi^+\pi^-2\pi^0$ have the largest cross sections in the energy region above the ϕ-meson resonance. They were studied with the BABAR detector (Aubert *et al.*, 2005b; Druzhinin, 2007) in the energy region below 4.5 GeV. Figures 30 and 31 show comparison of the BABAR results with the previous direct e^+e^- measurements, see Refs. (Achasov *et al.*, 2003; Akhmetshin *et al.*, 2004b; Bacci *et al.*, 1980; Bisello *et al.*, 1991a; Cordier *et al.*, 1982a; Cosme *et al.*, 1979; Dolinsky *et al.*, 1991; Kurdadze *et al.*, 1988)

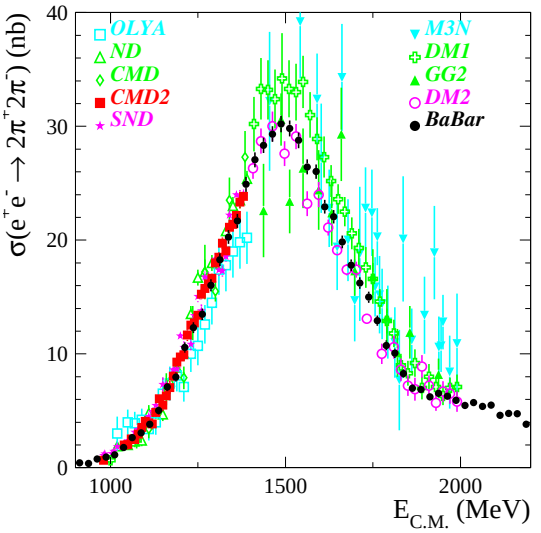


FIG. 30 Comparison of the BABAR results on the $e^+e^- \to \pi^+\pi^-\pi^+\pi^-$ cross section (Aubert *et al.*, 2005b) with the previous direct e^+e^-measurements (Achasov *et al.*, 2003; Akhmetshin *et al.*, 2004b; Bacci *et al.*, 1980; Bisello *et al.*, 1991a; Cordier *et al.*, 1982a; Cosme *et al.*, 1979; Dolinsky *et al.*, 1991; Kurdadze *et al.*, 1988).

for $\pi^+\pi^-\pi^+\pi^-$ and Refs. (Achasov *et al.*, 2003; Akhmetshin *et al.*, 1999; Bacci *et al.*, 1981; Bisello *et al.*, 1991a; Cosme *et al.*, 1979; Dolinsky *et al.*, 1991; Kurdadze *et al.*, 1986) for $\pi^+\pi^-2\pi^0$, in the energy range covered by these measurements. The large difference between the data sets from different experiments indicates that some previous measurements had large, up to 50%, unaccounted systematic errors. The BABAR systematic uncertainty on the $e^+e^- \to \pi^+\pi^-\pi^+\pi^-$ cross section is estimated to be about 5% in the 1–3 GeV energy range. For this channel the BABAR data are in good agreement with the recent SND (Achasov *et al.*, 2003) and CMD-2 (Akhmetshin *et al.*, 2004b) measurements at the energies below 1.4 GeV. The DM2 and BABAR data are also in reasonable agreement.

For the $\pi^+\pi^-2\pi^0$ channel the BABAR results are still preliminary. The estimated systematic uncertainty changes from 8% in the maximum of the cross section to 10% at 1 and 3 GeV.

At energies below 1.4 GeV the BABAR cross sections agree well with the results of the recent SND (Achasov *et al.*, 2003) and older OLYA (Kurdadze *et al.*, 1986) measurements, but not with the ND (Dolinsky *et al.*, 1991) and CMD-2 (Akhmetshin *et al.*, 1999) cross sections that may be affected by large unaccounted systematic errors as mentioned above.

The shape of the cross sections for both reactions shows wide structures peaked at about 1.5 GeV. Different intermediate states contribute to the $e^+e^- \to 4\pi$ cross sections. The observed bumps are sums of the contributions from the $\rho(770)$, $\rho(1450)$, and $\rho(1700)$ decays

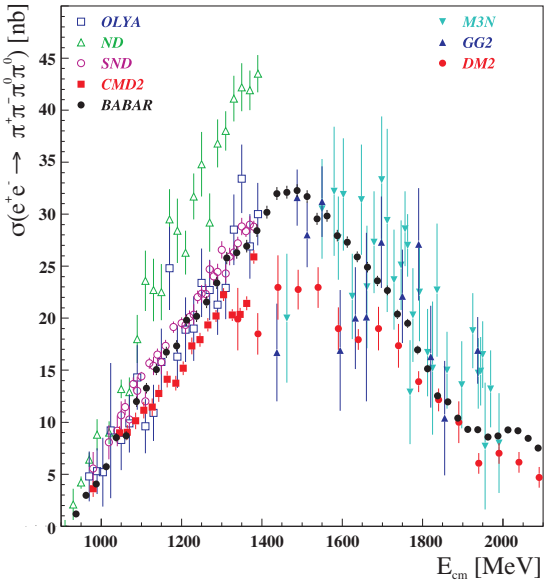


FIG. 31 Comparison of the BABAR results on the $e^+e^- \to \pi^+\pi^-2\pi^0$ cross section (Druzhinin, 2007) with the previous direct e^+e^-measurements (Achasov *et al.*, 2003; Akhmetshin *et al.*, 1999; Bacci *et al.*, 1981; Bisello *et al.*, 1991a; Cosme *et al.*, 1979; Dolinsky *et al.*, 1991; Kurdadze *et al.*, 1986).

into these intermediate states, which should be separated for a study of the excited ρ properties. Unfortunately, such analysis was performed at BABAR only at a qualitative level. The two- and three-pion mass distributions for the $\pi^+\pi^-\pi^+\pi^-$ final state are relatively well described by the model of the $a_1(1260)\pi$ intermediate state with a small contribution of the $f_0(1300)\rho$ state. This agrees with the $a_1\pi$ dominance hypothesis suggested in Ref. (Akhmetshin *et al.*, 1999) to describe the 4π dynamics at energies below 1.4 GeV. A strong deviation from this hypothesis is observed in the $\pi^+\pi^-2\pi^0$ channel. In addition to the expected $\omega\pi^0$ and $a_1\pi$ contributions, a surprisingly large contribution of the $\rho^+\rho^-$ intermediate state was observed. This is demonstrated in Fig. 32, where the 4π mass spectra for $\omega\pi$, non-$\omega\pi$, and $\rho^+\rho^-$ intermediate states are shown together with the total mass spectrum for the $e^+e^- \to \pi^+\pi^-2\pi^0$ reaction. The contributions of the different intermediate states were separated using simple conditions on 3π and 2π invariant masses. It is seen that the $\rho^+\rho^-$ cross section is more than a half of the non-$\omega\pi$ cross section at the energy about 1.7 GeV. For the $\pi^+\pi^-2\pi^0$ masses higher than 2.5 GeV/c^2 a clear signal of the $f_0(980)$ meson and a peak at the mass about 1.25 GeV/c^2 (probably from the $f_2(1270)$ meson) are seen in the $\pi^0\pi^0$ mass spectrum corresponding to the contributions of the $f_0(980)\rho$ and $f_2(1270)\rho$ intermediate states.

F. $e^+e^- \to K^+K^-\pi^+\pi^-$, $K^+K^-\pi^0\pi^0$

The $e^+e^- \to K^+K^-\pi^0\pi^0$ reaction has been never studied before the BABAR experiment (Aubert *et al.*, 2007b; Lees *et al.*, 2011), while the fully charged mode was previously measured with the DM1 detector (Cordier *et al.*, 1982b) but with an about 100 times smaller data set. The measured cross sections are shown in Figs. 33 and 34. The systematic uncertainties for these measurements are estimated to be at the (5–9)% level. The structures seen in the cross section energy dependence cannot be understood without analysis of intermediate states involved.

The distributions of the $K\pi$ invariant masses shown in Fig. 35 indicate that the $K^*(892)^0K^\pm\pi^\mp$ and $K^*(892)^\mp K^\pm\pi^0$ (similar plots are not shown) intermediate states dominate in these reactions. A small contribution of the $K_2^*(1430)K\pi$ state is also seen (Fig. 35(b)). A special correlation study (Lees *et al.*, 2011) showed that the intermediate state with two K^*, $K^*(892)\bar{K}^*(892)$, $K^*(892)\bar{K}_2^*(1430)$, and $K_2^*(1430)\bar{K}_2^*(1430)$, contributes less than 1% to the total reaction yield (the associated $K^*(892)\bar{K}_2^*(1430)$ production is observed in J/ψ decays). Taking the numbers of events in the K^* peaks for each c.m. energy interval, the "inclusive" $e^+e^- \to K^*(892)^0K\pi$ and $e^+e^- \to K_2^*(1430)^0K\pi$ cross sections shown in Fig. 36 were extracted. Figures 37(a) and 37(b) show scatter plots of the reconstructed a) $m(\pi^+\pi^-)$ and b) $m(\pi^0\pi^0)$ versus $m(K^+K^-)$ for selected events of the reactions $e^+e^- \to K^+K^-\pi^+\pi^-$ and $e^+e^- \to K^+K^-\pi^0\pi^0$, respectively. A clear $\phi(1020)$ signal is seen in the K^+K^- invariant mass in both figures and is discussed in more detail below. A signal of the $\rho(770)$ is observed in the $\pi^+\pi^-$ invariant mass distribution in Fig. 37(a). The $\pi^+\pi^-$ invariant mass distribution for $K^+K^-\pi^+\pi^-$ events not containing the $K^*(892)$ meson is shown in Fig. 38 (a). The $\rho(770)$ peak, probably corresponding to the intermediate $K_1(1230)^\pm$ and $K_1(1400)^\pm K^\mp$ states, is clearly seen in the $\pi^+\pi^-$ mass spectrum. In Fig. 38 (b) the "inclusive" cross section for the $K^+K^-\rho(770)$ reaction is presented. It is obtained by fitting the $\rho(770)$ signal in the $\pi^+\pi^-$ invariant mass distributions for each c.m. energy interval in Fig. 38.

One of the interesting ISR studies performed by BABAR (Aubert *et al.*, 2007b) and later reproduced by Belle (Shen *et al.*, 2009) is extracting relatively small contributions of the $\phi(1020)\pi^+\pi^-$, $\phi(1020)\pi^0\pi^0$, ($\phi \to K^+K^-$) intermediate states. Since the $\phi(1020)$ resonance is relatively narrow, the clean sample of $\phi\pi\pi$ events can be easily separated. Figure 39 shows the $m(\pi^+\pi^-)$ distribution for these events demonstrating a clear signal from the $f_0(980)$ resonance and a bump at lower masses which can be interpreted as the $f_0(600)$ state. A similar plot is obtained for the $\pi^0\pi^0$ invariant mass. These invariant mass distributions can be fitted with a superposition of two Breit-Wigner functions for the scalar $f_0(980)$ and $f_0(600)$ resonances as shown in Fig. 39. The $e^+e^- \to \phi(1020)\pi^+\pi^-$ cross section measured by

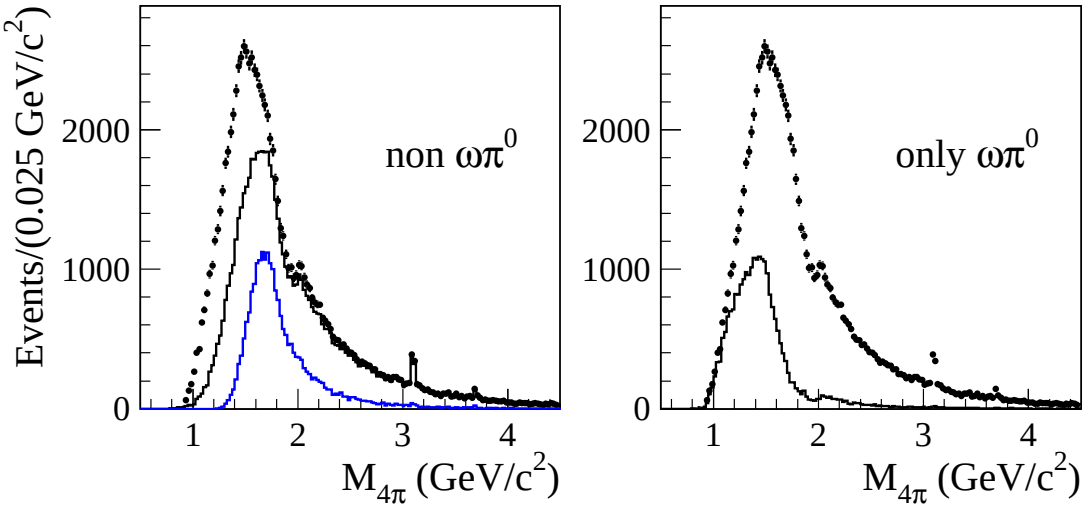


FIG. 32 The 4π invariant mass spectrum for selected $e^+e^- \to \pi^+\pi^- 2\pi^0$ events (Druzhinin, 2007) (points with error bars) in comparison with the spectrum for non-$\omega\pi^0$-events only (left) or with the spectrum for $\omega\pi^0$-events only (right). In the left plot the lowest histogram shows the contribution of the $\rho^+\rho^-$ intermediate state.

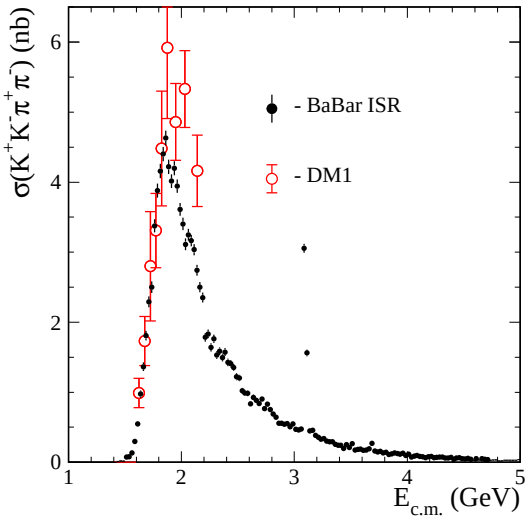


FIG. 33 The $e^+e^- \to K^+K^-\pi^+\pi^-$ cross section measured with the BABAR detector (Lees *et al.*, 2011) in comparison with the only previous measurement by DM1 (Cordier *et al.*, 1982b).

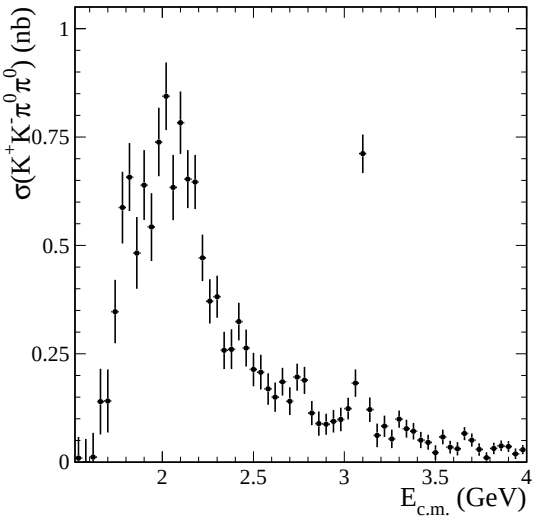


FIG. 34 The $e^+e^- \to K^+K^-\pi^0\pi^0$ cross section measured with the BABAR detector (Lees *et al.*, 2011).

BABAR and Belle is shown in Fig. 40. Two resonance structures are seen at 1.7 GeV and at 2.1 GeV. The BABAR Collaboration investigated decay mechanisms for these structures and concluded that the second structure decays only to the $\phi(1020)f_0(980)$ final state. The structure completely disappears if events associated with the $f_0(980)$ peak in the $m(\pi^+\pi^-)$ distribution are removed. The first structure is associated with the $\phi(1680)$, a radial excitation of the vector $s\bar{s}$ state. Its decays to $\phi(1020)f_0(600)$ and $\phi(1020)f_0(980)$ are not forbidden.

A simple VDM based model was suggested to describe the observed $e^+e^- \to \phi(1020)\pi^+\pi^-$ cross section.

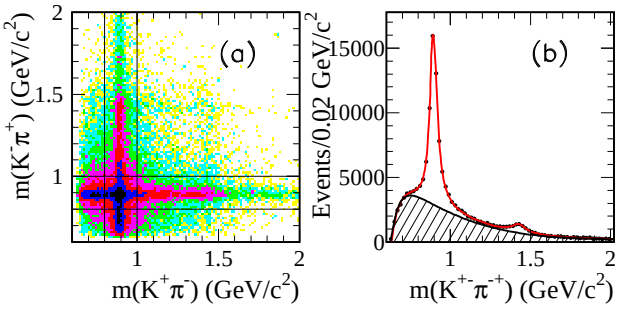


FIG. 35 (a) Scatter plots $m(K^-\pi^+)$ vs. $m(K^+\pi^-)$, and (b) projection $m(K^\pm\pi^\mp)$ plot (two entries per event) for the reaction $e^+e^- \to K^+K^-\pi^+\pi^-$ (Lees *et al.*, 2011). A sum over all accessible c.m. energies is given.

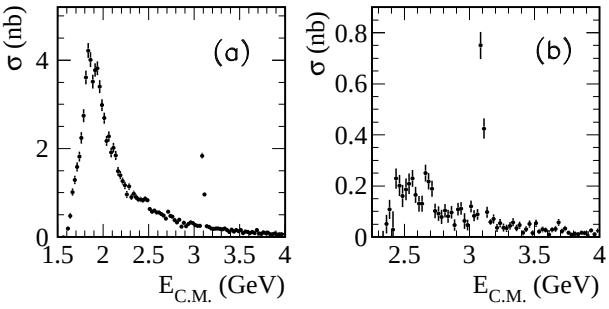


FIG. 36 (a) The $e^+e^- \to K^*(892)^0 K\pi$, and (b) $K_2^*(1430)^0 K\pi$ cross sections (Lees *et al.*, 2011) obtained from the $K^*(892)^0$ and $K_2^*(1430)^0$ signals of Fig. 35(b), respectively.

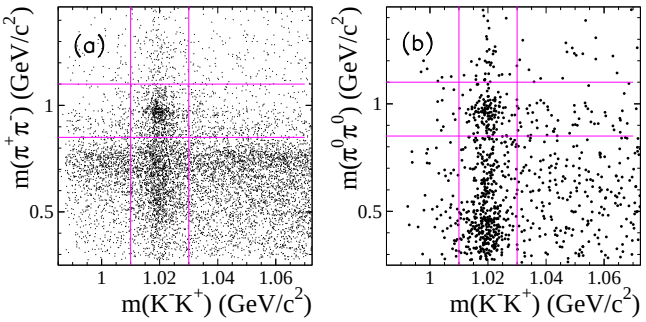


FIG. 37 The scatter plots of the reconstructed a) $m(\pi^+\pi^-)$ and b) $m(\pi^0\pi^0)$ versus $m(K^+K^-)$ for selected events in the data. The vertical (horizontal) lines bound a ϕ ($f_0(980)$) signal region (Lees *et al.*, 2011)..

The model assumes that two vector mesons contribute to the cross section; one resonance associated with the $\phi(1680)$ decays both to $\phi f_0(600)$ and to $\phi f_0(980)$, while another referred to as $Y(2175)$ decays to $\phi f_0(980)$ only. Since the nominal $\phi(1680)$ mass lies below the $\phi f_0(980)$ threshold, the $\phi(1680) \to \phi f_0(980)$ decay will reveal itself as a smooth bump in the energy dependence of the

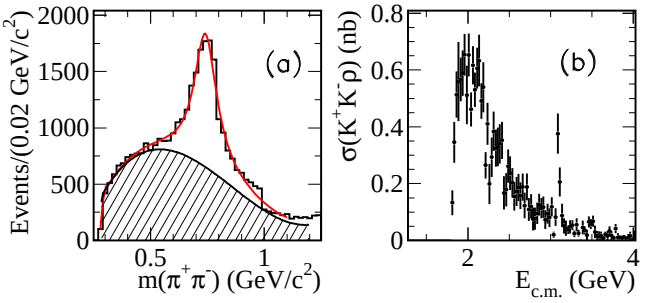


FIG. 38 (a) The $\pi^+\pi^-$ mass distribution for $K^+K^-\pi^+\pi^-$ events ($K^*(892)K\pi$ events are excluded); the solid curve represents a fit using a signal Breit-Wigner function with $\rho(770)$ parameters and a polynomial background (hatched area). (b) The $e^+e^- \to K^+K^-\rho(770)$ cross section obtained using the fitted numbers of ρ-meson events in each 25 MeV c.m. energy interval (Lees *et al.*, 2011).

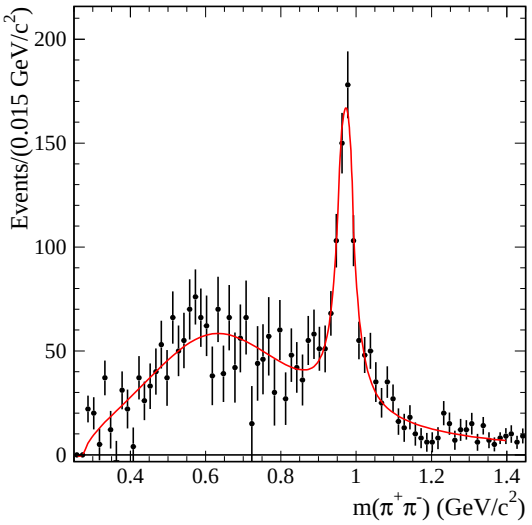


FIG. 39 The $m(\pi^+\pi^-)$ distribution for the $e^+e^- \to \phi(1020)\pi^+\pi^-$ reaction (Lees *et al.*, 2011).

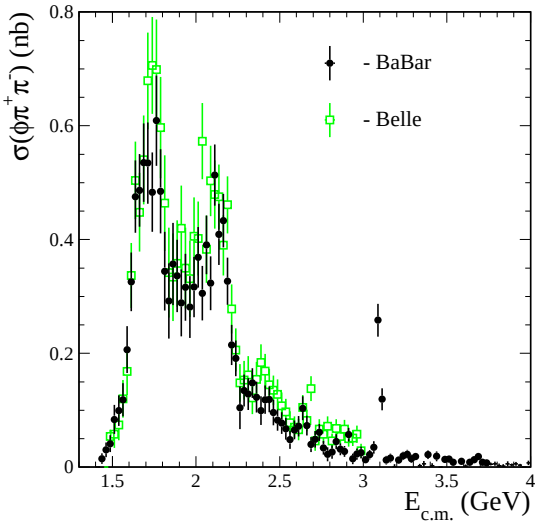


FIG. 40 The $e^+e^- \to \phi\pi^+\pi^-$ cross sections measured with the BABAR (Lees *et al.*, 2011) (circles) and Belle (Shen *et al.*, 2009) (squares) detectors.

$e^+e^- \to \phi f_0(980)$ cross section above 2 GeV. The result of the fit to the $e^+e^- \to \phi(1020)\pi^+\pi^-$ cross section with this model is shown in Fig. 41. It is clearly seen that the data above 2 GeV cannot be described with a contribution of the $\phi(1680)$ resonance only. An additional relatively narrow resonance $Y(2175)$ is needed to do this. The tongue below 2 GeV in the cross section for the reaction $e^+e^- \to \phi(1680) \to \phi f_0(980)$ in Fig. 41 is due to the finite width of the $f_0(980)$ state.

A relatively clean sample of $\phi f_0(980)$ events is selected using the requirement $0.85\text{GeV}/c^2 < m(\pi\pi) < 1.1$ GeV/c^2. The cross section for events of the $K^+K^-\pi^+\pi^-$ mode, fitted with the model described above, is shown

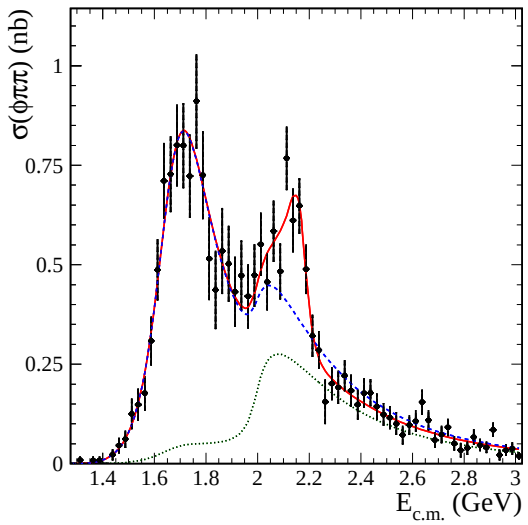


FIG. 41 The fit to the $e^+e^- \to \phi\pi^+\pi^-$ cross section (Lees *et al.*, 2011) in the two-resonance model described in the text (solid curve). The contribution of the first resonance ($\phi(1680)$) is shown by the dashed line. The dotted line shows the first resonance contribution in the $\phi f_0(980)$ decay mode only.

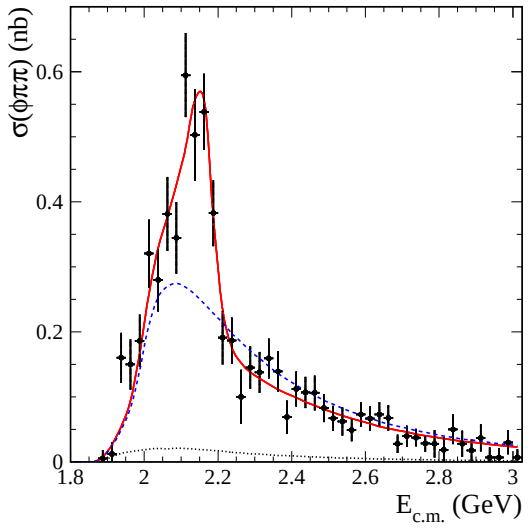


FIG. 42 The cross section for $e^+e^- \to \phi(1020)f_0(980)$ events selected with the cut $0.85 < m(\pi\pi) < 1.1$ GeV/c^2 (Lees *et al.*, 2011). The solid curve is the result of the two-resonance fit. The dashed and dotted curves are the contributions of the $\phi(1680) \to \phi f_0(980)$ and $\phi(1680) \to \phi f_0(600)$ decay channels, respectively.

in Fig. 42. The contribution of the $Y(2175)$ is seen much better with this selection. The comparison of the $e^+e^- \to \phi f_0(980)$ cross sections measured by BABAR in two $f_0(980)$ decay modes, $\pi^+\pi^-$ and $\pi^0\pi^0$, is shown in Fig. 43. It is seen that two measurements agree. The fit of two modes gives the peak cross section, mass and

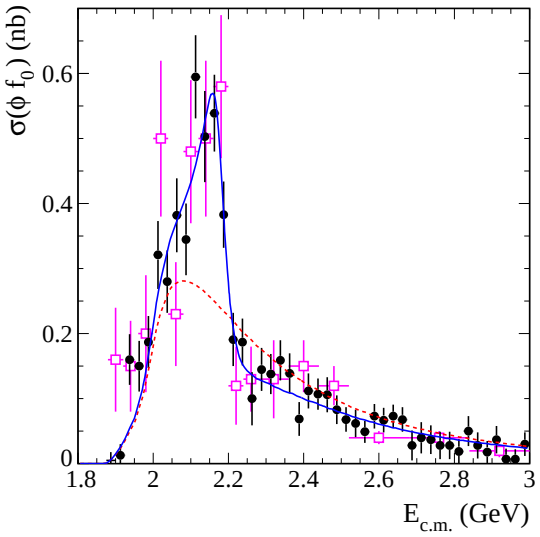


FIG. 43 The $e^+e^- \to \phi(1020)f_0(980)$ cross section measured in the $K^+K^-\pi^+\pi^-$ (circles) and $K^+K^-\pi^0\pi^0$ (squares) final states by BABAR (Lees *et al.*, 2011). The solid and dashed curves represent the results of the two-resonance fit described in the text.

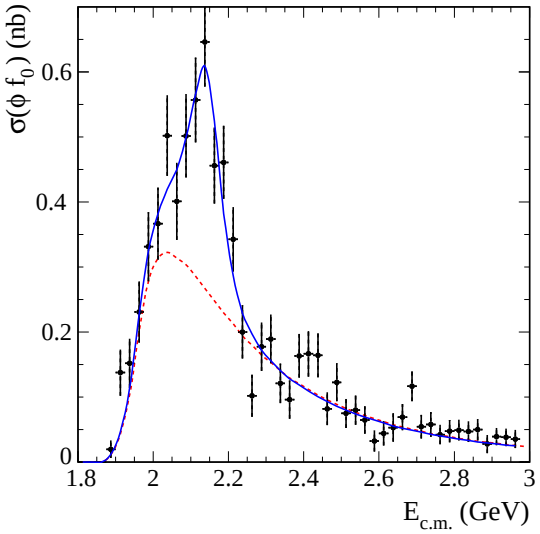


FIG. 44 The $e^+e^- \to \phi(1020)f_0(980)$ cross section measured by Belle (Shen *et al.*, 2009). The solid and dashed curves represent the results of the two-resonance fit described in the text.

width of the resonance:

$$\begin{aligned} \sigma_Y &= 0.104 \pm 0.025 \text{ nb}, \\ m_Y &= 2.179 \pm 0.009 \text{ GeV}/c^2, \\ \Gamma_Y &= 0.079 \pm 0.017 \text{ GeV}. \end{aligned}$$

The $e^+e^- \to \phi f_0(980)$ cross section measured in the Belle experiment (Shen *et al.*, 2009) is shown in Fig. 44, and also requires a resonance structure with similar parameters. Some properties of this resonance, a relatively

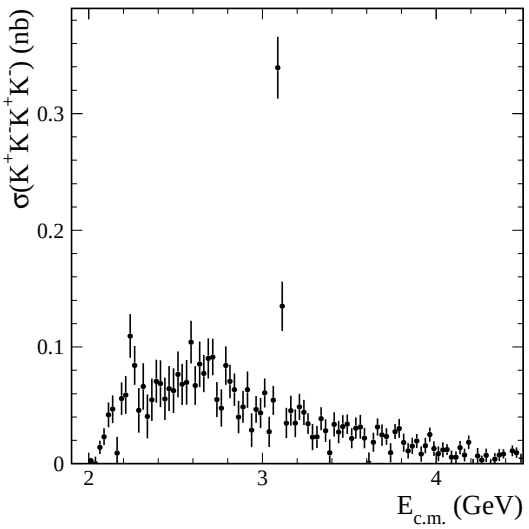


FIG. 45 The $e^+e^- \to 2(K^+K^-)$ cross section as a function of c.m. energy measured with the BABAR detector using ISR (Aubert *et al.*, 2007b).

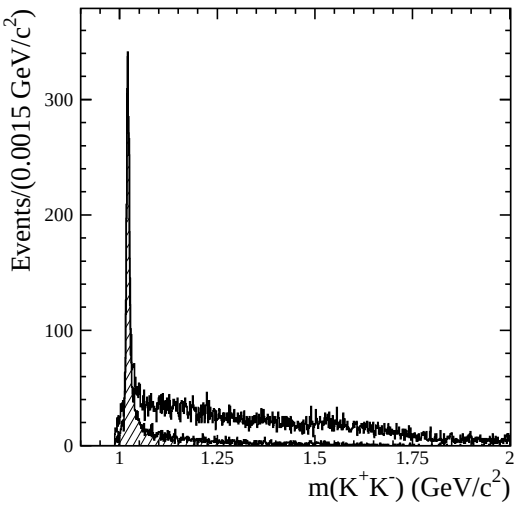


FIG. 46 The K^+K^- invariant mass distribution for selected $e^+e^- \to 2(K^+K^-)$ events (Aubert *et al.*, 2007b) (open histogram, four entries per event), and that for the combination in each event closest to the ϕ-meson mass (hatched histogram).

small width and absence of the $\phi f_0(600)$ decay, are unusual.

The nature of this state is not clear (Gomez-Avila *et al.*, 2009; Napsuciale *et al.*, 2007). One of the possible interpretations is that the $Y(2175)$ is a $s\bar{s}s\bar{s}$ four-quark state. Indeed, the $f_0(600)$ does not contain strange quarks, while the $f_0(980)$, strongly coupled with $K\bar{K}$, definitely contains them. For the $s\bar{s}s\bar{s}$ state, the observed $Y(2175) \to \phi f_0(980)$ is natural decay, while the not seen $Y(2175) \to \phi f_0(600)$ transition is suppressed by the OZI rule. The observation of the $Y(2175)$ decay to the $\phi\eta$ final state containing four s quarks, also supports this hypothesis.

G. $e^+e^- \to 2(K^+K^-)$

The reaction $e^+e^- \to 2(K^+K^-)$ was studied for the first time by BABAR (Aubert *et al.*, 2007b). The measured cross section is shown in Fig. 45. The most significant structure in the cross sections is due to the J/ψ decay. It is natural to expect that intermediate states for this reaction contain the $\phi(1020)$ meson which has a large decay rate to K^+K^-. Indeed, the strong ϕ meson peak is seen in the K^+K^- invariant mass distribution shown in Fig. 46. Since the ϕ meson is present in almost each four-kaon event, it is concluded that the reaction $e^+e^- \to 2(K^+K^-)$ is strongly dominated by the ϕK^+K^- production.

A study of events containing the ϕ meson was performed by BABAR. The K^+K^- pair forming the ϕ meson is selected by the requirement that its invariant mass is within ± 10 MeV of the ϕ nominal mass. The invariant mass distribution for the second K^+K^- pair is shown in Fig. 47(a). Figures 47(b,c,d) show the cross section for events with the K^+K^- invariant mass in the regions 1, 2, and 3 indicated in Fig. 47(a). An enhancement in the K^+K^- invariant mass spectrum near the K^+K^- threshold can be interpreted as being due to decay $f_0(980) \to K^+K^-$. Therefore, the cross section for the region 1 is expected to have a structure similar to that observed in $e^+e^- \to \phi f_0 \to K^+K^-\pi\pi$ (see Sec. III.F). The bump at 2.175 GeV is indeed seen in the cross section shown in Fig. 47(b), however, the data sample is too low to perform a quantitative analysis.

The relatively narrow region 2 with $1.06\ \mathrm{GeV}/c^2 < m(K^+K^-) < 1.2\ \mathrm{GeV}/c^2$ is responsible for the spike seen at 2.25 GeV in Fig. 45. The spike is much more significant in Fig. 47 (c) showing the cross section for events from this mass region. There is no explanation of this structure.

The peak in the K^+K^- mass spectrum near 1.5 GeV/c^2 is associated with the $f_2'(1525)$. The region 3 ($1.45\ \mathrm{GeV}/c^2 < m(K^+K^-) < 1.6\ \mathrm{GeV}/c^2$) is chosen to select $\phi f_2'(1525)$ events. The cross section for this mass region is shown in Fig. 47(d) and exhibits a broad structure at 2.7 GeV and a strong J/ψ signal.

H. $e^+e^- \to 5$ mesons

The BABAR detector studied a number of ISR reactions with five hadrons in the final state: $2(\pi^+\pi^-)\pi^0$, $2(\pi^+\pi^-)\eta$, $K^+K^-\pi^+\pi^-\pi^0$, and $K^+K^-\pi^+\pi^-\eta$ (Aubert *et al.*, 2007c).

The $e^+e^- \to 2(\pi^+\pi^-)\pi^0$ reaction has the largest cross section among the processes mentioned above. In the $\pi^+\pi^-\pi^0$ invariant mass spectrum for this re-

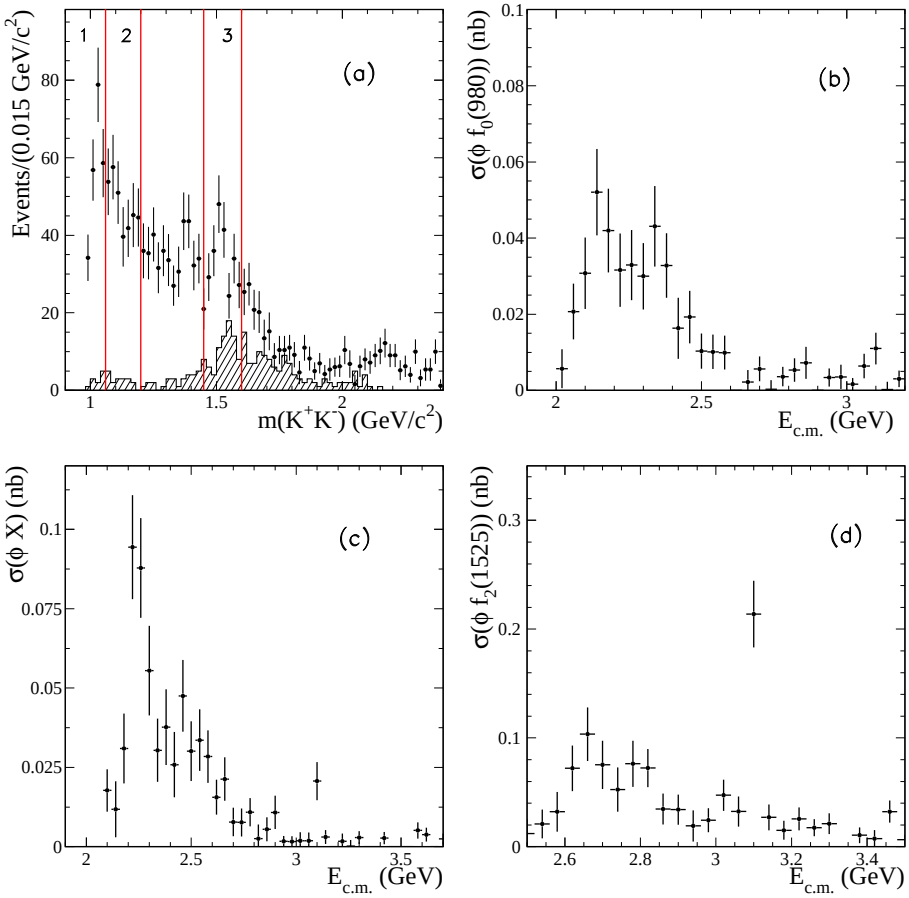


FIG. 47 The K^+K^- invariant mass distribution for ϕK^+K^- events (Aubert *et al.*, 2007b) (a). Events from the $J/\psi \to \phi K^+K^-$ decay are excluded from the spectrum shown by the open histogram. The hatched histogram is for events from the J/ψ decay. The numbered regions of the K^+K^- mass spectrum are used to calculate the cross sections shown in the plots (b), (c), and (d) for the regions 1, 2, and 3, respectively.

action (Fig. 48) clear signals of η and ω mesons are seen corresponding to the $\omega\pi^+\pi^-$ and $\eta\pi^+\pi^-$ intermediate states. The cross sections for these reactions were measured in direct e^+e^-experiments (Akhmetshin *et al.*, 2000; Antonelli *et al.*, 1988, 1992; Cordier *et al.*, 1981; Druzhinin *et al.*, 1986), but BABAR data are significantly more accurate. The $e^+e^- \to \eta\pi^+\pi^-$ and $e^+e^- \to \omega\pi^+\pi^-$ cross sections measured by BABAR and in direct e^+e^-experiments are shown in Fig. 49 and Fig. 50, respectively.

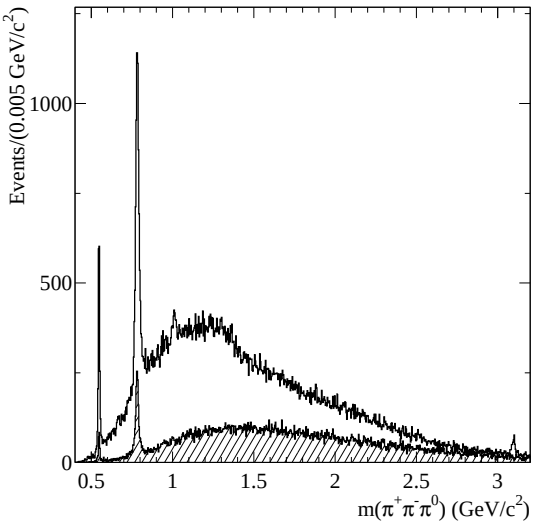


FIG. 48 The $m(\pi^+\pi^-\pi^0)$ distribution for $2(\pi^+\pi^-)\pi^0$ events (Aubert *et al.*, 2007c).

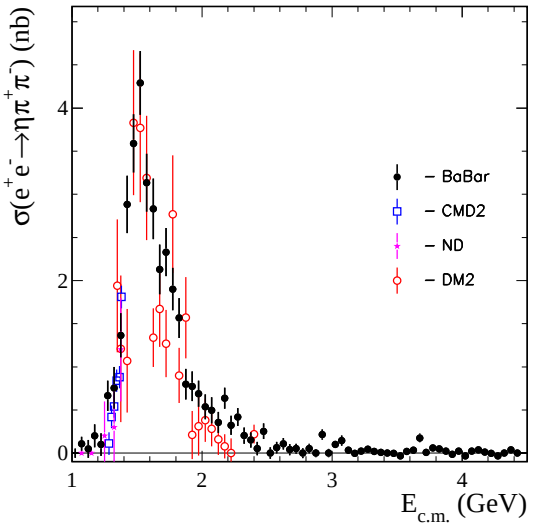


FIG. 49 The $e^+e^- \to \eta\pi^+\pi^-$ cross section measured by BABAR (Aubert *et al.*, 2007c) in comparison with the direct e^+e^-measurements (Akhmetshin *et al.*, 2000; Antonelli *et al.*, 1992; Druzhinin *et al.*, 1986).

The two pions from the reaction $e^+e^- \to \eta\pi^+\pi^-$ predominantly form the $\rho(770)$. In the two-pion invariant mass spectrum for the $e^+e^- \to \omega\pi^+\pi^-$ reaction shown in Fig. 51 a clear $f_0(980)$ signal is observed. The contribution of the $\omega f_0(980)$ intermediate state was extracted, and the cross section $e^+e^- \to \omega f_0(980)$ was measured for the first time. It is shown in Fig. 52. The $e^+e^- \to \omega\pi^+\pi^-$ cross section after subtraction of the $\omega f_0(980)$ contribution is shown in Fig. 53. The cross section is fitted with a sum of of two resonances. The fit result is shown in Fig. 53 and listed in Table II. The obtained parameters are in good agreement with

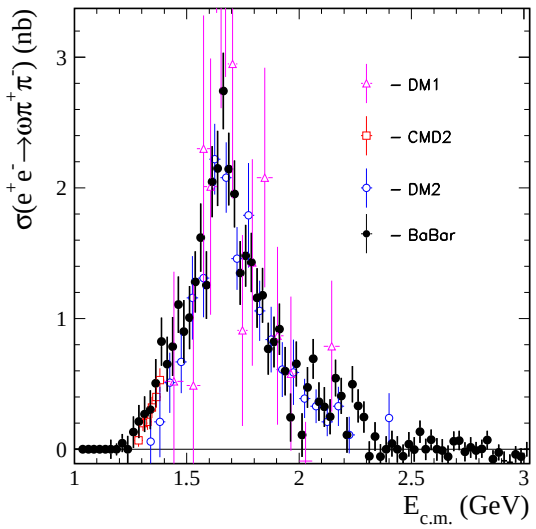


FIG. 50 The $e^+e^- \to \omega\pi^+\pi^-$ cross section measured by BABAR (Aubert *et al.*, 2007c) in comparison with the direct e^+e^-measurements (Akhmetshin *et al.*, 2000; Antonelli *et al.*, 1988; Cordier *et al.*, 1981).

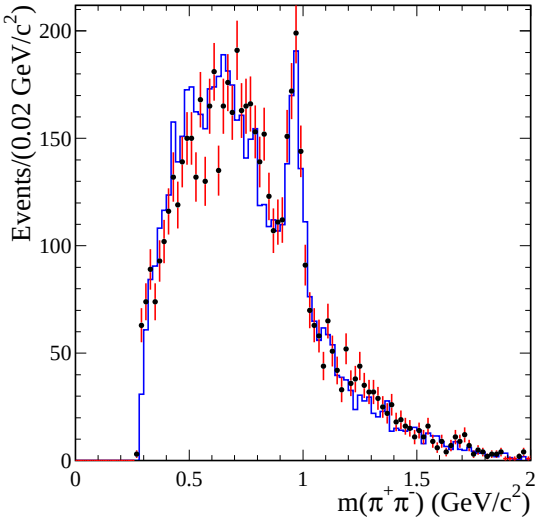


FIG. 51 The $m(\pi^+\pi^-)$ distribution for selected $\omega\pi^+\pi^-$ events in data (points with error bars) and in simulation (histogram) (Aubert *et al.*, 2007c).

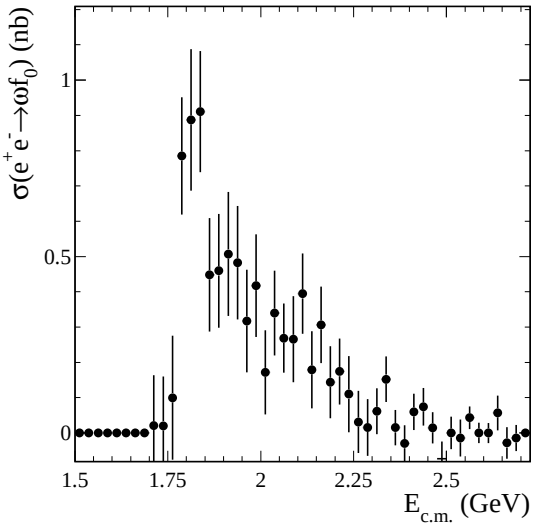


FIG. 52 The $e^+e^- \to \omega f_0(980)$ cross section measured by BABAR (Aubert *et al.*, 2007c).

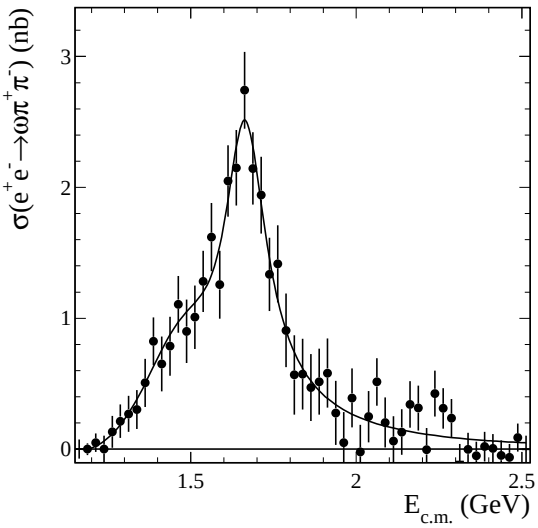


FIG. 53 The fit with two Breit-Wigner functions to the $\omega\pi^+\pi^-$ cross section with the $\omega f_0(980)$ contribution subtracted (Aubert *et al.*, 2007c).

those obtained for the $\pi^+\pi^-\pi^0$ channel (see discussion in Sec. III.J).

The $\omega\pi^+\pi^-$ and $\eta\pi^+\pi^-$ intermediate states do not saturate the total $e^+e^- \to 2(\pi^+\pi^-)\pi^0$ cross section as shown in Fig. 54. The $m(\pi^+\pi^-)$ and $m(\pi^\pm\pi^0)$ distributions for $e^+e^- \to 2(\pi^+\pi^-)\pi^0$ events with the $\omega\pi^+\pi^-$ and $\eta\pi^+\pi^-$ contributions excluded are shown in Fig. 55. From the analysis of these two-pion mass distributions it was concluded that the dominant intermediate state for these events is $\rho^0\rho^\pm\pi^\mp$. The $\rho\pi$ mass spectrum also exhibits a resonance structure with the parameters:

$$m_X = 1.243 \pm 0.012 \pm 0.020 \text{ GeV}/c^2;$$
$$\Gamma_X = 0.410 \pm 0.031 \pm 0.030 \text{ GeV}.$$

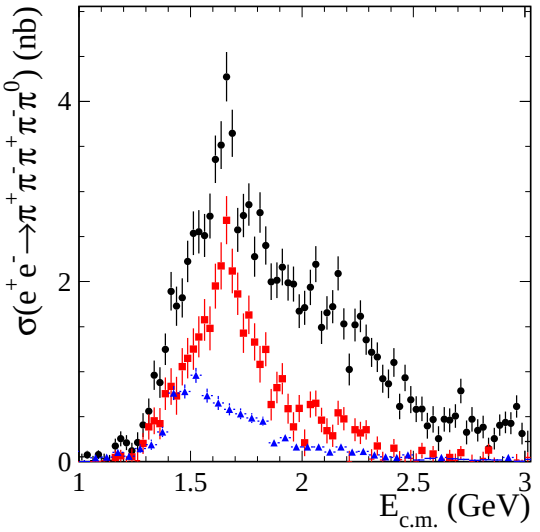


FIG. 54 The $e^+e^- \to 2(\pi^+\pi^-)\pi^0$ cross section (Aubert *et al.*, 2007c) and contributions from $\omega\pi^+\pi^-$(squares) and $\eta\pi^+\pi^-$(triangles).

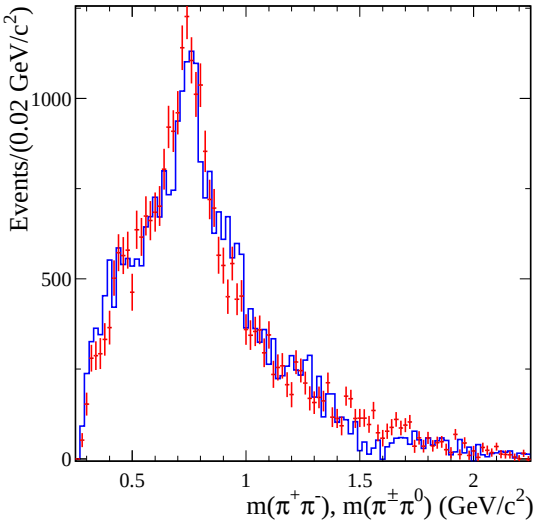


FIG. 55 The $m(\pi^+\pi^-)$ (points) and $m(\pi^\pm\pi^0)$ (histogram) distributions for $2(\pi^+\pi^-)\pi^0$ events with the $\omega\pi^+\pi^-$ and $\eta\pi^+\pi^-$ contributions excluded (Aubert *et al.*, 2007c).

The yield of the $X(1240)$ state is consistent with the complete dominance of the quasi-two-body reaction $e^+e^- \to \rho(770)X(1240) \to \rho^0\rho^\pm\pi^\mp$. The best candidates for $X(1240)$ are the $\pi(1300)$ or $a_1(1260)$ resonances (Amsler *et al.*, 2008).

The $e^+e^- \to 2(\pi^+\pi^-)\eta$ reaction was studied for the first time by BABAR. The measured cross section is shown in Fig. 56. A rich internal structure is expected for the $4\pi\eta$ final state. The four-pion mass distribution exhibits a wide resonance structure which can be a mixture of the known $\rho(1450)$ and $\rho(1700)$ resonances. Figure 57(a) shows the $\eta\pi^+\pi^-$ mass distribution with two

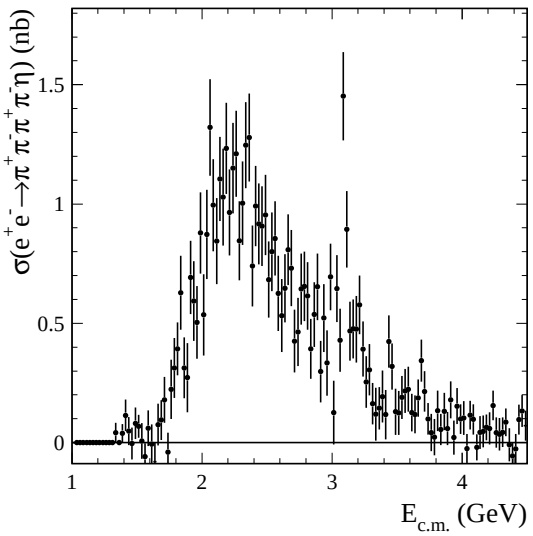


FIG. 56 The $e^+e^- \to 2(\pi^+\pi^-)\eta$ cross section measured by BABAR (Aubert *et al.*, 2007c).

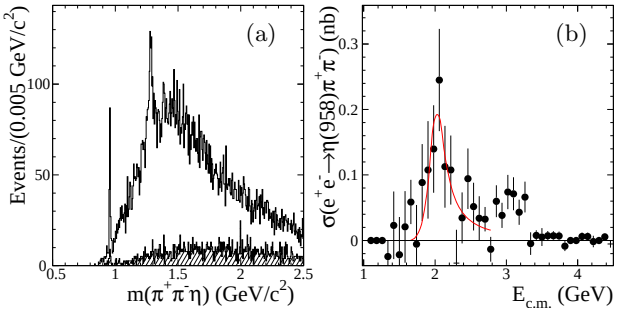


FIG. 57 (a) The $m(\eta\pi^+\pi^-)$ distribution for $2(\pi^+\pi^-)\eta$ events; (b) The $e^+e^- \to \eta(958)\pi^+\pi^-$ cross section and the result of the Breit-Wigner fit (Aubert *et al.*, 2007c).

narrow peaks. The lowest mass peak corresponds to the $\eta'(958)$. The measured $e^+e^- \to \eta'(958)\pi^+\pi^-$ cross section is shown in Fig. 57(b). The resonance-like structure observed in the cross section energy dependence is fitted with a single Breit-Wigner function. The fitted resonance parameters are

$$\begin{aligned} \sigma_0 &= 0.18 \pm 0.07 \text{ nb}, \\ m_x &= 1.99 \pm 0.08 \text{ GeV}/c^2, \\ \Gamma_x &= 0.31 \pm 0.14 \text{ GeV}. \end{aligned}$$

There is no entry for these parameters in the current PDG tables (Amsler *et al.*, 2008). Taking into account possible large systematic uncertainties on mass and width, the observed resonance can be interpreted as the $\rho(2150)$, extensively discussed in the past (Amsler *et al.*, 2008).

Another clear structure seen in the $\eta\pi^+\pi^-$ mass distribution (Fig. 57(a)) and shown in detail in Fig. 58(a) was interpreted as the $f_1(1285)$ meson. The measured $e^+e^- \to f_1(1285)\pi^+\pi^-$ cross section is shown in

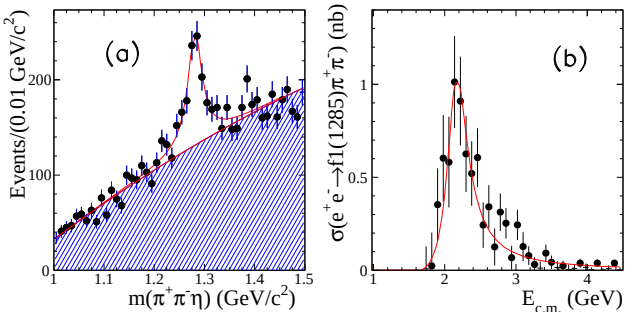


FIG. 58 (a) The $m(\eta\pi^+\pi^-)$ distribution for $2(\pi^+\pi^-)\eta$ events; (b) The $e^+e^- \to f_1(1285)\pi^+\pi^-$ cross section and the result of the Breit-Wigner fit (Aubert *et al.*, 2007c).

Fig. 58(b). The observed resonance structure has parameters:

$$\begin{aligned} \sigma_0 &= 1.00 \pm 0.18 \pm 0.15 \text{ nb}, \\ m_x &= 2.15 \pm 0.04 \pm 0.05 \text{ GeV}/c^2, \\ \Gamma_x &= 0.35 \pm 0.04 \pm 0.05 \text{ GeV}. \end{aligned}$$

The mass and width are close to those measured in the reaction $e^+e^- \to \eta'(958)\pi^+\pi^-$, but the cross section is significantly larger. The observed structure can also be assigned to the $\rho(2150)$ resonance.

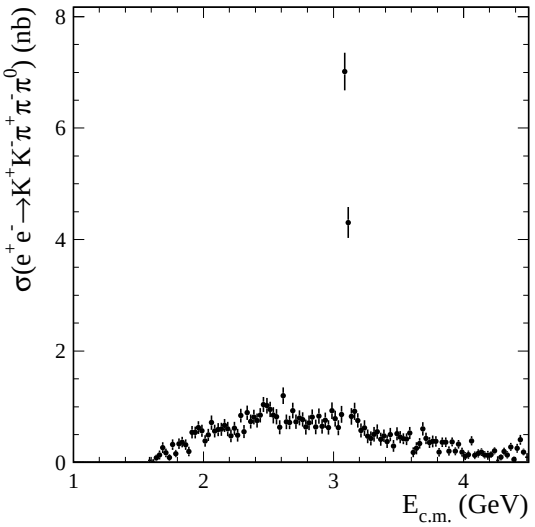


FIG. 59 The $e^+e^- \to K^+K^-\pi^+\pi^-\pi^0$ cross section measured by BABAR (Aubert *et al.*, 2007c).

The cross section for the reaction $e^+e^- \to K^+K^-\pi^+\pi^-\pi^0$ shown in Fig. 59 was also measured by BABAR for the first time. The three-pion and two-kaon invariant mass spectra for this reaction are shown in Fig. 60. Clear η and ω signals are seen in the three-pion mass distribution and a strong ϕ signal in the K^+K^- mass distribution. Figure 61 shows the calculated cross sections for the $e^+e^- \to \phi\eta$ (a) and $e^+e^- \to \omega K^+K^-$ (b) subprocesses. The former is in good agreement with that

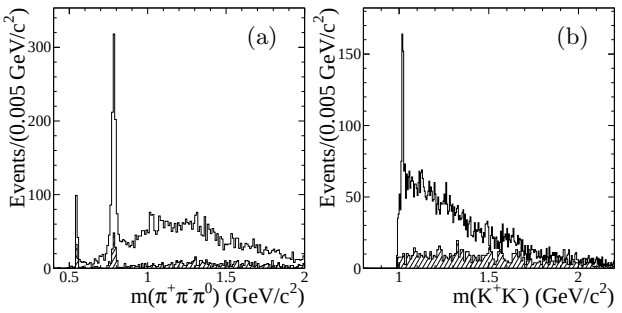


FIG. 60 The $m(\pi^+\pi^-\pi^0)$ (a) and $m(K^+K^-)$ (b) distributions for $K^+K^-\pi^+\pi^-\pi^0$ events (Aubert *et al.*, 2007c). The hatched histogram represents the estimated non-ISR background.

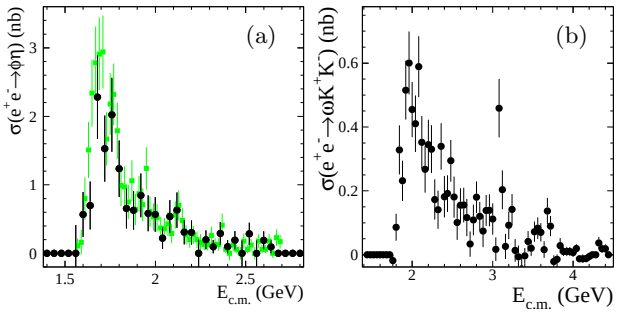


FIG. 61 (a) The $e^+e^- \to \phi\eta$ cross section measured by BABAR in the $K^+K^-\pi^+\pi^-\pi^0$ (Aubert *et al.*, 2007c) (circles) and $K^+K^-\gamma\gamma$ (squares) (Aubert *et al.*, 2008b) final states. (b) The cross sections for the $e^+e^- \to \omega K^+K^-$ process measured by BABAR (Aubert *et al.*, 2007c).

obtained in the $\eta \to \gamma\gamma$ mode (Aubert *et al.*, 2008b). It is a first observation of the process $e^+e^- \to \omega K^+K^-$.

The reaction $e^+e^- \to K^+K^-\pi^+\pi^-\eta$ was also studied by BABAR in Ref. (Aubert *et al.*, 2007c). The measured cross section is small and rises from threshold to a maximum value of about 0.2 nb at 2.8 GeV, followed by a monotonic decrease with increasing energy. The clear signal of the $\phi\eta'(958)$ intermediate state is observed in the K^+K^- and $\pi^+\pi^-\eta$ mass distributions. Unfortunately, the $\phi\eta'(958)$ invariant mass spectrum is not shown in Ref. (Aubert *et al.*, 2007c). This spectrum is interesting since for the four-quark $Y(2175)$ resonance (Sec. III.F) the decay to $\phi\eta'(958)$ is expected.

I. $e^+e^- \to 3(\pi^+\pi^-)$, $2(\pi^+\pi^-\pi^0)$

The reactions $e^+e^- \to 3(\pi^+\pi^-)$ and $e^+e^- \to 2(\pi^+\pi^-\pi^0)$ were studied before in a number of direct e^+e^- experiments, but with limited data samples (Bacci *et al.*, 1981; Baldini *et al.*, 1988; Bisello *et al.*, 1981; Cosme *et al.*, 1979; Esposito *et al.*, 1981). The BABAR detector studied the six-pion production using the ISR method from the threshold to 4.5 GeV (Aubert *et al.*, 2006b). As a result, the statistical and systematic uncertainties on the cross sections were dramatically reduced.

An interesting feature of the $3(\pi^+\pi^-)$ final state is the presence, among many $\pi^+\pi^-$ combinations, of only one $\rho(770)^0$ per event. No other intermediate resonance signals were observed. For the $2(\pi^+\pi^-\pi^0)$ final state also one $\rho(770)$ only, neutral or charged, per event is observed in the expected proportion 1 : 2.

In the $2(\pi^+\pi^-\pi^0)$ final state, η and ω signals are seen in the $\pi^+\pi^-\pi^0$ invariant mass distribution. A small fraction of events corresponds to the associated production of the η and ω. Selecting these $\eta\omega$ events the $e^+e^- \to \omega\eta$ cross section shown in Fig. 62 (left) was measured for the first time. The observed resonance structure which is expected to be the $\omega(1650)$ is fitted with a Breit-Wigner function. The fitted curve is shown in Fig. 62 (left). The obtained resonance parameters are listed in Table II together with the resonance parameters obtained from the fits to $e^+e^- \to 3\pi$ and $e^+e^- \to \omega\pi\pi$ cross sections (see discussion in Sec. III.J). Comparison of the $\omega 3\pi$ and $\omega(782)\eta$ contributions with the total $e^+e^- \to 2(\pi^+\pi^-\pi^0)$ cross section is shown in Fig. 62(right).

The total $e^+e^- \to 2(\pi^+\pi^-\pi^0)$ and $e^+e^- \to 3(\pi^+\pi^-)$ cross sections shown in Fig. 63 have very similar energy dependence. The ratio of the cross sections is almost constant over the energy range under study. Its average value is equal to $3.98 \pm 0.06 \pm 0.41$. A dip structure just below 2 GeV in the six-pion cross section was observed in the DM2 experiment (Baldini *et al.*, 1988) and then confirmed in the diffractive photoproduction of six pions in the FOCUS experiment (Frabetti *et al.*, 2000). Such a dip at 1.9 GeV was also observed in the total cross section of e^+e^- annihilation into hadrons by the FENICE detector (Antonelli *et al.*, 1996). This structure in BABAR data is fitted using the Breit-Wigner function coherent with the smooth non-resonant background. The fitted curves for both cross sections are shown in Fig. 63. The following "resonance" parameters are obtained:

$$\begin{aligned} m_{6\pi} &= 1.88 \pm 0.03 \text{ GeV}/c^2, \\ m_{4\pi 2\pi^0} &= 1.86 \pm 0.02 \text{ GeV}/c^2, \\ \Gamma_{6\pi} &= 0.13 \pm 0.03 \text{ GeV}, \\ \Gamma_{4\pi 2\pi^0} &= 0.16 \pm 0.02 \text{ GeV}. \end{aligned}$$

The parameter values seem to be essentially independent of the final-state charge combination. These values may be also compared with those obtained in the FOCUS experiment (Frabetti *et al.*, 2000): $m = 1.91 \pm 0.01$ GeV/c^2, $\Gamma = 0.037 \pm 0.013$ GeV. The mass values are consistent, but the widths obtained by BABAR are substantially larger. Note that typical widths of known isovector resonances with mass near 2 GeV/c^2 are 200–300 MeV. Since the obtained mass of the resonance structure is close to the double proton mass, it may be interpreted as a proton-antiproton subthreshold bound state (Datta and O'Donnell, 2003).

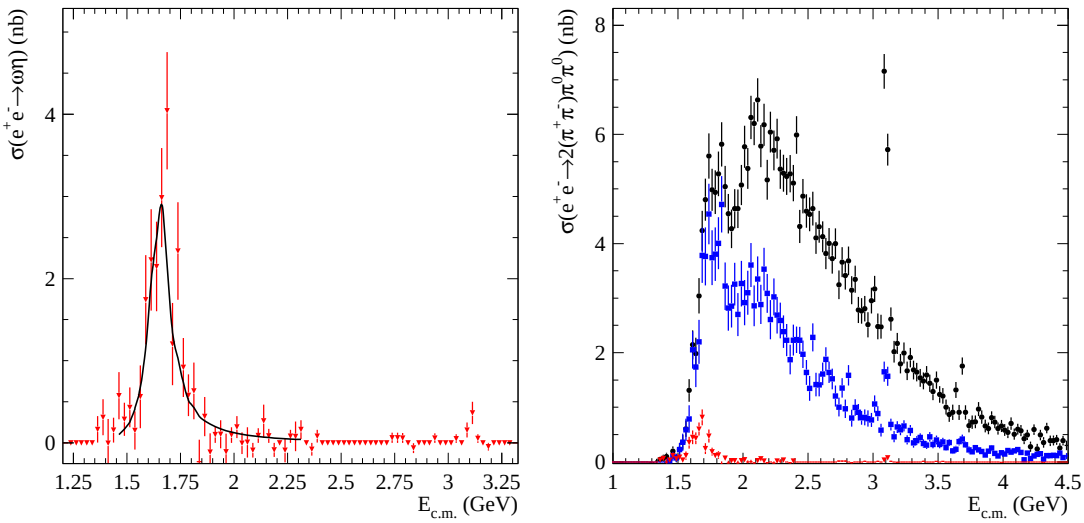


FIG. 62 The $e^+e^- \to \omega\eta$ cross section (left) and contribution of $e^+e^- \to \omega\pi^+\pi^-\pi^0$ (squares) and $e^+e^- \to \omega\eta$ (triangles) cross sections to all $e^+e^- \to 2(\pi^+\pi^-\pi^0)$ events (right) (Aubert *et al.*, 2006b).

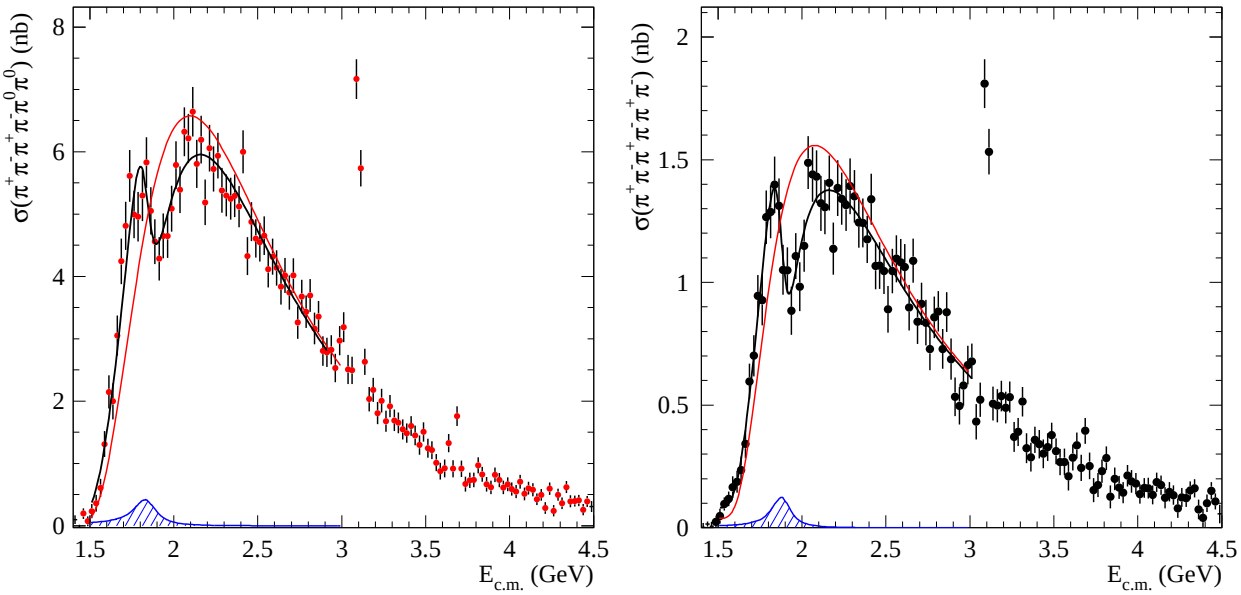


FIG. 63 The $e^+e^- \to 2(\pi^+\pi^-\pi^0)$ cross section (left) and the $e^+e^- \to 3(\pi^+\pi^-)$ cross section (right) with a fit to the (anti-)resonance function (Aubert *et al.*, 2006b). A resonance responsible for the "dip" is shown shaded.

J. Summary

The BABAR ISR study covers the low energy range of e^+e^- interactions from the 2π threshold to 4.0–4.5 GeV with exclusively measured cross sections for many processes. Figure 64 shows all exclusive cross sections measured by BABAR in a single plot. One can see that in most of the cases cross sections strongly depend on energy and their central values vary by five orders of magnitude.

One of the purposes of the BABAR ISR program was to measure the total hadronic cross section in the energy range below 2 GeV with improved accuracy (Druzhinin, 2007). To finalize this program, the cross sections at least for the $\pi^+\pi^-3\pi^0$, $\pi^+\pi^-4\pi^0$, K^+K^-, K_SK_L, $K_SK_L\pi\pi$, $K_SK^\pm\pi^\mp\pi^0$ final states should be additionally measured.

Note that the total cross section value is not the direct sum of the cross sections shown in Fig. 64. Each channel has internal subprocesses which include different resonances with different branching fractions to the observed final states. To perform a correct summation, each subchannel should be extracted separately and corrected

TABLE II Summary of the $\omega(1420)(\omega')$ and $\omega(1650)(\omega")$ resonance parameters obtained from the fits described in the text. The values without errors were fixed in the fits.

Fit	$\omega\eta$ (Aubert *et al.*, 2006b)	$\omega\pi^+\pi^-$ (Aubert *et al.*, 2007c)	3π (Aubert *et al.*, 2004b)	PDG (Amsler *et al.*, 2008)
$\sigma_{0w'}$ (nb)	–	1.01±0.29	–	–
$B_{ee}B_{w'f}\cdot 10^6$	–	0.13±0.04	0.82±0.08	–
$\Gamma_{ee}B_{w'f}$(eV)	–	17.5±5.4	369	–
$m_{w'}$(GeV/c^2)	–	1.38±0.02±0.07	1.350±0.030	1.40–1.45
$\Gamma_{w'}$(GeV)	–	0.13±0.05±0.01	0.450±0.140	0.180–0.250
$\phi_{w'}$ (rad.)	–	π	π	–
$\sigma_{0w''}$ (nb)	3.08±0.33	2.47±0.18	–	–
$B_{ee}B_{w''f}\cdot 10^6$	–	0.47±0.04	1.3±0.2	–
$\Gamma_{ee}B_{w''f}$(eV)	–	103.5±8.3	286	–
$m_{w''}$(GeV/c^2)	1.645±0.008	1.667±0.013±0.006	1.660±0.011	1.670±0.030
$\Gamma_{w''}$(GeV)	0.114±0.014	0.222±0.025±0.020	0.220±0.040	0.315±0.035
$\phi_{w''}$ (rad.)	0	0	0	–
σ_{0w} (nb)	0	102±67	PDG	–
χ^2/n.d.f.	–	34.9/48	–	–

for the decay rate of an internal resonance.

The exclusive ISR study of hadron production allows to investigate and improve our knowledge of excited states for light vector mesons. For most of them the parameters are still rather imprecise and new investigations are needed.

For multihadron final states it may be difficult to isolate the contributions of particular vector resonances due to presence of many interfering intermediate states. An example is the reaction $e^+e^-\to\pi^+\pi^-\pi^0\pi^0$, to which the $\omega\pi^0$, $a_1\pi$, $\rho^+\rho^-$ intermediate states give dominant contributions. The two latter states contain wide resonances and strongly interfere. A partial-wave analysis is required to separate the sub-processes of the $e^+e^-\to\pi^+\pi^-\pi^0\pi^0$ and $e^+e^-\to\pi^+\pi^-\pi^+\pi^-$ reactions. We hope that BABAR has enough data to perform such an analysis. This is necessary to separate contributions of two excited ρ states, $\rho(1450)$ and $\rho(1700)$, and determine their parameters. A detailed study of intermediate mechanisms strongly benefits from the quasi-two-body character of some final states, but is much more difficult for multibody final states.

The BABAR ISR data on isoscalar channels already allow to improve parameters of excited ϕ and ω states. A global fit to the isovector and isoscalar components for the process $e^+e^-\to K^*(892)\bar{K}$, and the $e^+e^-\to\phi\eta$ cross section (Buon *et al.*, 1982) was used to determine parameters of the $\phi(1680)$ resonance (see Table I).

In Table II we summarize the results of the fits to the $e^+e^-\to 3\pi$, $e^+e^-\to\omega\pi\pi$, and $e^+e^-\to\omega\eta$ cross sections performed by BABAR in Refs. (Aubert *et al.*, 2004b, 2006b, 2007c), and compare them with the corresponding PDG (Amsler *et al.*, 2008) parameters. A simultaneous fit to all three channels could significantly improve the results and give additional information on relative decay rates.

Due to numerous extensive studies of various exclusive cross sections, we have learned a lot about the total cross section of e^+e^- annihilation into hadrons and its components allowing a more precise estimation of hadronic vacuum polarization effects to be performed (see also Section VII).

IV. BARYON FORM FACTORS

A. General formulae

The cross section of the process $e^+e^-\to\mathcal{B}\bar{\mathcal{B}}$, where $\mathcal{B}$ is a spin-1/2 baryon, is given by (Renard, 1981)

$$\frac{\mathrm{d}\sigma}{\mathrm{d}\Omega} = \frac{\alpha^2\beta C}{4s}\left[(|G_M(s)|^2(1+\cos^2\theta)\right. \quad (11)$$

$$+ \frac{1}{\tau}|G_E(s)|^2\sin^2\theta) \quad (12)$$

$$\left. - \frac{1}{\tau}|G_E(s)|^2)\sin^2\theta\cos 2\varphi\right],$$

where $\beta=\sqrt{1-4m_{\mathcal{B}}^2/s}$ and $m_{\mathcal{B}}$ are the baryon velocity (v/c) and mass, $C=y/(1-e^{-y})$ with $y=\pi\alpha m_{\mathcal{B}}/\beta\sqrt{s}$ is the Coulomb correction factor (Tzara, 1970) for charged baryons ($C=1$ for neutral baryons), $\tau=m^2/4M_{\mathcal{B}}^2$ is the inverse helicity suppression factor, G_M and G_E are the baryon magnetic and electric form factors. The number of form factors (two) corresponds to two $\mathcal{B}\bar{\mathcal{B}}$ states with different angular momenta: $^3S_1$ and $^3D_1$. At the $\mathcal{B}\bar{\mathcal{B}}$ threshold the D-wave state vanishes, and $|G_E|=|G_M|$. At high $\sqrt{s}$ the terms containing G_E are suppressed by the helicity factor $1/\tau$. With unpolarized beams the total cross section is

$$\sigma(s)=\frac{4\pi\alpha^2\beta C}{3s}\left[|G_M(s)|^2+\frac{1}{2\tau}|G_E(s)|^2\right]. \quad (13)$$

As discussed above (see Sections II.A and II.D, and Fig. 7), the detection efficiency in the ISR measurement with a tagged photon has weak dependence on the angular distributions of final hadrons. In the case of the

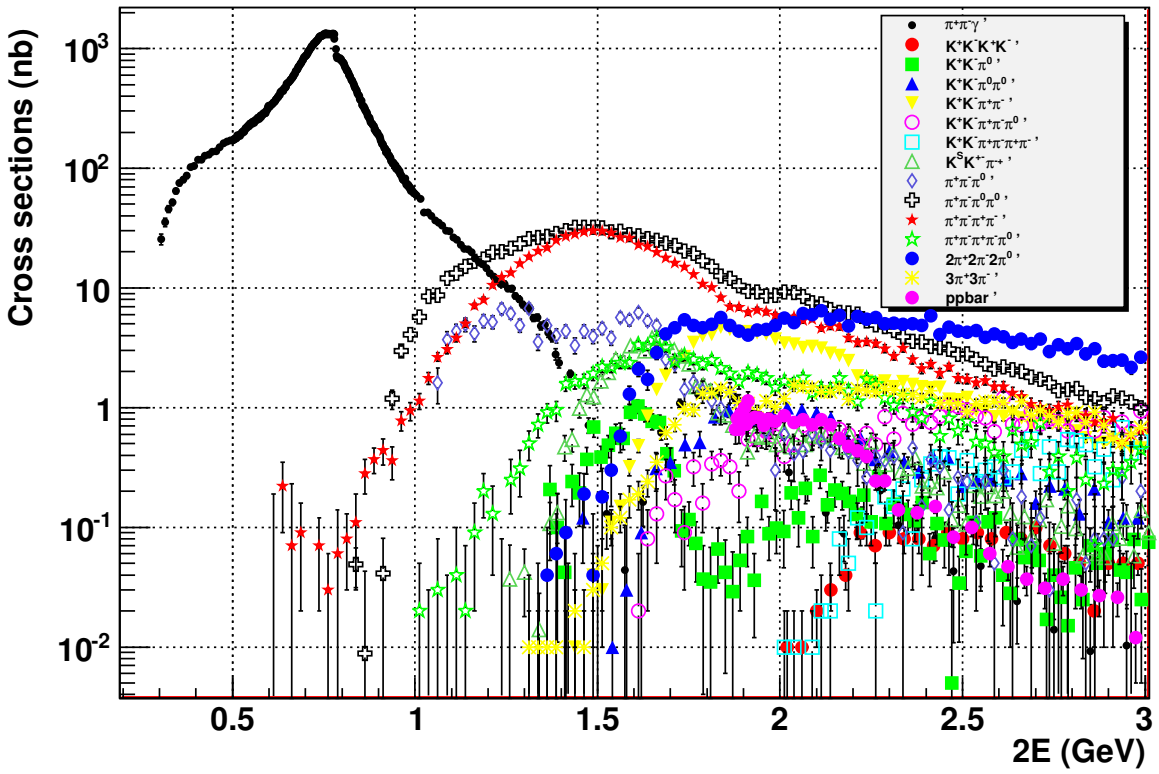


FIG. 64 The cross sections of $e^+e^- \to$ hadrons measured with the BABAR detector via ISR. The results on $e^+e^- \to \pi^+\pi^-\pi^0\pi^0$ are preliminary.

dibaryon production this allows one to measure the total cross section [Eq.(13)] independently of the relation between the electric and magnetic form factors. The ratio of the form factors can then be determined from an analysis of the baryon angular distribution. In direct e^+e^- or $p\bar{p}$ experiments the range of the accessible polar angles is limited by the detector acceptance. In this case the cross section cannot be measured in a model-independent way. The detection efficiency is determined, and the proton magnetic form factor $|G_M|$ is extracted, usually under the assumption that $|G_M| = |G_E|$. In the BABAR paper (Aubert *et al.*, 2006a) on the ISR study of the reaction $e^+e^- \to p\bar{p}$ the effective form factor is introduced as a linear combination of $|G_M|^2$ and $|G_E|^2$:

$$|F(m)|^2 = \frac{2\tau|G_M(s)|^2 + |G_E(s)|^2}{2\tau + 1} \qquad (14)$$

With the effective form factor the total cross section looks like

$$\sigma_0(m) = \frac{4\pi\alpha^2\beta C}{3m^2}(1 + \frac{1}{2\tau})|F(m)|^2 \qquad (15)$$

The effective form factor defined in such a way allows an easy comparison of the results of the model-independent ISR measurement with $|G_M|$ obtained in direct e^+e^- and $p\bar{p}$ experiments under the assumption that $|G_M| = |G_E|$.

The modulus of the ratio of the electric and magnetic form factors can be determined from the analysis of the baryon polar angle distribution. This distribution can be presented as a sum of the terms proportional to $|G_M|^2$ and $|G_E|^2$. For the $e^+e^- \to p\bar{p}\gamma$ cross section the fully differential formula can be found in (Czyż *et al.*, 2004). In this process the θ_p dependences of the G_E and G_M terms are not strongly different from $\sin^2\theta_p$ and $1 + \cos^2\theta_p$, describing the angular distributions for the electric and magnetic form factors in Eq. (12). Note that in direct e^+e^- experiments with transversely polarized beams a study of the proton azimuthal angle distribution can improve G_E/G_M separation (see Eq. (12)).

A nonzero relative phase between the electric and magnetic form factors manifests itself in a polarization of the outgoing baryons. In the reaction $e^+e^- \to \mathcal{B}\bar{\mathcal{B}}$ this polarization is perpendicular to the production plane (Dubnickova *et al.*, 1996). For the ISR process $e^+e^- \to \mathcal{B}\bar{\mathcal{B}}\gamma$ the polarization observables are analyzed in Refs. (Czyż *et al.*, 2007; Kardapoltzev, 2007). In the case of the $\Lambda\bar{\Lambda}$ final state the $\Lambda \to p\pi^-$ decay can be used to measure the Λ polarization and hence the phase between the form factors.

B. Measurement of time-like baryon form factors

Measurements of the $e^+e^- \to p\bar{p}$ cross section have been performed in e^+e^- experiments (Ablikim *et al.*, 2005; Antonelli *et al.*, 1998; Bisello *et al.*, 1983, 1990; Castellano *et al.*, 1973; Delcourt *et al.*, 1979; Pedlar *et al.*, 2005) with a (20–30)% precision. The cross section and the proton form factor were deduced assuming $|G_E| = |G_M|$. More precise measurements of the proton form factor have been performed in $p\bar{p} \to e^+e^-$ experiments (Ambrogiani *et al.*, 1999; Armstrong *et al.*, 1993; Bardin *et al.*, 1994). In the PS170 experiment (Bardin *et al.*, 1994) at LEAR, the proton form factor was measured from threshold ($p\bar{p}$ annihilation at rest) up to a mass of 2.05 GeV/c^2. The ratio $|G_E/G_M|$ was measured using the angular dependence of the cross section and was found to be compatible with unity. The LEAR data show a strong dependence of the form factor on $p\bar{p}$ mass near threshold, and a weak dependence in the range 1.95–2.05 GeV/c^2. The Fermilab experiments, E760 (Armstrong *et al.*, 1993) and E835 (Ambrogiani *et al.*, 1999), show that the form factor decreases rapidly at higher masses, in agreement with the perturbative QCD prediction $G_M \propto \alpha_s^2(m^2)/m^4$.

Experimental information on the reactions $e^+e^- \to \Lambda\bar{\Lambda}$, $\Sigma^0\bar{\Sigma}^0$, $\Lambda\bar{\Sigma}^0$ is very scarce. The $e^+e^- \to \Lambda\bar{\Lambda}$ cross section is measured to be 100^{+65}_{-35} pb at 2.386 GeV, and at the same energy the upper limits for $e^+e^- \to \Sigma^0\bar{\Sigma}^0$ (< 120 pb) and $e^+e^- \to \Lambda\bar{\Sigma}^0$ (< 75 pb) cross sections have been obtained (Bisello *et al.*, 1990).

C. $e^+e^- \to p\bar{p}\gamma$

The first ISR baryon experiment was the measurement of the proton-antiproton production cross section (Aubert *et al.*, 2006a) by BABAR. The measured $e^+e^- \to p\bar{p}$ cross section shown in Figs. 65 and 66 is almost flat near the threshold, and then decreases from 1 nb to about 1 pb at 4.5 GeV. There are two rapid drops of the cross section near 2.15 and 2.9 GeV. The BABAR proton form factor data presented in Fig. 67, in general, agree with the previous measurements. Figure 68 shows an expanded view of the near-threshold region. The BABAR measurement confirms the PS170 observation (Bardin *et al.*, 1994) of the significant increase in the form factor for energies approaching the $p\bar{p}$ threshold. The proton form factor reaches about 0.6 at the threshold.

A study of the proton angular distribution allows one to extract the value of the ratio of the electric and magnetic form factors $|G_E/G_M|$. The results of the BABAR $|G_E/G_M|$ measurement are shown in Fig. 69 in comparison with the data obtained at LEAR (Bardin *et al.*, 1994). In disagreement with the LEAR result, the BABAR data indicate that $|G_E/G_M|$ significantly exceeds unity in the energy range between threshold and 2.1 GeV.

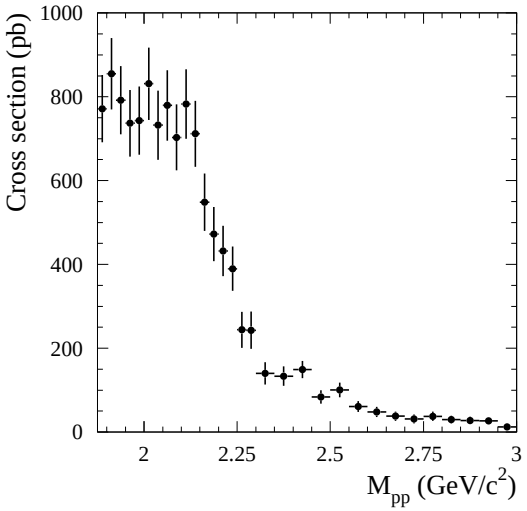


FIG. 65 The $e^+e^- \to p\bar{p}$ cross section measured by BABAR (Aubert *et al.*, 2006a).

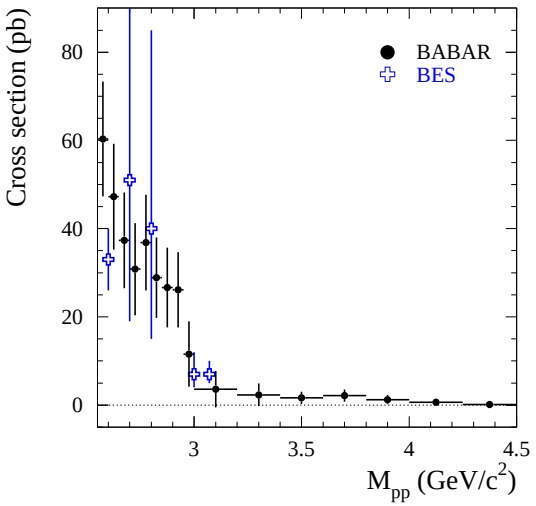


FIG. 66 The $e^+e^- \to p\bar{p}$ cross section measured by BABAR (Aubert *et al.*, 2006a) in comparison with the BES data (Ablikim *et al.*, 2005)

D. $e^+e^- \to \Lambda\bar{\Lambda}\gamma$

The $e^+e^- \to \Lambda\bar{\Lambda}$ cross section measured by the BABAR detector (Aubert *et al.*, 2007d) is shown in Fig.70 in comparison with the only previous measurement (Bisello *et al.*, 1990). The BABAR measurement is based on about 200 $\Lambda\bar{\Lambda}$ events selected in the decay mode $\Lambda \to p\pi$.

The measured Λ effective form factor is shown in Fig.71. The ratio $|G_E/G_M|$ is found to be consistent

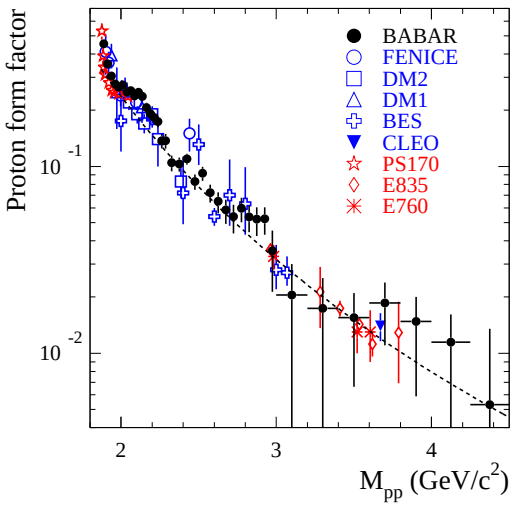


FIG. 67 The proton form factor measured in different experiments (Ablikim *et al.*, 2005; Ambrogiani *et al.*, 1999; Antonelli *et al.*, 1998; Armstrong *et al.*, 1993; Aubert *et al.*, 2006a; Bardin *et al.*, 1994; Bisello *et al.*, 1983; Delcourt *et al.*, 1979; Pedlar *et al.*, 2005). The solid line represents the QCD fit described in the text.

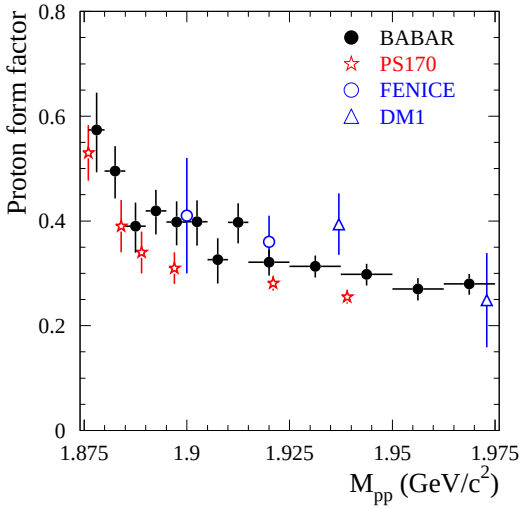


FIG. 68 The proton form factor in the near-threshold region (Antonelli *et al.*, 1998; Aubert *et al.*, 2006a; Bardin *et al.*, 1994; Delcourt *et al.*, 1979).

with unity. The use of the $\Lambda \to p\pi$ decay allows to measure the relative phase ϕ_Λ between the complex G_E and G_M form factors. A non-zero ϕ_Λ leads to polarization ζ of the outgoing baryons. The value of ζ is extracted from the analysis of the proton angular distribution in the $\Lambda \to p\pi$ decay. The measured $\cos\theta_{p\zeta}$ distribution, where $\theta_{p\zeta}$ is the angle between the Λ polarization vector and the proton momentum in the Λ rest frame, is shown in Fig.72. No $\cos\theta_{p\zeta}$ distribution asymmetry corresponding to the non-zero polarization is seen. Because of the

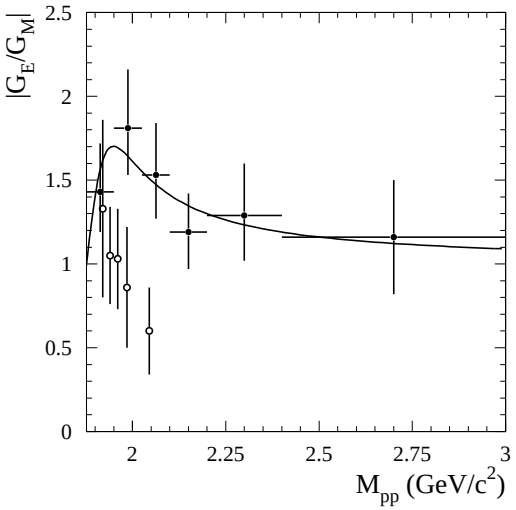


FIG. 69 The proton $|G_E/G_M|$ ratio measured by BABAR (Aubert *et al.*, 2006a) (black points) compared with LEAR data (Bardin *et al.*, 1994) (open circles).

limited data sample only a very weak limit on the phase between the G_E and G_M has been set for the Λ hyperon: $-0.76 < \sin\phi_\Lambda < 0.98$.

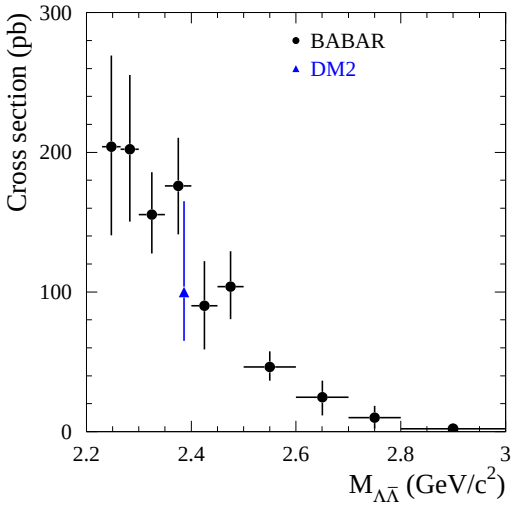


FIG. 70 The $e^+e^- \to \Lambda\bar{\Lambda}$ cross section measured by BABAR (Aubert *et al.*, 2007d) in comparison with the DM2 measurement (Bisello *et al.*, 1990).

E. $e^+e^- \to \Sigma^0\bar{\Sigma}^0$, $\Lambda\bar{\Sigma}^0$ ($\Sigma^0\bar{\Lambda}$)

The BABAR measurement of the Σ^0 and $\Sigma^0\Lambda$ form factors is described in Ref. (Aubert *et al.*, 2007d). The decay chain $\Sigma^0 \to \Lambda\gamma \to p\pi\gamma$ is used to reconstruct Σ^0. About 20 candidate events were selected for each of the ISR reactions, $e^+e^- \to \Sigma^0\bar{\Sigma}^0\gamma$ and $e^+e^- \to \Sigma^0\bar{\Lambda}\gamma$.

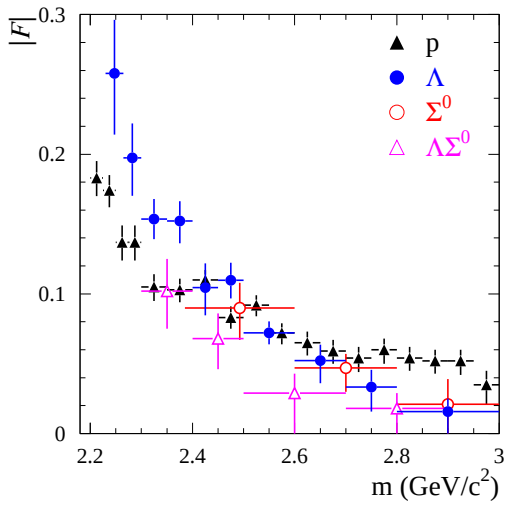


FIG. 71 The baryon form factors measured by BABAR (Aubert *et al.*, 2006a, 2007d) versus the dibaryon invariant mass.

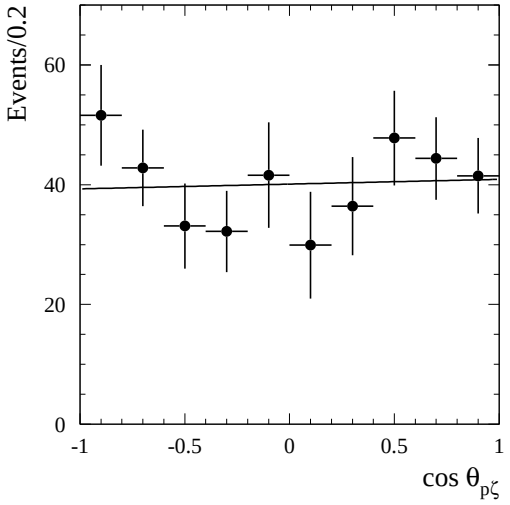


FIG. 72 The $\cos\theta_{p\zeta}$ distribution in the $e^+e^- \to \Lambda\bar{\Lambda}$ process (Aubert *et al.*, 2007d). The line represents the result of the fit to data with a first-order polynomial.

The effective Σ^0 and $\Sigma^0\Lambda$ form factors are shown in Fig.71. The corresponding values of the $e^+e^- \to \Sigma^0\bar{\Sigma}^0$ and $e^+e^- \to \Sigma^0\bar{\Lambda}$ cross sections are about 40 pb near the reaction thresholds. It is seen that the Λ, Σ^0 and $\Sigma^0\Lambda$ form factors are of the same order.

F. Summary

The baryon form factors are a subject of various phenomenological models (see Ref. (Baldini *et al.*, 2009) and references therein). QCD predicts for the baryon form factor the asymptotic behavior $F(q^2) \sim \alpha_s^2(q^2)/q^4$ (Chernyak and Zhitnitsky, 1977). Comparison of this prediction with the data on the proton form factor is shown in Fig. 67. It is seen that the asymptotic regime is reached at energies higher than 3 GeV.

The remarkable feature of the process $e^+e^- \to p\bar{p}$ is a nearly flat cross section in the 200-MeV region above the $p\bar{p}$ threshold. This feature is explained in Ref. (Baldini *et al.*, 2009) by the opposite trends in the energy dependence of the S-wave and D-wave contributions.

A natural explanation for the sharp increase of the proton form factor in the vicinity of the $p\bar{p}$ threshold is the final state interaction of the proton and antiproton (see, for example, Ref. (Dmitriev and Milstein, 2007) and references therein). Another possibility is a contribution of the vector-meson state located just below the $p\bar{p}$ threshold. This state is observed in the reaction $e^+e^- \to 6\pi$ (Aubert *et al.*, 2006b; Baldini *et al.*, 1988; Frabetti *et al.*, 2000).

The rapid drop of the cross section at 2.15 GeV may be a manifestation of the isovector state $\rho(2150)$, which is seen in the reactions $e^+e^- \to \eta'\pi^+\pi^-$ and $e^+e^- \to f_1(1285)\pi^+\pi^-$ (Aubert *et al.*, 2007c). The drop in the cross section near 2.9 GeV is still not understood.

The $e^+e^- \to \Lambda\bar{\Lambda}$ cross section has some features similar to those for the process $e^+e^- \to p\bar{p}$. In the energy region of about 200 MeV above threshold the $\Lambda\bar{\Lambda}$ cross section is flat; the G_E/G_M ratio is consistent with that measured by BABAR for the $e^+e^- \to p\bar{p}$. The attempt to explain the unusual energy dependence of the $e^+e^- \to \Lambda\bar{\Lambda}$ cross section was made in Ref. (Baldini *et al.*, 2009). A fit to the Λ form factor with the power-law function $const/q^n$ (Fig.73) gives $n = 9.2 \pm 0.3$. This n value strongly differs from the QCD asymptotic prediction $n = 4$. Similarly to the $p\bar{p}$ case, the asymptotic regime is not reached for $e^+e^- \to \Lambda\bar{\Lambda}$ at the energies below 3 GeV.

The cross sections of the processes $e^+e^- \to \Sigma^0\bar{\Sigma}^0$ and $e^+e^- \to \Lambda\bar{\Sigma}^0(\Sigma^0\bar{\Lambda})$ have been measured with large errors. The corresponding Σ^0 and $\Sigma^0\Lambda$ form factors (Fig.71) show a monotonic decrease starting just from the threshold. A fit to form factor data with the power-law function gives $n > 4$ but with large errors.

It is interesting to compare the measured form factors with each other and with the QCD prediction for the asymptotic form factor ratios (Chernyak *et al.*, 1989): $F_p = 4.1F_\Lambda$, $F_{\Sigma^0} = -1.18F_\Lambda$, $F_{\Sigma^0\Lambda} = -2.34F_\Lambda$. From comparison of the form factors in Fig.71, it is seen that the prediction works (possibly accidentally) only for the ratio of the Λ and Σ^0 form factors. The ratio F_Λ/F_p falls with energy. In the highest energy interval 2.8–3.00 GeV the ratio is equal to $0.3^{+0.2}_{-0.3}$ and agrees with the asymptotic value 0.24. This is an indication that the asymptotic regime is reached just above 3 GeV.

The BABAR experiment shows that the ISR method is well suited for the measurement of baryon form factors. Future Super B-factories as well as already running BEPC e^+e^- collider will make possible measurements

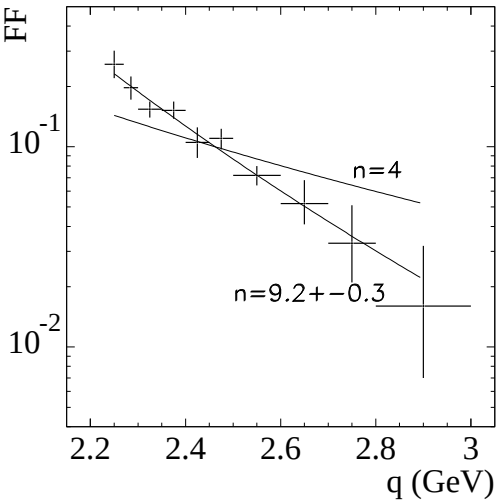


FIG. 73 A fit of the Λ form factor (Aubert *et al.*, 2007d) with the power-law function $F \sim const/q^n$ and with the QCD-inspired function $F \sim const/q^4$.

of the form factors, especially for the proton, with unprecedented accuracy. High-precision measurements of the proton form factor are also planned in the PANDA experiment. .

V. DECAYS OF THE J/ψ AND $\psi(2S)$

For all the processes described in the previous sections, clear narrow peaks are seen in the energy dependence of the cross sections corresponding to the J/ψ and $\psi(2S)$ decays. The Born cross section for the ISR production of a narrow resonance, for example, the J/ψ, decaying to the final state h can be calculated using (Aubert *et al.*, 2004a)

$$\sigma_{J/\psi} = \frac{12\pi^2\Gamma(J/\psi \to e^+e^-)\mathcal{B}(J/\psi \to h)}{s m_{J/\psi}} W_0(\theta_0, x_{J/\psi}) \tag{16}$$

where $m_{J/\psi}$ and $\Gamma(J/\psi \to e^+e^-)$ are the mass and electronic width of the J/ψ meson, $x_{J/\psi} = 1 - m^2_{J/\psi}/s$, and $\mathcal{B}(J/\psi \to h)$ is the branching fraction for the J/ψ decay to the final state h. The function W_0 is described in Sec. I.C by Eq.(7). Therefore, a measurement of the number of $J/\psi \to h$ decays in the ISR process $e^+e^- \to h\gamma$ determines the product of the electronic width and the branching fraction: $\Gamma(J/\psi \to e^+e^-)\mathcal{B}(J/\psi \to h)$.

The total cross section for the process $e^+e^- \to \gamma J/\psi$ with a tagged ISR photon ($\theta_0 = 30^\circ$) is about 3.4 pb. With the integrated luminosity of ~ 500 fb^{-1} collected by the BABAR detector it corresponds to about 1.7 million produced J/ψ's. This number is significantly smaller than, for example, about 60 million J/ψ's produced in the BESII experiment at the BEPC e^+e^- collider. However, the general quality of the BABAR detector and its particle identification in particular, are much better compared to the BESII detector. As a result, the detector efficiency and the integrated luminosity are determined with lower systematic errors. A typical systematic uncertainty of the BABAR measurement is 3-5%, while BESII usually quotes 10-15%. The lower systematic error makes ISR results on many J/ψ decays competitive with BESII and other previous measurements. Practically all decays with the rates about 10^{-3} and higher can be measured via ISR with better overall accuracy. Moreover, because of excellent particle identification, many J/ψ and $\psi(2S)$ decays with kaons in the final state have been studied using ISR for the first time.

In the BABAR experiment the ISR method enabled to measure a few tens of J/ψ and $\psi(2S)$ decays with the best-to-date accuracy and discover about 20 new decays of these resonances.

A. Leptonic decays

The BABAR (Aubert *et al.*, 2004a) and CLEO (Adams *et al.*, 2006) collaborations performed a study of the J/ψ production in the reaction $e^+e^- \to \mu^+\mu^-\gamma$. The dimuon mass spectrum for this reaction obtained by BABAR is shown in Fig. 74. The signal of the ISR J/ψ production is well seen in the mass spectrum. The nonresonant spectrum is due to muon pair production in the process $e^+e^- \to \mu^+\mu^-\gamma$, where photon can be emitted by both initial electrons and final muons. Since the dimuon decay of the J/ψ meson proceeds through a single photon transition, $J/\psi \to \gamma^* \to \mu^+\mu^-$, the angular and momentum distributions for events from the J/ψ peak are completely identical to those for the ISR part of nonresonant events. The idea of the BABAR measurement is to determine the ratio of the number of J/ψ events to the level of the nonresonant spectrum which is well known theoretically. The dimuon spectrum of Fig. 74 has been fit with a function taking into account the energy dependence of the nonresonant cross section and the experimental J/ψ line shape. The ratio

$$r = \frac{N_{J/\psi}}{\frac{\mathrm{d}N}{\mathrm{d}m} \cdot \Delta m} \tag{17}$$

was the main fit parameter. After substituting cross sections for the numbers of events, this ratio can be rewritten

$$r = \frac{\sigma^{\mathrm{Born}}_{J/\psi}}{\frac{\mathrm{d}\sigma^{\mathrm{Born}}_{\mathrm{ISR}}}{\mathrm{d}m} \cdot \Delta m} \cdot \frac{1}{K};\ K = \frac{\mathrm{d}\sigma^{\mathrm{vis}}_{\mathrm{Total}}/\mathrm{d}m}{\mathrm{d}\sigma^{\mathrm{vis}}_{\mathrm{ISR}}/\mathrm{d}m}. \tag{18}$$

Detector acceptances and ISR radiative corrections, which are the same for the nonresonant ISR and J/ψ contributions to the reaction $e^+e^- \to \mu^+\mu^-\gamma$, cancel in the ratio. The total nonresonant cross section includes the FSR contribution, which is parameterized in terms

of K, the ratio of the visible nonresonant total and ISR-only (FSR switched off) cross sections. Since BABAR selects events with the photon emitted at a large angle, the FSR contribution is relatively large. Using simulated events, the coefficient $K = 1.11 \pm 0.01$ (statistical error only) is determined for the selection criteria used.

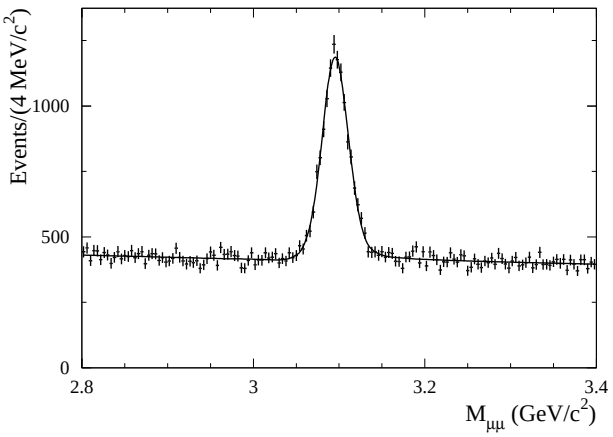


FIG. 74 The $\mu^+\mu^-$ mass spectrum in the J/ψ region for selected events of the reaction $e^+e^- \to \mu^+\mu^-\gamma$ (Aubert *et al.*, 2004a). The curve is the result of the fit described in the text.

The result of the fit is shown in Fig. 74. The value $r = 18.94 \pm 0.44$ is found with $\chi^2/ndf = 122/144$. From the product $r \cdot K = 21.03 \pm 0.49 \pm 0.47$ the cross section $\sigma_{J/\psi} = 2124 \pm 49 \pm 47$ fb and the product of the J/ψ parameters

$$\Gamma_{ee} \cdot B_{\mu\mu} = 0.3301 \pm 0.0077 \pm 0.0073 \text{ keV}$$

are determined. The main sources of the systematic error quoted are uncertainties in the J/ψ line shape and the coefficient K, both due to imperfect simulation of the detector response.

Using the values for B_{ee} and $B_{\mu\mu}$ (Eidelman *et al.*, 2004), which are well measured in the cascade $\psi(2S) \to J/\psi\pi^+\pi^-$ decays (Bai *et al.*, 1998), the electronic and total widths of the J/ψ meson were derived,

$$\Gamma_{ee} = 5.61 \pm 0.20 \text{ keV}, \quad \Gamma = 94.7 \pm 4.4 \text{ keV}\,.$$

These were the best-to-date measurements of the J/ψ parameters.

The BABAR measurement was improved by CLEO. With the integrated luminocity of 281 pb^{-1} collected at $\sqrt{s} = 3.77$ GeV about 13×10^3 ISR produced $J/\psi \to \mu^+\mu^-$ events were selected (compared to 8×10^3 $J/\psi \to \mu^+\mu^-$ events in the BABAR measurement based on a 88 fb^{-1} data sample). Since CLEO used the untagged approach, the FSR contribution to the nonresonant cross section was significantly reduced. The second important improvement of the method was that the J/ψ line shape was extracted from data. To do this, the data collected by CLEO at the $\psi(2S)$ resonance were used to select a clean sample of $\psi(2S) \to J/\psi\pi^+\pi^-$, $J/\psi \to \mu^+\mu^-$ events. The CLEO result for the product of the J/ψ parameters is

$$\Gamma_{ee} \cdot \mathcal{B}_{\mu\mu} = 0.3384 \pm 0.0058 \pm 0.0071 \text{ keV}.$$

Despite the analysis improvements described above, the systematic error of the CLEO result was not reduced compared to the BABAR measurement. However, the sources of the systematic uncertainties are different for the two measurements. So the results can be considered as completely independent.

The data collected at $\sqrt{s} = 3.77$ GeV were used by CLEO to study $\psi(2S)$ ISR production (Adam *et al.*, 2006). ISR $\psi(2S)$ events were selected in the decay modes $\psi(2S) \to \pi^+\pi^- J/\psi$, $\pi^0\pi^0 J/\psi$, and $\eta J/\psi$ with the J/ψ decaying to the lepton pair, e^+e^- or $\mu^+\mu^-$. From the number of the $\psi(2S)$ events the products $\Gamma(\psi(2S) \to e^+e^-)\mathcal{B}(\psi(2S) \to XJ/\psi)$, where $X = \pi^+\pi^-$, $\pi^0\pi^0$, and η, were obtained. Since the branching fractions for these decay modes are known with 1.5–2% accuracy (Amsler *et al.*, 2008), the measurement of the products can by used to improve accuracy of the $\psi(2S)$ electronic width. The CLEO result dominates in the current PDG value $\Gamma(\psi(2S) \to e^+e^-) = 2.36 \pm 0.04$ keV (Amsler *et al.*, 2008).

B. Decays to light mesons and baryons

A systematic study of the J/ψ and $\psi(2S)$ decays to light hadrons was performed in the BABAR experiment (Aubert *et al.*, 2004b, 2005b, 2006a,b, 2007c,d). An example of the J/ψ signal for $J/\psi \to \pi^+\pi^-\pi^0$, one of the most probable J/ψ decay modes, is shown in Fig. 75 (Aubert *et al.*, 2004b). It is seen that the nonresonant background is small. From the number of events at the peak, the product $\Gamma(J/\psi \to e^+e^-)B(J/\psi \to 3\pi) = 0.122 \pm 0.005 \pm 0.008$ keV was determined. Using the J/ψ electronic width value, known from the ISR study of the $J/\psi \to \mu^+\mu^-$ decay, the branching fraction $B(J/\psi \to 3\pi) = (2.18 \pm 0.19)\%$ was calculated, which differed by about 50% from the PDG value, $(1.47 \pm 0.13)\%$, available when the analysis (Aubert *et al.*, 2004b) was carried out. Similar deviation was observed in the BES experiment (Bai *et al.*, 2004) where $B(J/\psi \to 3\pi) = (2.10 \pm 0.11)\%$ was obtained.

Another example of a J/ψ decay mode with a rather high probability, which was studied using ISR, is shown in Fig. 76, where the signals of $J/\psi \to 2(\pi^+\pi^-)\pi^0$ and $\psi(2S) \to 2(\pi^+\pi^-)\pi^0$ are clearly seen (Aubert *et al.*, 2007c). Again, by determining the number of peak events over the nonresonant background and using Eq. (16), the product $\Gamma(J/\psi \to e^+e^-)B(J/\psi \to \pi^+\pi^-\pi^+\pi^-\pi^0) = (3.03 \pm 0.05 \pm 0.18) \times 10^{-4}$ keV was determined. The value of the $J/\psi \to \pi^+\pi^-\pi^+\pi^-\pi^0$ branching fraction obtained from this product, $(5.46 \pm 0.09 \pm 0.34)\%$, differed by about 5σ from the PDG value, $(3.37 \pm 0.26)\%$, available

TABLE III Measurements of the J/ψ and $\psi(2S)$ branching fractions via ISR at BABAR (Aubert *et al.*, 2004b, 2005b, 2006a,b, 2007c,d) compared to the current world-average values (Nakamura *et al.*, 2010).

Measured quantity	Measured value (eV)	J/ψ or $\psi(2S)$ branching fraction (10^{-3}) BABAR	PDG-2010
$\Gamma_{ee}^{J/\psi}\mathcal{B}_{J/\psi\to\pi^+\pi^-\pi^0}$	$122 \pm 5 \pm 8$	$21.8 \pm 1.0 \pm 1.6$	$20.7 \pm 1.2 (S = 1.2)^a$
$\Gamma_{ee}^{J/\psi}\mathcal{B}_{J/\psi\to 2(\pi^+\pi^-)}$	$19.5 \pm 1.4 \pm 1.3$	$3.70 \pm 0.26 \pm 0.37$	3.55 ± 0.23
$\Gamma_{ee}^{J/\psi}\mathcal{B}_{J/\psi\to 2(\pi^+\pi^-)\pi^0}$	$303 \pm 5 \pm 18$	$54.6 \pm 0.9 \pm 3.4$	$41 \pm 5 (S = 2.4)$
$\Gamma_{ee}^{J/\psi}\mathcal{B}_{J/\psi\to 3(\pi^+\pi^-)}$	$23.7 \pm 1.6 \pm 1.4$	$4.40 \pm 0.29 \pm 0.29$	4.3 ± 0.4
$\Gamma_{ee}^{J/\psi}\mathcal{B}_{J/\psi\to 2(\pi^+\pi^-\pi^0)}$	$89 \pm 5 \pm 10$	$16.5 \pm 1.0 \pm 1.8$	16.2 ± 2.1
$\Gamma_{ee}^{J/\psi}\mathcal{B}_{J/\psi\to K^+K^-\pi^+\pi^-}$	$37.9 \pm 0.8 \pm 1.1$	$6.84 \pm 0.15 \pm 0.27$	6.6 ± 0.5
$\Gamma_{ee}^{J/\psi}\mathcal{B}_{J/\psi\to K^+K^-\pi^0\pi^0}$	$11.8 \pm 0.8 \pm 0.9$	$2.12 \pm 0.15 \pm 0.18$	2.45 ± 0.32
$\Gamma_{ee}^{J/\psi}\mathcal{B}_{J/\psi\to K^+K^-K^+K^-}$	$4.00 \pm 0.33 \pm 0.29$	$0.72 \pm 0.06 \pm 0.05$	0.76 ± 0.09
$\Gamma_{ee}^{J/\psi}\mathcal{B}_{J/\psi\to K^+K^-\pi^+\pi^-\pi^0}$	$107 \pm 4 \pm 6$	$19.2 \pm 0.8 \pm 1.5$	$17.9 \pm 2.9 (S = 2.2)$
$\Gamma_{ee}^{J/\psi}\mathcal{B}_{J/\psi\to K^+K^-2(\pi^+\pi^-)}$	$27.5 \pm 2.3 \pm 1.7$	$5.09 \pm 0.42 \pm 0.35$	$4.7 \pm 0.7 (S = 1.3)$
$\Gamma_{ee}^{J/\psi}\mathcal{B}_{J/\psi\to\omega\pi^+\pi^-}\mathcal{B}_{\omega\to 3\pi}$	$47.8 \pm 3.1 \pm 3.2$	$9.7 \pm 0.6 \pm 0.6$	$8.6 \pm 0.7 (S = 1.1)$
$\Gamma_{ee}^{J/\psi}\mathcal{B}_{J/\psi\to\omega\pi^+\pi^-\pi^0}\mathcal{B}_{\omega\to 3\pi}$	$22 \pm 3 \pm 2$	$4.1 \pm 0.6 \pm 0.4$	4.0 ± 0.7
$\Gamma_{ee}^{J/\psi}\mathcal{B}_{J/\psi\to\eta\pi^+\pi^-}\mathcal{B}_{\eta\to 3\pi}$	$0.51 \pm 0.22 \pm 0.03$	$0.40 \pm 0.17 \pm 0.03$	0.40 ± 0.17
$\Gamma_{ee}^{J/\psi}\mathcal{B}_{J/\psi\to 2(\pi^+\pi^-)\eta}\mathcal{B}_{\eta\to\gamma\gamma}$	$5.16 \pm 0.85 \pm 0.39$	$2.35 \pm 0.39 \pm 0.20$	2.29 ± 0.24
$\Gamma_{ee}^{J/\psi}\mathcal{B}_{J/\psi\to\phi\eta}\mathcal{B}_{\phi\to K^+K^-}\mathcal{B}_{\eta\to 3\pi}$	$0.84 \pm 0.37 \pm 0.05$	$1.4 \pm 0.6 \pm 0.1$	$0.75 \pm 0.08 (S = 1.5)$
$\Gamma_{ee}^{J/\psi}\mathcal{B}_{J/\psi\to K^+K^-\eta}\mathcal{B}_{\eta\to 2\gamma}$	$4.8 \pm 0.7 \pm 0.3$	$0.87 \pm 0.13 \pm 0.07$	0.87 ± 0.15
$\Gamma_{ee}^{J/\psi}\mathcal{B}_{J/\psi\to\omega K^+K^-}\mathcal{B}_{\omega\to 3\pi}$	$3.3 \pm 1.3 \pm 0.2$	$1.36 \pm 0.50 \pm 0.10$	1.36 ± 0.51
$\Gamma_{ee}^{J/\psi}\mathcal{B}_{J/\psi\to K^+K^-\pi^+\pi^-\eta}\mathcal{B}_{\eta\to\gamma\gamma}$	$10.2 \pm 1.3 \pm 0.8$	$4.7 \pm 0.6 \pm 0.4$	4.67 ± 0.70
$\Gamma_{ee}^{J/\psi}\mathcal{B}_{J/\psi\to(K^{*0}\bar{K}_2^{*0}+\text{c.c.})}\mathcal{B}_{K^{*0}\to K\pi}\mathcal{B}_{K_2^{*0}\to K\pi}$	$8.59 \pm 0.36 \pm 0.27$	$6.98 \pm 0.29 \pm 0.21$	6.0 ± 0.6
$\Gamma_{ee}^{J/\psi}\mathcal{B}_{J/\psi\to(K^0\bar{K}^*(892)^0+\text{c.c.})}$	$26.6 \pm 2.5 \pm 1.5$	$4.8 \pm 0.5 \pm 0.3$	4.39 ± 0.31
$\Gamma_{ee}^{J/\psi}\mathcal{B}_{J/\psi\to(K^+\bar{K}^*(892)^-+\text{c.c.})}$	$29.0 \pm 1.7 \pm 1.3$	$5.2 \pm 0.3 \pm 0.2$	5.12 ± 0.30
$\Gamma_{ee}^{J/\psi}\mathcal{B}_{J/\psi\to K^{*0}\bar{K}^{*0}}\mathcal{B}_{K^{*0}\to K^+\pi^-}\mathcal{B}_{\bar{K}^{*0}\to K^-\pi^+}$	$0.57 \pm 0.15 \pm 0.03$	$0.23 \pm 0.06 \pm 0.01$	0.23 ± 0.07
$\Gamma_{ee}^{J/\psi}\mathcal{B}_{J/\psi\to\phi\pi^+\pi^-}\mathcal{B}_{\phi\to K^+K^-}$	$2.19 \pm 0.23 \pm 0.07$	$0.81 \pm 0.08 \pm 0.03$	$0.94 \pm 0.09 (S = 1.2)$
$\Gamma_{ee}^{J/\psi}\mathcal{B}_{J/\psi\to\phi\pi^0\pi^0}\mathcal{B}_{\phi\to K^+K^-}$	$1.36 \pm 0.27 \pm 0.07$	$0.50 \pm 0.10 \pm 0.03$	0.56 ± 0.16
$\Gamma_{ee}^{J/\psi}\mathcal{B}_{J/\psi\to\phi K^+K^-}\mathcal{B}_{\phi\to K^+K^-}$	$2.26 \pm 0.26 \pm 0.16$	$1.67 \pm 0.19 \pm 0.12^b$	1.83 ± 0.24
$\Gamma_{ee}^{J/\psi}\mathcal{B}_{J/\psi\to\phi f_0}\mathcal{B}_{\phi\to K^+K^-}\mathcal{B}_{f_0\to\pi^+\pi^-}$	$0.69 \pm 0.11 \pm 0.05$	$0.38 \pm 0.06 \pm 0.02$	$0.32 \pm 0.09 (S = 1.9)$
$\Gamma_{ee}^{J/\psi}\mathcal{B}_{J/\psi\to\phi f_0}\mathcal{B}_{\phi\to K^+K^-}\mathcal{B}_{f_0\to\pi^0\pi^0}$	$0.48 \pm 0.12 \pm 0.05$	$0.53 \pm 0.13 \pm 0.05$	$0.32 \pm 0.09 (S = 1.9)$
$\Gamma_{ee}^{J/\psi}\mathcal{B}_{J/\psi\to\phi 2(\pi^+\pi^-)}\mathcal{B}_{\phi\to K^+K^-}$	$4.7 \pm 0.9 \pm 0.9$	$1.77 \pm 0.35 \pm 0.12$	1.66 ± 0.23
$\Gamma_{ee}^{\psi(2S)}\mathcal{B}_{\psi(2S)\to 2(\pi^+\pi^-)\pi^0}$	$29.7 \pm 2.2 \pm 1.8$	$12.0 \pm 0.9 \pm 0.7$	$2.9 \pm 1.0 (S = 4.6)$
$\Gamma_{ee}^{\psi(2S)}\mathcal{B}_{\psi(2S)\to 2(\pi^+\pi^-\pi^0)}$	$11.2 \pm 3.3 \pm 1.3$	$5.3 \pm 1.6 \pm 0.6$	5.3 ± 1.7
$\Gamma_{ee}^{\psi(2S)}\mathcal{B}_{\psi(2S)\to K^+K^-2(\pi^+\pi^-)}$	$4.4 \pm 2.1 \pm 0.3$	$2.1 \pm 1.0 \pm 0.2$	1.9 ± 0.9
$\Gamma_{ee}^{\psi(2S)}\mathcal{B}_{\psi(2S)\to J/\psi\pi^+\pi^-}\mathcal{B}_{J/\psi\to 3\pi}$	$18.6 \pm 1.2 \pm 1.1$	$23.6 \pm 1.6 \pm 1.6$	$20.7 \pm 1.2 (S = 1.2)^c$
$\Gamma_{ee}^{\psi(2S)}\mathcal{B}_{\psi(2S)\to\omega\pi^+\pi^-}\mathcal{B}_{\omega\to 3\pi}$	$2.69 \pm 0.73 \pm 0.16$	$1.22 \pm 0.33 \pm 0.07$	0.73 ± 0.12
$\Gamma_{ee}^{\psi(2S)}\mathcal{B}_{\psi(2S)\to J/\psi\eta}\mathcal{B}_{\eta\to 3\pi}\mathcal{B}_{J/\psi\to\mu^+\mu^-}$	$1.11 \pm 0.33 \pm 0.07$	$33.4 \pm 9.9 \pm 2.0$	32.8 ± 0.7
$\Gamma_{ee}^{\psi(2S)}\mathcal{B}_{\psi(2S)\to 2(\pi^+\pi^-)\eta}\mathcal{B}_{\eta\to\gamma\gamma}$	$1.13 \pm 0.55 \pm 0.08$	$1.2 \pm 0.6 \pm 0.1$	1.2 ± 0.6
$\Gamma_{ee}^{\psi(2S)}\mathcal{B}_{\psi(2S)\to K^+K^-\pi^+\pi^-\pi^0}$	$4.4 \pm 1.3 \pm 0.3$	$1.8 \pm 0.5 \pm 0.1$	$1.26 \pm 0.09 (S = 1.2)$
$\Gamma_{ee}^{\psi(2S)}\mathcal{B}_{\psi(2S)\to K^+K^-\pi^+\pi^-\eta}\mathcal{B}_{\eta\to\gamma\gamma}$	$1.2 \pm 0.7 \pm 0.1$	$1.3 \pm 0.7 \pm 0.1$	1.3 ± 0.7
$\Gamma_{ee}^{\psi(2S)}\mathcal{B}_{\psi(2S)\to K^+K^-\pi^+\pi^-}$	$1.92 \pm 0.30 \pm 0.06$	$0.81 \pm 0.13 \pm 0.03$	$0.75 \pm 0.09 (S = 1.9)$
$\Gamma_{ee}^{\psi(2S)}\mathcal{B}_{\psi(2S)\to K^+K^-\pi^0\pi^0}$	$0.60 \pm 0.31 \pm 0.03$	$0.25 \pm 0.13 \pm 0.02$	0.25 ± 0.13
$\Gamma_{ee}^{\psi(2S)}\mathcal{B}_{\psi(2S)\to K^+K^-K^+K^-}$	$0.22 \pm 0.10 \pm 0.02$	$0.09 \pm 0.04 \pm 0.01$	0.060 ± 0.014
$\Gamma_{ee}^{\psi(2S)}\mathcal{B}_{\psi(2S)\to\phi\pi^+\pi^-}\mathcal{B}_{\phi\to K^+K^-}$	$0.27 \pm 0.09 \pm 0.02$	$0.35 \pm 0.12 \pm 0.01$	$0.117 \pm 0.029 (S = 1.7)$
$\Gamma_{ee}^{\psi(2S)}\mathcal{B}_{\psi(2S)\to\phi f_0}\mathcal{B}_{\phi\to K^+K^-}\mathcal{B}_{f_0\to\pi^+\pi^-}$	$0.17 \pm 0.06 \pm 0.02$	$0.22 \pm 0.08 \pm 0.02$	$0.068 \pm 0.024 (S = 1.1)$

[a] S is a PDG scale factor.
[b] $\mathcal{B}_{J/\psi\to\phi K\bar{K}}$
[c] $\mathcal{B}_{J/\psi\to 3\pi}$.

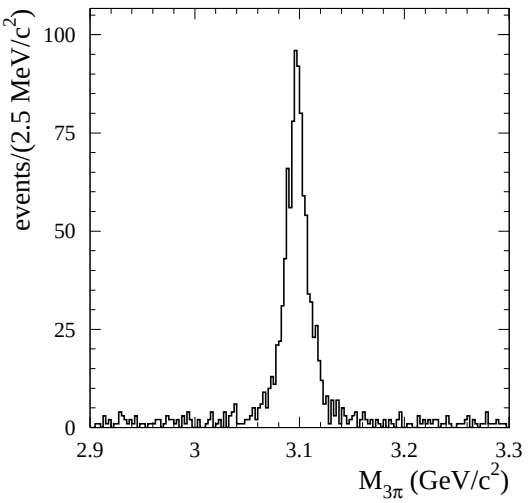


FIG. 75 The 3π mass spectrum for selected $e^+e^- \to \pi^+\pi^-\pi^0\gamma$ data events in the vicinity of the J/ψ resonance (Aubert *et al.*, 2004b).

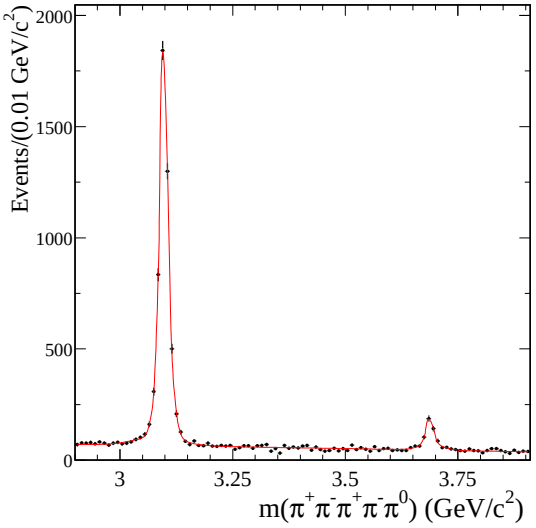


FIG. 76 The $2(\pi^+\pi^-)\pi^0$ mass distribution for ISR $e^+e^- \to 2(\pi^+\pi^-)\pi^0\gamma$ events in the J/ψ–$\psi(2S)$ mass region (Aubert *et al.*, 2007c).

when the analysis (Aubert *et al.*, 2007c) was carried out. As was shown in Sec. III.H, the five-pion final state includes production of many intermediate resonances. All of them are seen in the $J/\psi \to 5\pi$ decay. This may be a source of the systematic error unaccounted in previous measurements of the decay. The detection efficiency in the ISR method with a tagged photon is weakly sensitive to the dynamics of the $J/\psi \to 5\pi$ decay. The model uncertainty in the detection efficiency for the BABAR measurement (Aubert *et al.*, 2007c) was estimeted from the difference in efficiency values for phase-space generated five-pion events and events generated for the $\omega\pi^+\pi^-$ or $\eta\pi^+\pi^-$ final states. It was found to be less than 3%.

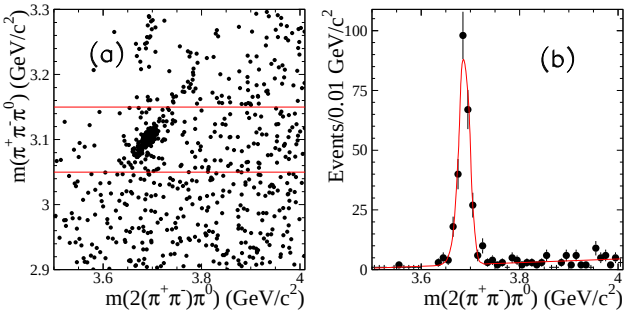


FIG. 77 (a) The three-pion combination closest to J/ψ mass versus five-pion mass. (b) The five-pion mass for events with the three-pion mass in the ± 50 MeV window around J/ψ mass (Aubert *et al.*, 2007c).

A part of events from the $\psi(2S)$ peak comes from the decay chain $\psi(2S) \to J/\psi\pi^+\pi^- \to 2(\pi^+\pi^-)\pi^0$ with the J/ψ decaying to three pions. To select these events, the $\pi^+\pi^-\pi^0$ combination with the invariant mass closest to the J/ψ mass is chosen. Figure 77(a) shows the scatter plot of this three-pion mass versus the five-pion mass. A clear signal from the above decay chain is seen. The five-pion mass spectrum for events with the $\pi^+\pi^-\pi^0$ mass within the ± 0.05 GeV/c^2 window around the J/ψ mass is shown in Fig. 77(b). From the fit to the mass spectrum with a double-Gaussian function the number of detected $\psi(2S) \to J/\psi\pi^+\pi^- \to 2(\pi^+\pi^-)\pi^0$ events was determined to be 256 ± 17, and the triple product

$$\mathcal{B}(\psi(2S) \to J/\psi\pi^+\pi^-)\mathcal{B}(J/\psi \to \pi^+\pi^-\pi^0) \times\Gamma(\psi(2S) \to e^+e^-) = (1.86 \pm 0.12 \pm 0.11) \times 10^{-2} \text{ keV}$$

was obtained. By using the world-average $\Gamma(\psi(2S) \to e^+e^-)$ and $\mathcal{B}(\psi(2S) \to J/\psi\pi^+\pi^-)$ values (Amsler *et al.*, 2008), the branching fraction $\mathcal{B}(J/\psi \to \pi^+\pi^-\pi^0) = (2.36\pm0.16\pm0.16)\%$ was obtained, which is in good agreement with the BABAR measurement in the 3π final state: $\mathcal{B}(J/\psi \to \pi^+\pi^-\pi^0) = (2.18 \pm 0.19)\%$ (Aubert *et al.*, 2004b). This, in particular, confirms the correctness of the normalization procedure used for the measurement of $\mathcal{B}(J/\psi \to 5\pi)$.

Table III presents measurements of the J/ψ and $\psi(2S)$ decay rates performed with the BABAR detector via ISR for many multihadron final states. The current PDG values are shown in the last column (Nakamura *et al.*, 2010). In most of the cases these values are close to those of BABAR emphasizing their importance. Note also that in a few cases the scale factor is significantly higher than one indicating a large difference between the BABAR measurement and previous results.

As can be seen from Table III, the J/ψ decay rates to even numbers of pions $(4\pi, 6\pi \ldots)$ are much smaller compared to the decays to odd numbers of pions. Indeed, a strong decay of the J/ψ to an even number of pions is forbidden by G-parity conservation. It is expected that this decay is dominated by a single photon transition,

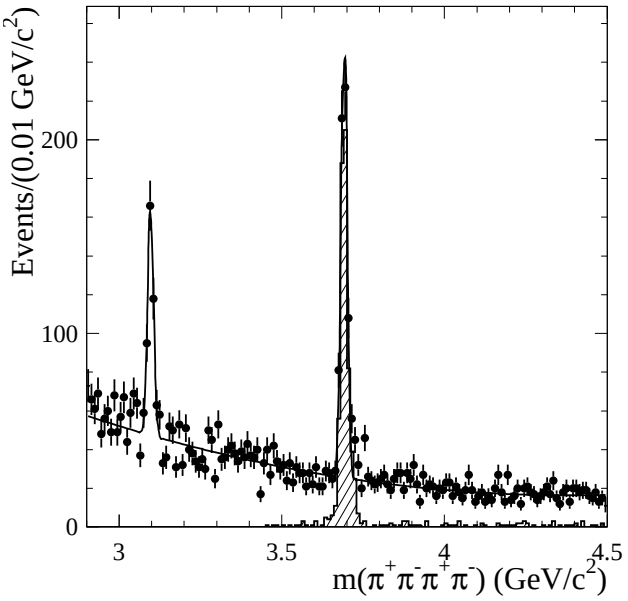


FIG. 78 The $2(\pi^+\pi^-)$ mass distribution for ISR-produced $e^+e^- \to 2(\pi^+\pi^-)$ events in the mass region around the J/ψ and $\psi(2S)$ (Aubert *et al.*, 2005b); there are clear signals at the J/ψ and $\psi(2S)$ mass positions. The latter is dominatesby the $\psi(2S) \to J/\psi\pi^+\pi^- \to \mu^+\mu^-\pi^+\pi^-$ transition; selected events with two muons from the J/ψ decays are shown by the shaded histogram.

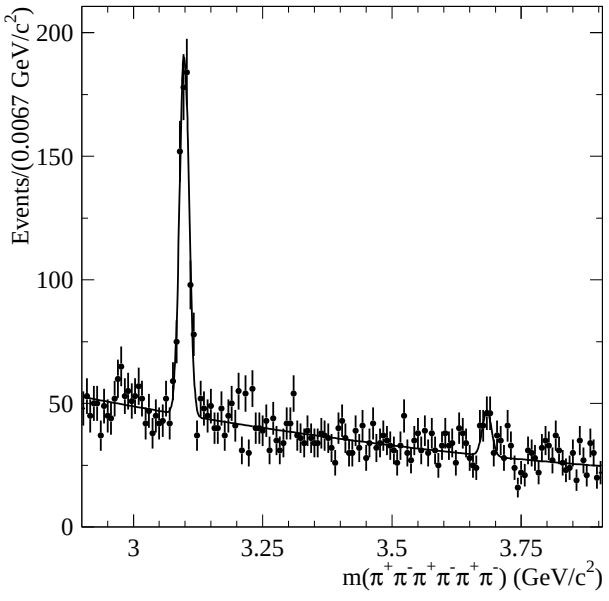


FIG. 79 The $3(\pi^+\pi^-)$ mass distribution for ISR-produced $e^+e^- \to 3(\pi^+\pi^-)$ events in the mass region around the J/ψ and $\psi(2S)$ (Aubert *et al.*, 2006b); there are clear signals at the J/ψ and $\psi(2S)$ mass positions.

$J/\psi \to \gamma^* \to n\pi$. No such suppression occurs for the strong J/ψ decays to other modes, such as to three or five pions, which mainly proceed through three gluons. The $2(\pi^+\pi^-)$ and $3(\pi^+\pi^-)$ mass spectra for events of the ISR processes $e^+e^- \to 2(\pi^+\pi^-)\gamma$ and $e^+e^- \to 3(\pi^+\pi^-)\gamma$, in the mass regions of the J/ψ and $\psi(2S)$ resonances, are shown in Figs. 78 and 79, respectively. From the fits to the mass spectra the numbers of J/ψ and $\psi(2S)$ events and also the level of the nonresonant background are determined. The latter is proportional to the value of the nonresonant $e^+e^- \to 2(\pi^+\pi^-)$ or $e^+e^- \to 3(\pi^+\pi^-)$ cross section. In the BABAR paper (Aubert *et al.*, 2006b) the ratio

$$R_{J/\psi} = \frac{6\pi^2\Gamma(J/\psi \to e^+e^-)\mathcal{B}(J/\psi \to f)/m^2_{J/\psi}}{\sigma_{e^+e^-\to f}(m_{J/\psi})} \quad (19)$$

is calculated, where $\sigma_{e^+e^-\to f}$ is the value of the nonresonant cross section to the final state f at the J/ψ mass. The numerator of the ratio represents the integral over the J/ψ excitation curve. The $R_{J/\psi}$ values for the 4π, 6π, $2K2\pi$, $2K4\pi$, and $4K$ final states are listed in Table IV together with the $R_{J/\psi}$ value obtained for the $\mu^+\mu^-$ final state. The $R_{J/\psi}$ values for the 4π and 6π final states are closer to that for $\mu^+\mu^-$ compared to the final states with kaons and indicate that the single-photon exchange dominates for the J/ψ decays into these modes. For the J/ψ decays to the final states with kaons, which can contain a sizeable isoscalar component, the single-photon transition is expected to be less dominant, as indicated by the larger central values of the ratios.

TABLE IV Ratios of the J/ψ partial production rates to continuum cross sections $R_{J/\psi}$ (see Eq.(19)). The result for $\mu^+\mu^-$ is from Ref. (Aubert *et al.*, 2004a). The result for $3(\pi^+\pi^-)$ is from Ref. (Aubert *et al.*, 2006b) and the results for $2(\pi^+\pi^-)$, $K^+K^-\pi^+\pi^-$ and $K^+K^-K^+K^-$ are from Ref. (Aubert *et al.*, 2005b).

Final state	$R_{J/\psi}$ (MeV)
$2(\pi^+\pi^-)$	85.1 ± 7.9
$3(\pi^+\pi^-)$	106 ± 10
$2(\pi^+\pi^-\pi^0)$	99.1 ± 6.5
$K^+K^-2(\pi^+\pi^-)$	122 ± 10
$K^+K^-\pi^+\pi^-$	166 ± 19
$K^+K^-K^+K^-$	138 ± 32
$\mu^+\mu^-$	84.12 ± 2.69

VI. ISR STUDIES IN THE CHARMONIUM REGION

In this chapter we will discuss recent progress in the charmonium spectroscopy mainly achieved due to the application of the ISR method, see also recent reviews (Brambilla *et al.*, 2011; Pakhlova *et al.*, 2010). We will start with the description of the open charm final states addressing later so-called charmonium-like states, presumably states with hidden charm.

A. Final states with open charm

For a quarter of a century our knowledge of the vector charmonia above the threshold of open charm production (throughout this section referred to as ψ states) was based on the pioneer experiments of Mark-I (Siegrist *et al.*, 1976) and DASP (Brandelik *et al.*, 1978). Even such basic parameters of the ψ mesons as mass, width and leptonic width were known with large uncertainties mainly determined by low statistics of the old experiments. In Ref. (Seth, 2005) an attempt was made to use the updated information on the R values from Crystal Ball (Osterheld *et al.*, 1986) and BES (Bai *et al.*, 2002) to improve these parameters. Finally, the BES Collaboration performed a global fit of the data on R collected by BES in the energy range from 3.7 to 5 GeV (Ablikim *et al.*, 2008). In some cases the obtained values of mass, width and leptonic width for the ψ states differ significantly from the older values and still suffer from big uncertainties caused by insufficient statistics and model dependence primarily due to numerous thresholds of charm production opening in this energy region. It became clear that serious progress would be possible after tedious exclusive studies, which recently became possible due to ISR analyses of BABAR and Belle based on very large integrated luminosities.

Exclusive e^+e^- cross sections for hadronic final states containing charm mesons in the $\sqrt{s}$=3.7-5 GeV/c^2 energy range were measured by BABAR (Aubert *et al.*, 2007e, 2009b) and Belle (Pakhlova *et al.*, 2007, 2008a,b,c, 2009) using ISR to reach the charmonium region. Note that in these analyses Belle systematically employs a partial reconstruction technique to increase the detection efficiency and suppress background.

The $D\bar{D}$ cross sections in the entire charm energy range from Belle (Pakhlova *et al.*, 2008a) and BABAR (Aubert *et al.*, 2007e) are shown in Figs. 80(a),(b) and are consistent with each other. Both exhibit clear evidence of structures near 4.1 and 4.4 GeV/c^2. They also observe a structure (Figs. 80(a) and (b)) at 3900 MeV which must be taken into account to describe the $D\bar{D}$ cross section and R in the region between the $\psi(3770)$ and $\psi(4040)$. This enhancement is not considered as a new $c\bar{c}$ resonance, as it is qualitatively consistent with the energy dependence of the sum of the cross sections for various channels opening in this energy range predicted in a coupled-channel model (Eichten *et al.*, 1980). The $D\bar{D}^*$ cross sections from Belle (Pakhlova *et al.*, 2007) and BABAR (Aubert *et al.*, 2009b) shown in Figs. 80(c),(d) exhibit a single broad peak near threshold (close to the $\psi(4040)$ position), whereas the $D^*\bar{D}^*$ results from Belle (Pakhlova *et al.*, 2007) and BABAR (Aubert *et al.*, 2009b) (Figs. 80(e),(f)) feature several local maxima and minima in this energy range.

BABAR (Aubert *et al.*, 2009b) performed unbinned maximum likelihood fits to the $D\bar{D}$, $D\bar{D}^*$, and $D^*\bar{D}^*$ spectra. The expected ψ signals were parameterized by p-wave relativistic Breit-Wigner (RBW) functions with their parameters fixed to the PDG08 values (Amsler *et al.*, 2008). An interference between the resonances and the non-resonant contributions was required in the fit. The computed ratios of the branching fractions for the ψ resonances and the quark model predictions are presented in Table V. The BABAR results deviate from some of the theoretical expectations, which often differ from each other.

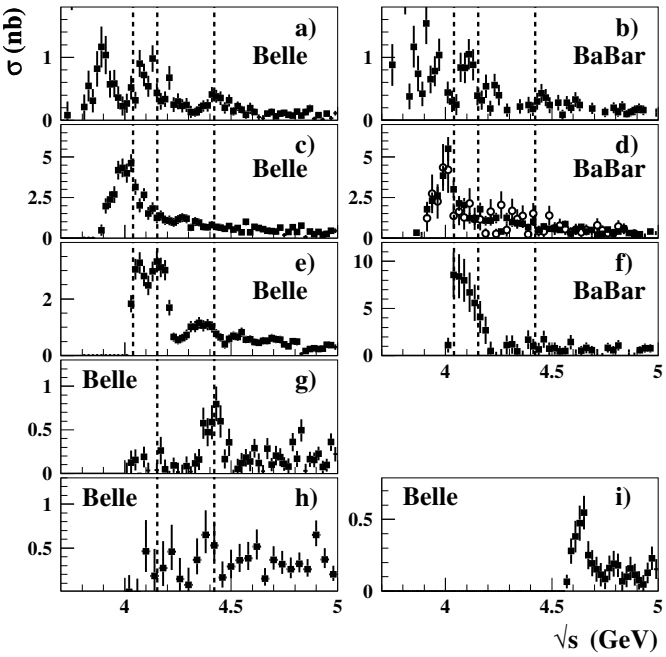


FIG. 80 Measured e^+e^- exclusive open-charm cross sections for $\sqrt{s}$=3.7-5.0 GeV/c^2 from Belle and BABAR, showing (a) $D\bar{D}$ (Pakhlova *et al.*, 2008a), (b) $D\bar{D}$ (Aubert *et al.*, 2007e) , (c) D^+D^{*-} (Pakhlova *et al.*, 2007); (d) $D\bar{D}^*$ for D=D^0 (solid squares) and D=$D^\pm$ (open circles) (Aubert *et al.*, 2009b); (e) $D^{*+}D^{*-}$ (Pakhlova *et al.*, 2007); (f) $D^*\bar{D}^*$ (Aubert *et al.*, 2009b); (g) $D^0D^-\pi^+$ (Pakhlova *et al.*, 2008b); (h) $D^0D^{*-}\pi^+$ (Pakhlova *et al.*, 2009); (i) $\Lambda_c\bar{\Lambda}_c$ (Pakhlova *et al.*, 2008c). Vertical dashed lines indicate ψ masses in the region.

The $e^+e^- \to D^0D^-\pi^+$ cross section measured by Belle (Pakhlova *et al.*, 2008b) is shown in Fig. 80(g) and exhibits an unambiguous $\psi(4415)$ signal. A study of the resonant structure shows clear signals for the $\bar{D}_2^*(2460)^0$ and $D_2^*(2460)^+$ mesons and constructive interference between the neutral $D^0\bar{D}_2^*(2460)^0$ and the charged $D^-D_2^*(2460)^+$ decay amplitudes. Belle performed a likelihood fit to the $D^0D^-\pi^+$ mass distribution with a $\psi(4415)$ signal parameterized by an S-wave RBW function. The significance for the signal is $\sim 10\sigma$ and the peak mass and total width are in good agreement with the PDG06 (Yao *et al.*, 2006) values and the BES fit results (Ablikim *et al.*, 2008). The product of the branching fractions $\mathcal{B}(\psi(4415) \to D\bar{D}_2^*(2460)) \times \mathcal{B}(\bar{D}_2^*(2460) \to D\pi^+)$ was found to be between 10% and 20% depend-

TABLE V Ratios of branching fractions for the $\psi(4040)$, $\psi(4160)$ and $\psi(4415)$ resonances from BABAR (Aubert *et al.*, 2009b). Theoretical expectations are from models denoted $^3P_0$ (Barnes *et al.*, 2005), C^3 (Eichten *et al.*, 2006), and $\rho K \rho$ (Swanson *et al.*, 2006).

State	Ratio	Measured	$^3P_0$	C^3	$\rho K \rho$
$\psi(4040)$	$D\bar{D}/D\bar{D}^*$	0.24±0.05±0.12	0.003		0.14
	$D^*\bar{D}^*/D\bar{D}^*$	0.18±0.14±0.03	1.0		0.29
$\psi(4160)$	$D\bar{D}/D^*\bar{D}^*$	0.02±0.03±0.02	0.46	0.08	
	$D\bar{D}^*/D^*\bar{D}^*$	0.34±0.14±0.05	0.011	0.16	
$\psi(4415)$	$D\bar{D}/D^*\bar{D}^*$	0.14±0.12±0.03	0.025		
	$D\bar{D}^*/D^*\bar{D}^*$	0.17±0.25±0.03	0.14		

ing on the $\psi(4415)$ parameterization. The non-resonant $D^0D^-\pi^+$ branching fraction was found to be <22% of $\mathcal{B}(\psi(4415) \to D\bar{D}_2^*(2460) \to D^0D^-\pi^+)$. Similarly, the energy dependence of the cross section of the $D^0D^{*-}\pi^+$ final state, shown in Fig. 80(h), has been measured by Belle (Pakhlova *et al.*, 2009); a marginal signal of the $\psi(4415)$ is found (3.1σ), and its branching fraction was limited to <10.6%. Very recently BABAR (del Amo Sanchez *et al.*, 2010) and Belle (Pakhlova *et al.*, 2011) reported consistent results on the cross sections of $D_s^+D_s^-$, $D_s^+D_s^{*+}$ and $D_s^{*+}D_s^{*-}$.

The Belle collaboration has also measured the cross section of the process $e^+e^- \to \Lambda_c^+\Lambda_c^-$ (Pakhlova *et al.*, 2008c). Because of the large number of the Λ_c decay channels with small branching fractions full reconstruction of both Λ_c is not effective. The strategy of a search for $\Lambda_c^+\Lambda_c^-\gamma$ events at Belle (Pakhlova *et al.*, 2008c) was the following: one of the Λ_c baryons was reconstructed using three decay modes pK_S^0, $pK^-\pi^+$, $\Lambda\pi^+$. Then in the spectrum of masses recoiling against the $\Lambda_c^+\gamma$ system, a peak at the Λ_c^- mass was searched for. This peak presumably corresponded to the process $e^+e^- \to \Lambda_c^+\Lambda_c^-\gamma$. The resulting exclusive cross section of the process $e^+e^- \to \Lambda_c^+\Lambda_c^-$ is shown in Fig.80(i). The cross section is nearly flat from the threshold up to 5.4 GeV/c^2 except the region just above threshold, where a peak with the mass $M = 4634^{+10}_{-30}$ MeV/c^2, width $\Gamma = 92^{+40}_{-27}$ MeV/c^2 and significance of 8.2 σ is observed. The state is denoted as $X(4630)$ and the product of the branching fractions measured for it is $\mathcal{B}(e^+e^-)\times\mathcal{B}(\Lambda_c\bar{\Lambda}_c) = (0.68\pm0.33)\times10^{-6}$. The nature of this enhancement remains unclear. Although both mass and width of the $X(4630)$ are consistent within errors with those of another Belle state $Y(4660)$, that was found in $\psi(2S)\pi\pi$ decays via ISR and is described in the next section (Wang *et al.*, 2007), this could be coincidence and does not exclude other interpretations.

Although in general the energy behavior of the exclusive cross sections from BABAR and Belle qualitatively follows the expectations of the coupled-channel model (Eichten *et al.*, 1980), some features are not reproduced by theory. This is confirmed by the measurement of CLEO (Cronin-Hennessy *et al.*, 2009), which scanned the energy range between 3.97 and 4.26 GeV and reported the cross sections for final states consisting of two charm mesons ($D\bar{D}$, $D^*\bar{D}$, $D^*\bar{D}^*$, $D_s^+D_s^-$, $D_s^{*+}D_s^-$, and $D_s^{*+}D_s^{*-}$) as well as for those in which the charm-meson pair is accompanied with a pion. The updated potential model predictions of Eichten (Eichten *et al.*, 1980, 2006) fail to describe many features of the data.

B. New charmonium-like states

The first observation of an unexpected vector charmonium-like state was made by BABAR (Aubert *et al.*, 2005a) in ISR production of $Y(4260) \to J/\psi\pi^+\pi^-$, which was later updated (Aubert *et al.*, 2008a) with twice the data, as shown in Fig. 81. CLEO (He *et al.*, 2006) and Belle (Yuan *et al.*, 2007) confirmed the BABAR result, but Belle also found a smaller, broader structure at 4008 MeV/c^2, as seen in Fig. 82. Aside from the lower mass state, for which the updated BABAR (Aubert *et al.*, 2008a) analysis placed an upper limit, the three sets of measurements were quite consistent in mass and width, as shown in Table VI, but only roughly so in strength. BABAR (Aubert *et al.*, 2007a) found one more apparent enhancement $Y(4360)$ in $\psi(2S)\pi^+\pi^-$, which Belle (Wang *et al.*, 2007) measured with somewhat larger mass and smaller width, as seen in Table VII. Belle also found a second structure near 4660 MeV/c^2 in the same final state, as seen in Fig. 83. (A combined fit (Liu *et al.*, 2008) to Belle and BABAR $\psi(2S)\pi^+\pi^-$ data found consistency between them.) Because dipion transitions between vector quarkonia are commonplace for charmonium and bottomonium, it was natural to ascribe the Y's to excited vector charmonia. A number of additional features of these states are in conflict with this hypothesis. Only one, $Y(4660)$, is remotely near a predicted 1^{--} $c\bar{c}$ state ($1\,^3D_1$). The $Y(4260)$ and $Y(4360)$ did not show up in inclusive hadronic cross section (R) measurements (Bai *et al.*, 2002), as would be expected of such states (there is no fine-grained R-scan data near $Y(4660)$).

A comparison of the measured $J/\psi\pi^+\pi^-$ and total hadronic cross sections in the $\sqrt{s} \simeq 4260$ MeV region yields a lower bound for $\Gamma(Y \to J/\psi\pi^+\pi^-)$>508 keV at 90% C.L., an order of magnitude higher than expectations for conventional vector charmonium states (Mo *et al.*, 2006). Charmonium would also feature dominant open charm decays, exceeding those of dipion transitions by a factor expected to be $\gtrsim$100, because such is the case for $\psi(3770)$ and $\psi(4160)$. As summarized in Table VIII, no such evidence has been found, significantly narrowing any window for either charmonia or, in some cases, quark-gluon hybrid interpretations. CLEO (Coan *et al.*, 2006) studied direct production of the $Y(4260)$ in e^+e^- collisions and identified the only non-$J/\psi\pi^+\pi^-$ decay modes seen

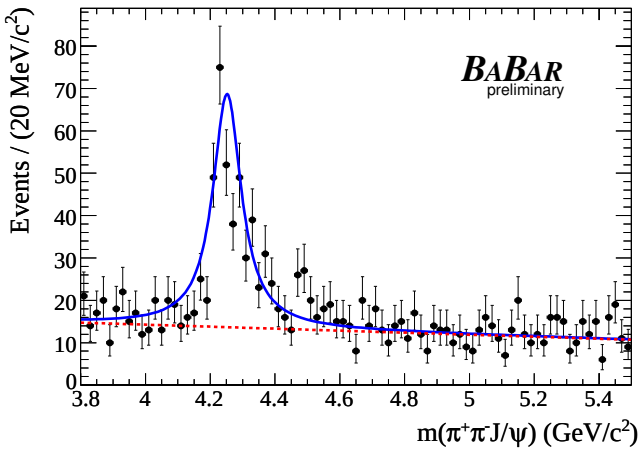


FIG. 81 The invariant mass of $J/\psi\pi^+\pi^-$ candidates produced in initial state radiation, $e^+e^- \to \gamma_{ISR}\, J/\psi\pi^+\pi^-$. Points with error bars represent data, and the curves show the fit (solid) to a signal plus a linear background (dashed) (Aubert *et al.*, 2008a).

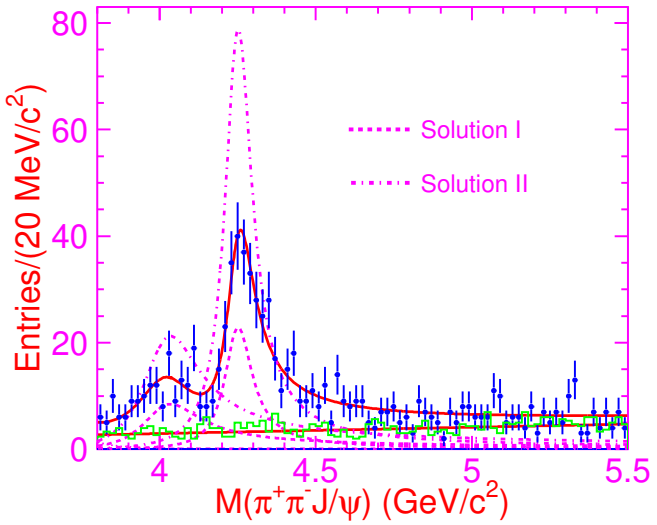


FIG. 82 The invariant mass of $J/\psi\pi^+\pi^-$ candidates produced in initial state radiation studied by Belle (Yuan *et al.*, 2007), with J/ψ-sidebands already subtracted, unlike Fig. 81. Points with error bars represent data, the solid curve shows the best fits to the data to two resonances including interference with a floating phase, and the dashed and dashed-dot curves show the two pair of individual resonance contributions for the two equally probable best-fit phases.

so far, $J/\psi\pi^0\pi^0$ and $J/\psi K^+K^-$, occuring at roughly half and one-sixth, respectively, of the $J/\psi\pi^+\pi^-$ rate. The $J/\psi K^+K^-$ decay mode was also observed by Belle (Yuan *et al.*, 2008).

Any interpretation for these vector states will not only have to explain their masses, widths, and manifest reluctance to materialize in open charm or unflavored light meson final states. The dipion invariant mass spectra exhibit curious structures, as seen for the $Y(4260)$

TABLE VI Measured properties of the $Y(4260) \to J/\psi\pi^+\pi^-$. The Belle (Wang *et al.*, 2007) single-resonance fit result is quoted to allow for comparison to the other two.

Quantity	Value	From (χ^2/ndf)
M (MeV/c^2)	$4259\pm8^{+2}_{-6}$	BABAR (Aubert *et al.*, 2008a)
	4263 ± 6	Belle (Yuan *et al.*, 2007)
	$4284^{+17}_{-16}\pm4$	CLEO (He *et al.*, 2006)
	4263 ± 5	Avg (1.8/2)
Γ (MeV)	$88\pm23^{+6}_{-4}$	BABAR (Aubert *et al.*, 2008a)
	126 ± 18	Belle (Yuan *et al.*, 2007)
	$73^{+39}_{-25}\pm5$	CLEO (He *et al.*, 2006)
	108 ± 15	Avg (2.4/2)
$\mathcal{B}\times\Gamma_{ee}$ (eV)	$5.5\pm1.0^{+0.8}_{-0.7}$	BABAR (Aubert *et al.*, 2008a)
	9.7 ± 1.1	Belle (Yuan *et al.*, 2007)
	$8.9^{+3.9}_{-3.1}\pm1.8$	CLEO (He *et al.*, 2006)
	8.0 ± 1.4	Avg (6.1/2)

TABLE VII Measured properties of the two enhancements found in the $\psi(2S)\pi^+\pi^-$ mass distribution, the $Y(4360)$ and $Y(4660)$. Liu *et al.* (Liu *et al.*, 2008) performed a binned maximum likelihood fit to the combined Belle and BABAR cross section distributions (Fig. 83).

Quantity	Value	From (χ^2/d.o.f.)
M (MeV/c^2)	4324 ± 24	BABAR (Aubert *et al.*, 2007a)
	$4361\pm9\pm9$	Belle (Wang *et al.*, 2007)
	4353 ± 15	Avg (1.8/1)
	$4355^{+\ 9}_{-10}\pm9$	Liu (Liu *et al.*, 2008)
Γ (MeV)	172 ± 33	BABAR (Aubert *et al.*, 2007a)
	$74\pm15\pm10$	Belle (Wang *et al.*, 2007)
	96 ± 42	Avg (6.8/1)
	$103^{+17}_{-15}\pm11$	Liu (Liu *et al.*, 2008)
M (MeV/c^2)	$4664\pm11\pm5$	Belle (Wang *et al.*, 2007)
	$4661^{+9}_{-8}\pm6$	Liu (Liu *et al.*, 2008)
Γ (MeV)	$48\pm15\pm3$	Belle (Wang *et al.*, 2007)
	$42^{+17}_{-12}\pm6$	Liu (Liu *et al.*, 2008)

in Fig. 84 (Aubert *et al.*, 2008a), for the $Y(4360)$ in Fig. 85(a) (Wang *et al.*, 2007), and for the $Y(4660)$ in Fig. 85(b) (Wang *et al.*, 2007). The first shows a distinctly non-phase-space double-hump structure which is qualitatively confirmed by Belle (Yuan *et al.*, 2007), the second exhibits a majority of events at higher masses, and the third indicates a quite dominant $f_0(980)$ component.

VII. SOME IMPLICATIONS FOR THEORY AND PERSPECTIVES

The progress in precision of the low energy data on $e^+e^- \to$ hadrons achieved recently due to ISR studies allows an update of the estimation of the hadronic con-

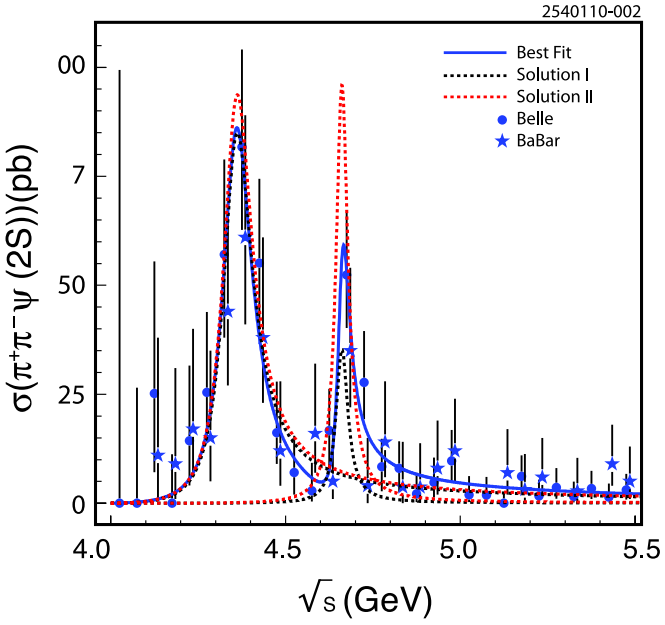


FIG. 83 From a binned maximum likelihood fit (Liu *et al.*, 2008) of combined Belle and BABAR data, the $\psi(2S)\pi^+\pi^-$ invariant-mass cross section as a function of $\sqrt{s}$. The solid circles and stars show the Belle and BABAR data, respectively. The solid curve shows the best fits to the data to two resonances including interference with a floating phase, and the dashed curves show the contributions of two pairs of individual resonances for the two equally probable best-fit phases.

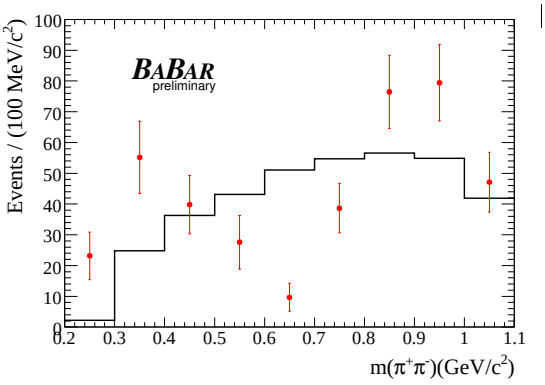


FIG. 84 The dipion invariant mass distribution on ISR-produced $Y(4260) \to J/\psi\pi^+\pi^-$ decays, where points represent data and the line histogram phase-space MC simulation (Aubert *et al.*, 2008a).

tribution to the muon anomalous magnetic moment to be performed. It is well known that the precision of the Standard Model prediction of this quantity is limited by the contributions from strong interactions. These are conventionally separated into a theory-driven light-by-light contribution, see a recent review in (Prades *et al.*, 2009), and two experiment-driven vacuum polarization contributions, the dominant lowest-order and higher-order parts. The lowest-order term can be calculated

TABLE VIII Upper limits at 90% C.L. on the ratios $\sigma(e^+e^- \to Y \to T)/\sigma(e^+e^- \to Y \to J/\psi\pi^+\pi^-)$ at $\sqrt{s} = 4.26$ GeV/c^2 (CLEO (Cronin-Hennessy *et al.*, 2009)) and $\mathcal{B}(Y \to T)/\mathcal{B}(Y \to J/\psi\pi^+\pi^-)$ (for $Y(4260)$) (BABAR (Aubert *et al.*, 2007e, 2009b) and Belle (Pakhlova *et al.*, 2007)), where T is an open charm final state.

T	$Y(4260)$
$D\bar{D}$	4.0 (Cronin-Hennessy *et al.*, 2009)
	7.6 (Aubert *et al.*, 2007e)
$D\bar{D}^*$	45 (Cronin-Hennessy *et al.*, 2009)
	34 (Aubert *et al.*, 2009b)
$D^*\bar{D}^*$	11 (Cronin-Hennessy *et al.*, 2009)
	40 (Aubert *et al.*, 2009b)
$D\bar{D}^*\pi$	15 (Cronin-Hennessy *et al.*, 2009)
	9 (Pakhlova *et al.*, 2007)
$D^*\bar{D}^*\pi$	8.2 (Cronin-Hennessy *et al.*, 2009)
$D_s\bar{D}_s$	1.3 (Cronin-Hennessy *et al.*, 2009)
$D_s\bar{D}_s^*$	0.8 (Cronin-Hennessy *et al.*, 2009)
$D_s^*\bar{D}_s^*$	9.5 (Cronin-Hennessy *et al.*, 2009)

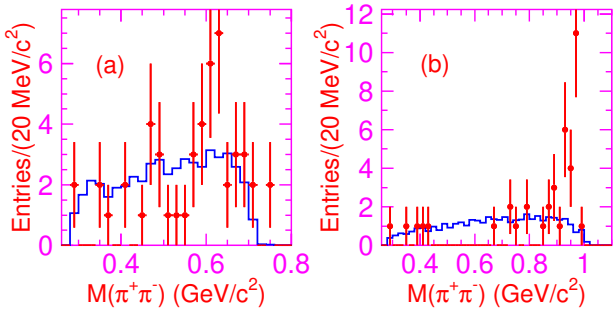


FIG. 85 The dipion invariant mass distribution on ISR-produced (a) $Y(4360) \to \psi(2S)\pi^+\pi^-$ and (b) $Y(4660) \to \psi(2S)\pi^+\pi^-$, where points represent data and the line histogram phase-space MC simulation (Wang *et al.*, 2007).

from a dispersion integral (Bouchiat and Michel, 1961; Gourdin and de Rafael, 1969) in which the integrand contains a combination of experimental data on cross sections of $e^+e^- \to$ hadrons and perturbative QCD. The integral ranges from the threshold of hadron production, i.e., from the $\pi^0\gamma$ threshold to infinity:

$$a_\mu^{\rm had,LO} = \left(\frac{\alpha m_\mu}{3\pi}\right)^2 \int_{m_\pi^2}^{\infty} ds\, \frac{R(s)\,\hat{K}(s)}{s^2}. \qquad (20)$$

The function $\hat{K}(s)$ in the integration kernel is rather smooth, whereas a factor $1/s^2$ emphasizes the low-energy part of the spectrum. Of particular importance is the process $e^+e^- \to \pi^+\pi^-(\gamma)$, which provides about 73% of the lowest-order hadronic contribution and about 62% of its total quadratic error.

In most cases new ISR results from BABAR are consistent with previous measurements and have comparable or better accuracy. However, not always these results

Process	Before BABAR	With BABAR
$\pi^+\pi^-\pi^0$	2.45 ± 0.26	3.25 ± 0.09
$2\pi^+2\pi^-$	14.20 ± 0.90	13.09 ± 0.44
$3\pi^+3\pi^-$	0.10 ± 0.10	0.11 ± 0.02
$2\pi^+2\pi^-2\pi^0$	1.42 ± 0.30	0.89 ± 0.09

TABLE IX The contribution of some multipion processes to $a_\mu^{\rm had,LO}$ integrated from threshold to 1.8 GeV for the measurements before BABAR and including the new BABAR results. For the $\pi^+\pi^-\pi^0$ final state the contribution of the ω and ϕ mesons is excluded. All values are in units of 10^{-10}.

agree with the corresponding old datasets. For example, from Fig. 23 discussed in Ch. 3 it is clear that the cross section of the process $e^+e^-\to\pi^+\pi^-\pi^0$ obtained by BABAR (Aubert *et al.*, 2004b) is consistent with that of SND (Achasov *et al.*, 2002) below $\sqrt{s}$ = 1.4 GeV, but is much higher than that at DM2 (Antonelli *et al.*, 1992) above this energy. The energy dependence of the cross section observed by DM2 is also inconsistent with other measurements (see the discussion of this problem in Ref. (Achasov *et al.*, 2002)) and the existence of the rather well established $\omega(1420)$ and $\omega(1650)$ resonances. The contribution of this process to $a_\mu^{\rm had,LO}$, which was equal to $(2.45\pm0.26)\cdot10^{-10}$ before BABAR (Davier *et al.*, 2003b), becomes $(3.25 \pm 0.09) \cdot 10^{-10}$ after the new results are taken into account (Davier, 2007). For the process $e^+e^-\to 2\pi^+2\pi^-$, which cross section is one of the largest above 1 GeV, the new BABAR measurement (Aubert *et al.*, 2005b) is in good agreement with the older results and after taking them into account the precision of the corresponding contribution improves by a factor of two. Another example is the measurement of two six-pion final states (Aubert *et al.*, 2006b). In Figs. 86 and 87 we compare the cross sections from BABAR with those in older measurements. It is clear that the improvement is dramatical because older measurements were too imprecise to make a reasonable prediction. We summarize the discussed contributions to $a_\mu^{\rm had,LO}$ integrated from threshold to 1.8 GeV for the measurements before BABAR (see the references in Ref. (Davier *et al.*, 2003b)) and with BABAR in Table IX (Davier, 2007).

The calculation using all multibody modes measured by BABAR (Aubert *et al.*, 2004b, 2005b, 2006b, 2007c) together with the relevant older measurements (for a complete list of references see Ref. (Davier *et al.*, 2003b)) gives for the contribution of hadronic continuum from threshold to 1.8 GeV the value $(54.2 \pm 1.9) \cdot 10^{-10}$. It is consistent with the result of the older calculation (Davier *et al.*, 2003b), $(55.0 \pm 2.6) \cdot 10^{-10}$, and more precise.

A very important step in the calculations of $a_\mu^{\rm had,LO}$ has been recently made in Ref. (Davier *et al.*, 2010a), which for the first time took into account the BABAR measurement of the reaction $e^+e^-\to\pi^+\pi^-$ (Aubert *et al.*, 2009a) and finally in Ref. (Davier *et al.*, 2011), which

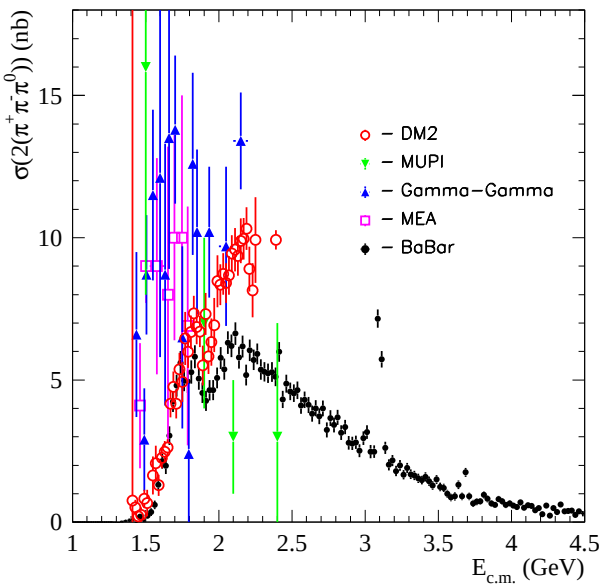


FIG. 86 The cross section of the process $e^+e^-\to 2\pi^+2\pi^-2\pi^0$ (Aubert *et al.*, 2006b; Bacci *et al.*, 1981; Baldini *et al.*, 1988; Cosme *et al.*, 1979; Esposito *et al.*, 1981).

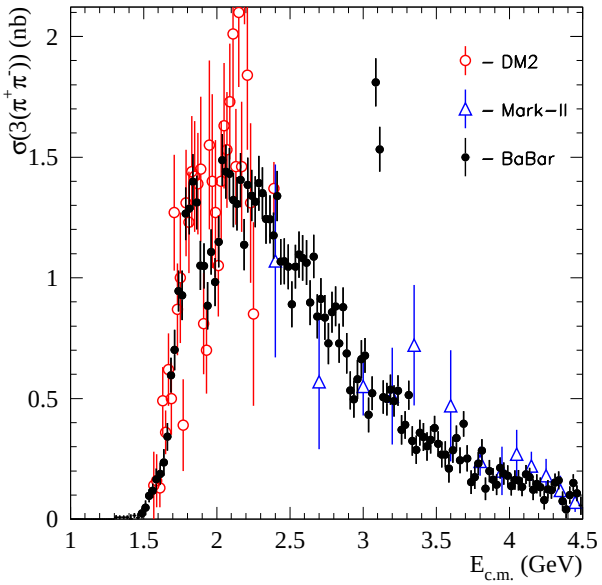


FIG. 87 The cross section of the process $e^+e^-\to 3\pi^+3\pi^-$ (Aubert *et al.*, 2006b; Baldini *et al.*, 1988; Jean-Marie *et al.*, 1976).

also accounted for the KLOE results on the $\pi^+\pi^-$ final state (Ambrosino *et al.*, 2009, 2011). It uses the whole set of experimental data in the energy range up to 1.8 GeV, the region dominated by hadronic resonances, and perturbative QCD for the contribution of the quark continuum beyond that energy. In particular, they modify the treatment of the $\omega(782)$ and $\phi(1020)$ res-

Experiment	$a_\mu^{\rm had,LO}[\pi\pi]$ $[10^{-10}]$	$\mathcal{B}_{\rm CVC}$ [%]
BABAR	514.1 ± 3.8 (1.00)	$25.15 \pm 0.18 \pm 0.22$ (1.00)
KLOE	503.1 ± 7.1 (0.97)	$24.56 \pm 0.26 \pm 0.22$ (0.92)
CMD2	506.6 ± 3.9 (0.89)	$24.96 \pm 0.21 \pm 0.22$ (0.96)
SND	505.1 ± 6.7 (0.94)	$24.82 \pm 0.30 \pm 0.22$ (0.91)

TABLE X Estimated $a_\mu^{\rm had,LO}[\pi\pi]$ and $\mathcal{B}_{\rm CVC}$ contributions from the e^+e^- data (Davier *et al.*, 2011).

onances using the data from Ref. (Aubert *et al.*, 2004b), and include preliminary data of BABAR on $e^+e^- \to \pi^+\pi^-2\pi^0$ (Druzhinin, 2007). They also use isospin invariance to estimate the contributions from several unmeasured final states with six pions and $K\bar{K}(n\pi)$ relating them to those of known channels. For other channels they refer to earlier calculations (Davier *et al.*, 2003a,b; Davier, 2007).

Contributions to $a_\mu^{\rm had,LO}[\pi\pi]$ from the individual $\pi^+\pi^-$ cross sections measured at BABAR (Aubert *et al.*, 2009a), KLOE (Ambrosino *et al.*, 2009, 2011), CMD2 (Akhmetshin *et al.*, 2004a, 2007), and SND (Achasov *et al.*, 2006) are given in the middle column of Table X (Davier *et al.*, 2011). In the right column we list the corresponding CVC predictions for the $\tau^\pm \to \pi^\pm\pi^0\nu_\tau$ branching fraction corrected for isospin-breaking effects (Davier *et al.*, 2010b). Here the first error is experimental and the second estimates the uncertainty in the isospin-breaking corrections. For each experiment, all available data in the energy range from threshold to 1.8 GeV (m_τ for $\mathcal{B}_{\rm CVC}$) are used, and the missing part is completed by the combined e^+e^- data.

The average of the four separate results gives $a_\mu^{\rm had,LO}[\pi\pi] = (507.8 \pm 2.8_{\rm tot}) \cdot 10^{-10}$ (Davier *et al.*, 2011). The comparison with their previous result (Davier *et al.*, 2010b), $a_\mu^{\rm had,LO}[\pi\pi] = (503.5 \pm 3.5_{\rm tot}) \cdot 10^{-10}$, shows that the inclusion of the new BABAR data significantly increases the central value of the integral. For the higher-order hadronic contributions to $a_\mu^{\rm had,LO}$, which are also estimated based on e^+e^-data, there is a slight gain in accuracy from $-9.79 \pm 0.08_{\rm exp} \pm 0.03_{\rm rad}$ (Hagiwara *et al.*, 2007) to $-9.79 \pm 0.06_{\rm exp} \pm 0.03_{\rm rad}$ (Hagiwara *et al.*, 2011).

A compilation of recent results for a_μ, from which the central value of the experimental average (Bennett *et al.*, 2006) has been subtracted, is given in Fig. 88. The shaded vertical band indicates the experimental error. The SM predictions are taken from: HMNT 07 (Hagiwara *et al.*, 2007), JN 09 (Jegerlehner and Nyffeler, 2009), Davier et al. 09/1 (τ-based) (Davier *et al.*, 2010b), Davier et al. 09/2 (e^+e^--based, with BABAR $\pi^+\pi-$ data) (Davier *et al.*, 2010a), HLMNT 11 (e^+e^--based, with BABAR and KLOE $\pi^+\pi^-$ data) (Hagiwara *et al.*, 2011), DHMZ 10 (τ and e^+e^-) (Davier *et al.*, 2011), BDDJ 11 ((τ and e^+e^-) (Benayoun *et al.*, 2011).

There have been only a few tests of CVC based on the new data. The most interesting final state is of course that with two pions, where a serious discrepancy be-

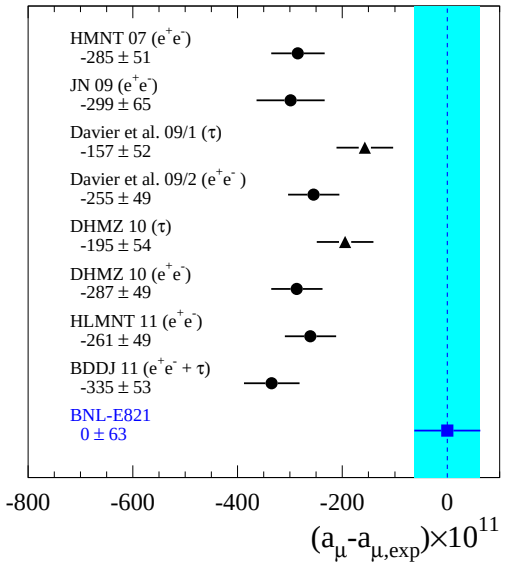


FIG. 88 Compilation of recent results for a_μ.

tween the $e^+e^-$and τ data was reported (Davier *et al.*, 2003a,b). The results of the most recent tests in this channel (Davier *et al.*, 2010b, 2011) are based on the reevaluation of isospin-breaking corrections. The predictions for the branching fraction of $\tau^\pm \to \pi^\pm\pi^0\nu_\tau$ shown in Table X. can be compared to the world average value of $(25.51 \pm 0.09)\%$ (Nakamura *et al.*, 2010). Although the difference between the CVC prediction and the experimental value is less significant than previously (Davier *et al.*, 2003b; Davier, 2007), it is still substantial for all groups but BABAR. A new approach to the problem was suggested very recently in Ref. (Jegerlehner and Szafron, 2011), where the $\rho - \gamma$ mixing was properly taken into account. The CVC prediction for the branching fraction to two pions is $(25.20 \pm 0.17 \pm 0.28)\%$ in good agreement with the direct measurement. Finally, Ref. (Benayoun *et al.*, 2011) reports consistent results on e^+e^- and τ in the 2π channel and obtains a theoretical prediction for a_μ, which is lower than the experimental value by 4.1σ.

One more test of CVC that included recent ISR results from BABAR has been performed in Ref. (Cherepanov and Eidelman, 2009). The authors use CVC together with the data on $e^+e^- \to \eta\pi^+\pi^-$ and $e^+e^- \to \eta'\pi^+\pi^-$ to estimate the branching fraction of the corresponding τ decays. For the former final state the estimate based on the older data (Akhmetshin *et al.*, 2000; Antonelli *et al.*, 1988; Delcourt *et al.*, 1982; Druzhinin *et al.*, 1986) predicts for the branching fraction $(0.132 \pm 0.016)\%$, somewhat smaller but not incompatible with $(0.165 \pm 0.015)\%$ obtained from the BABAR data (Aubert *et al.*, 2007c). The average of the two gives the CVC prediction of $(0.150 \pm 0.016)\%$, in good agreement with the new world

average $\mathcal{B}(\tau^- \to \eta\pi^-\pi^0\nu_\tau) = (0.139 \pm 0.010)\%$ that uses the new presise measurement at Belle (Inami *et al.*, 2009). For the $\mathcal{B}(\tau^- \to \eta'\pi^-\pi^0\nu_\tau)$ they give an upper limit of $< 3.2 \cdot 10^{-5}$ at 90% CL, which is a factor of 2.5 more restrictive than the upper limit based on the only existing measurement by CLEO: $< 8 \cdot 10^{-5}$ (Bergfeld *et al.*, 1997).

There are two recent evaluations of $\Delta\alpha^{(5)}_{\rm had}(M_Z^2)$, the hadronic contribution to the running α from five flavors (Davier *et al.*, 2011; Hagiwara *et al.*, 2011). In Ref. (Hagiwara *et al.*, 2011) a data set of e^+e^-cross sections includes multibody data from BABAR and 2π data from KLOE and the calculation gives the value 0.02760 ± 0.00015, slightly higher and significantly more accurate than the previously accepted value 0.02758 ± 0.00035 (Burkhardt and Pietrzyk, 2005). The estimation performed in Ref. (Davier *et al.*, 2011) additionally uses the BABAR data on the $\pi\pi$ final state and perturbative QCD between 1.8 and 3.7 GeV and gives an even more precise value 0.02749 ± 0.00010.

VIII. CONCLUSIONS

Successful experiments at high-luminosity e^+e^- colliders (ϕ- and B-factories) opened a new era in a study of e^+e^- annihilation into hadrons at low energies using a novel method of initial-state radiation usually referred to as ISR or radiative return.

Modern detectors operating at these factories which collected unprecedentally high integrated luminosity allow this method to compete with direct e^+e^- experiments.

A lot of new data on the cross sections of e^+e^- annihilation into hadrons were obtained using ISR, first of all, on the production of mesons from threshold of their production $\sim 2m_\pi$ to the c.m. energy of about 4-5 GeV. More than 30 processes have been studied in which mesons and hadronic resonances were produced, many of them for the first time.

Valuable information on the particles with mass of about a few GeV has been obtained, primarily on excited vector mesons, radial and/or orbital excitations. Parameters of vector charmonia were investigated, new data on more than 40 decay channels were obtained, many decays observed for the first time.

New data on production cross sections were obtained for various baryons: proton, Λ, Σ^0 and Λ_c hyperon, opening new possibilities for testing form factor models.

New states ($\rho(1900)$, $Y(2175)$, $Y(4260)$, $Y(4320)$ ...), some of them with presumably exotic quark structure, have been discovered. Their nature is not yet established and widely discussed.

New values of the cross sections obtained using ISR can be used for more precise predictions of the muon anomalous magnetic moment, running fine- structure constant at the Z boson mass, tests of CVC and many other theoretical models.

Only part of the available ISR data sample has been processed, e.g., for BABAR it is about 1/3, analysis is in progress. Belle has only started a corresponding data processing.

If existing projects of Super B-Factories are approved, prospects of reaching an integrated luminosity by a factor of 30-100 exceeding that today appear. Such experiments will improve accuracy for many processes which studies are now statistically limited.

Acknowledgments

The authors are grateful to Vera Luth for the idea of this review. We are indebted to our colleagues from the BABAR and Belle Collaborations for many years of fruitful work. Thanks are also due to Brian Heltsley from CLEO and Graziano Venanzoni from KLOE for valuable comments.

This work was supported in part by the grants RFBR 10-02-00695, 11-02-00112, 11-02-00558, and the DFG grant GZ 436 RUS 113/769/0-3.

References

Abashian, A., *et al.* [Belle Collaboration], 2002, Nucl. Instr. and Meth. A **479**, 117.

Ablikim, M., *et al.* [BES Collaboration], 2005, Phys. Lett. B **630**, 14.

Ablikim, M., *et al.* [BES Collaboration], 2008, Phys. Lett. B **660**, 315.

Achasov, M.N., *et al.* [SND Collaboration], 2002, Phys. Rev. D **66**, 032001.

Achasov, M.N., *et al.* [SND Collaboration], 2003, J. Exp. Theor. Phys. **96**, 789.

Achasov, M.N., *et al.* [SND Collaboration], 2006, J. Exp. Theor. Phys. **103**, 380.

Actis, S., *et al.*, 2010, Eur. Phys. J. C **66**, 585.

Adam, N.E., *et al.* [CLEO Collaboration], 2006, Phys. Rev. Lett. **96**, 082004.

Adams, G.S., *et al.* [CLEO Collaboration], 2006, Phys. Rev. D **73**, 051103.

Agostinelli, S., *et al.* [GEANT4 Collaboration], 2003, Nucl. Instr. Meth. A **506**, 250.

Akhmetshin, R.R., *et al.* [CMD-2 Collaboration], 1999, Phys. Lett. B **466**, 392.

Akhmetshin, R.R., *et al.* [CMD-2 Collaboration], 2000, Phys. Lett. B **489**, 125.

Akhmetshin, R.R., *et al.* [CMD-2 Collaboration], 2004a, Phys. Lett. B **578**, 285.

Akhmetshin, R.R., *et al.* [CMD-2 Collaboration], 2004b, Phys. Lett. B **595**, 101.

Akhmetshin, R.R., *et al.* [CMD-2 Collaboration], 2007, Phys. Lett. B **648**, 28.

Alemany, R., M. Davier, and A. Höcker, 1998, Eur. Phys. J. C **2**, 123.

Aloisio, A., *et al.* [KLOE Collaboration], 2005, Phys. Lett. B **606**, 12.

Ambrogiani, M., *et al.* [E835 Collaboration], 1999, Phys. Rev. D **60**, 032002.

Ambrosino, F., *et al.* [KLOE Collaboration], 2009, Phys. Lett. B **670**, 285.

Ambrosino, F., *et al.* [KLOE Collaboration], 2011, Phys. Lett. B **700**, 102.

Amsler, C., *et al.* [Particle Data Group], 2008, Phys. Lett. B **667**, 1.

Antonelli, A., *et al.* [DM2 Collaboration], 1988, Phys. Lett. B **212**, 133.

Antonelli, A., *et al.* [DM2 Collaboration], 1992, Z. Phys. C **56**, 15.

Antonelli, A., *et al.* [FENICE Collaboration], 1996, Phys. Lett. B **365**, 427.

Antonelli, A., *et al.* [FENICE Collaboration], 1998, Nucl. Phys. B **517**, 3.

Arbuzov, A.B., *et al.*, 1998, JHEP **9812**, 009.

Armstrong, T.A., *et al.* [E760 Collaboration], 1993, Phys. Rev. Lett. **70**, 1212.

Aubert, B., *et al.* [BABAR Collaboration], 2002, Nucl. Instr. Meth. A **479**, 1.

Aubert, B., *et al.* [BABAR Collaboration], 2004a, Phys. Rev. D **69**, 011103.

Aubert, B., *et al.* [BABAR Collaboration], 2004b, Phys. Rev. D **70**, 072004.

Aubert, B., *et al.* [BABAR Collaboration], 2005a, Phys. Rev. Lett. **95**, 142001.

Aubert, B., *et al.* [BABAR Collaboration], 2005b, Phys. Rev. D **71**, 052001.

Aubert, B., *et al.* [BABAR Collaboration], 2006a, Phys. Rev. D **73**, 012005.

Aubert, B., *et al.* [BABAR Collaboration], 2006b, Phys. Rev. D **73**, 052003.

Aubert, B., *et al.* [BABAR Collaboration], 2007a, Phys. Rev. Lett. **98**, 212001.

Aubert, B., *et al.* [BABAR Collaboration], 2007b, Phys. Rev. D **76**, 012008.

Aubert, B., *et al.* [BABAR Collaboration], 2007c, Phys. Rev. D **76**, 092005, [Erratum-ibid, 2008, **77**, 119902].

Aubert, B., *et al.* [BABAR Collaboration], 2007d, Phys. Rev. D **76**, 092006.

Aubert, B., *et al.* [BABAR Collaboration], 2007e, Phys. Rev. D **76**, 111105.

Aubert, B., *et al.* [BABAR Collaboration], 2008a, eprint arXiv:0808.1543 [hep-ex].

Aubert, B., *et al.* [BABAR Collaboration], 2008b, Phys. Rev. D **77**, 092002.

Aubert, B., *et al.* [BABAR Collaboration], 2009a, Phys. Rev. Lett. **103**, 231801.

Aubert, B., *et al.* [BABAR Collaboration], 2009b, Phys. Rev. D **79**, 092001.

Aulchenko, V. M. *et al.* [CMD-2 Collaboration], 2005, JETP Lett. **82**, 743.

Aulchenko, V. M. *et al.* [CMD-2 Collaboration], 2006, JETP Lett. **84**, 413.

Bacci, C., *et al.* [$\gamma\gamma$2 Collaboration], 1980, Phys. Lett. B **95**, 139.

Bacci, C., *et al.* [$\gamma\gamma$2 Collaboration], 1981, Nucl. Phys. B **184**, 31.

Bai, J.Z., *et al.* [BES Collaboration], 1998, Phys. Rev. D **58**, 092006.

Bai, J.Z., *et al.* [BES Collaboration], 2002, Phys. Rev. Lett. **88**, 101802.

Bai, J.Z., *et al.* [BES Collaboration], 2004, Phys. Rev. D **70**, 012005.

Baier, V.N., and V. S. Fadin, 1968, Phys. Lett. B **27**, 223.

Baier, V.N., and V. A. Khoze, 1965, Sov. Phys. JETP **21**, 1145.

Baldini, R., *et al.* [DM2 Collaboration], 1988, in Proceedings of the "Fenice" Workshop, Frascati.

Baldini, R., *et al.*, 2009, Eur. Phys. J. A **39**, 315.

Barberio, E., B. van Eijk, and Z. Was, 1991, Comput. Phys. Commun. **66**, 115.

Bardin, G., *et al.* [PS170 Collaboration], 1994, Nucl. Phys. B **411**, 3.

Barnes, T., S. Godfrey, and E. S. Swanson, 2005, Phys. Rev. D **72**, 054026.

Benayoun, M., *et al.*, 1999, Mod. Phys. Lett. **14**, 2605.

Benayoun, M., *et al.*, 2011, arXiv:1106.1315 [hep-ph].

Bennett, G.W., *et al.* [E821 Collaboration], 2006, Phys. Rev. D **73**, 072003.

Bergfeld, T., *et al.* [CLEO Collaboration], 1997, Phys. Rev. Lett. **79**, 2406.

Binner, S., J.H. Kühn, and K. Melnikov, 1999, Phys. Lett. B **459**, 279.

Bisello, D., *et al.* [DM1 Collaboration], 1981, Phys. Lett. B **107**, 145.

Bisello, D., *et al.* [DM2 Collaboration], 1983, Nucl. Phys. B **224**, 379.

Bisello, D., *et al.* [DM2 Collaboration], 1989, Phys. Lett. B **220**, 321.

Bisello, D., *et al.* [DM2 Collaboration], 1990, Z. Phys. C **48**, 23.

Bisello, D., *et al.* [DM2 Collaboration], 1991a, Nucl. Phys. Proc. Suppl. **21**, 111.

Bisello, D., *et al.* [DM2 Collaboration], 1991b, Z. Phys. C **52**, 227.

Bityukov, S.I., *et al.*, 1987, Phys. Lett. B **188**, 383.

Bonneau, G., and F. Martin, 1971, Nucl. Phys. B **27**, 381.

Bouchiat, C., and L. Michel, 1961, J. Phys. Radium **22**, 121.

Brambilla, H., *et al.* [QWG], 2011, Eur. Phys. J. C **71**, 1515.

Brandelik, R., *et al.* [DASP Collaboration], 1978, Phys. Lett. B **76**, 361.

Buon, J., *et al.* [DM1 Collaboration], 1982, Phys. Lett. B **118**, 221.

Burkhardt, H., *et al.*, 1989, Z. Phys. C **43**, 497.

Burkhardt, H., and B. Pietrzyk, 2005, Phys. Rev. D **72**, 057501.

Caffo, M., H. Czyż, and E. Remiddi, 1994, Phys. Lett. B **327**, 369.

Caffo, M., H. Czyż, and E. Remiddi, 1997, Nuovo Cim. A **110**, 515.

Castellano, M., *et al.*, 1973, Nuovo Cim. A **14**, 1.

Cherepanov, V.A., and S.I. Eidelman, 2009, JETP Lett. **89**, 429.

Chernyak, V.L., and A. R. Zhitnitsky, 1977, JETP Lett. **25**, 510.

Chernyak, V.L., *et al.*, 1989, Z. Phys. C **42**, 569.

Coan, T.E., *et al.* [CLEO Collaboration], 2006, Phys. Rev. Lett. **96**, 162003.

Cordier, A., *et al.* [DM1 Collaboration], 1981, Phys. Lett. B **106**, 155.

Cordier, A., *et al.* [DM1 Collaboration], 1982a, Phys. Lett. B **109**, 129.

Cordier, A., *et al.* [DM1 Collaboration], 1982b, Phys. Lett. B **110**, 335.

Cosme, G., *et al.* [M3N Collaboration], 1979, Nucl. Phys. B **152**, 215.

Cronin-Hennessy, D., *et al.* [CLEO Collaboration], 2009, Phys. Rev. D **80**, 072001.

Czyż, H., and J. H. Kühn, 2001, Eur. Phys. J. C **18**, 497.
Czyż, H., *et al.*, 2003, Eur. Phys. J. C **27**, 563.
Czyż, H., *et al.*, 2004, Eur. Phys. J. C **35**, 527.
Czyż, H., A. Grzelinska, and J. H. Kühn, 2007, Phys. Rev. D **75**, 074026.
D'Agostini, G., 1995, Nucl. Instrum. Meth. A **362**, 487.
Datta, A., and P.J. O'Donnell, 2003, Phys. Lett. B **567**, 263.
Davier, M., *et al.*, 2003a, Eur. Phys. J. C **27**, 497.
Davier, M., *et al.*, 2003b, Eur. Phys. J. C **31**, 503.
Davier, M., 2007, Nucl. Phys. B (Proc. Suppl.) **169**, 288.
Davier, M., *et al.*, 2010a, Eur. Phys. J. C **66**, 1.
Davier, M., *et al.*, 2010b, Eur. Phys. J. C **66**, 127.
Davier, M., *et al.*, 2011, Eur. Phys. J. C **71**:1515.
del Amo Sanchez, P., *et al.* [BABAR Collaboration], 2010, Phys. Rev. D **82**, 052004.
Delcourt, B., *et al.* [DM1 Collaboration], 1979, Phys. Lett. B **86**, 395.
Delcourt, B., *et al.* [DM1 Collaboration], 1982, Phys. Lett. B **113**, 93.
Dmitriev, V.F., and A. I. Milstein, 2007, Phys. Lett. B **658**, 13.
Dolinsky, S.I., *et al.* [ND Collaboration], 1991, Phys. Rept. **202**, 99.
Druzhinin, V.P., *et al.* [ND Collaboration], 1986, Phys. Lett. B **174**, 115.
Druzhinin, V.P., 2007, eprint arXiv:0710.3455 [hep-ex].
Dubnickova, A.Z., S. Dubnicka, and M. P. Rekalo, 1996, Nuovo Cim. A **109**, 241.
Eichten, E.J., *et al.*, 1980, Phys. Rev. D **21**, 203.
Eichten, E.J., K. Lane and C. Quigg, 2006, Phys. Rev. D **73**, 014014, [Erratum-ibid. 2006, D **73**, 079903 (2006)].
Eichten, E.J., *et al.*, 2008, Rev. Mod. Phys. **80**, 1161.
Eidelman, S.I., and V.N. Ivanchenko, 1991, Phys. Lett. B **257**, 437.
Eidelman, S., and F. Jegerlehner, 1995, Z. Phys. C **67**, 585.
Eidelman, S., *et al.* [Particle Data Group], 2004, Phys. Lett. B **592**, 1.
Esposito, B., *et al.* [MEA Collaboration], 1981, Lett. Nuovo Cim. **31**, 445.
Frabetti, P.L., *et al.* [FOCUS Collaboration], 2000, Phys. Lett. B **514**, 240.
Franzini, P., and M. Moulson, 2006, Annual Review of Nuclear and Particle Science, **56**, 207.
Gomez-Avila, S., M. Napsuciale, and E. Oset, 2009, Phys.Rev. D **79**, 034018.
Gourdin, M., and E. de Rafael, 1969, Nucl. Phys. B **10**, 667.
Hagiwara, K., *et al.*, 2003, Phys. Lett. B **557**, 69.
Hagiwara, K., *et al.*, 2007, Phys. Lett. B **649**, 173.
Hagiwara, K., *et al.*, 2011, J. Phys. G **38**, 085003.
He, Q., *et al.* [CLEO Collaboration], 2006, Phys. Rev. D **74**, 091104.
Inami, K., *et al.* [Belle Collaboration], 2009, Phys. Lett. B **672**, 209.
Jean-Marie, B., *et al.* [Maek-II Collaboration], 1976, Preprint SLAC-PUB-1711.
Jegerlehner, F., and A. Nyffeler, 2009, Phys. Rept. **477**, 1.
Jegerlehner, F., and R. Szafron, 2011, Eur. Phys. J. C **71**:1332.
Kardapoltzev, L.V., 2007, Bachelor's thesis, Novosibirsk State University (unpublished).
Kawamoto, N., and A.I. Sanda, 1978, Phys. Lett. B **76**, 446.
Khoze, V.A., *et al.*, 2001, Eur. Phys. J. C **18**, 481.
Khoze, V.A., *et al.*, 2002, Eur. Phys. J. C **25**, 199.
Konchatnij, M.I., and N.P. Merenkov, 1999, JETP Lett. **69**, 811.
Kuraev, E.A., and V.S. Fadin, 1985, Sov. J. Nucl. Phys. **41**, 466.
Kurdadze, L.M., *et al.* [Olya Collaboration], 1984, Sov. J. Nucl. Phys. **40**, 286.
Kurdadze, L.M., *et al.* [Olya Collaboration], 1986, JETP Lett. **43**, 643.
Kurdadze, L.M., *et al.* [Olya Collaboration], 1988, JETP Lett. **47**, 512.
Kurokawa, S., and E. Kikutani, 2003, Nucl. Instr. and Meth. A **499**, 1, and other papers included in this volume.
J. P. Lees, J. P., *et al.* [The BABAR Collaboration], 2011, eprint arXiv:1103.3001 [hep-ex].
Liu, Z.Q., X.S. Qin, and C.Z. Yuan, 2008, Phys. Rev. D **78**, 014032.
Malaescu, B., 2009, eprint arXiv:0907.3791 [physics.data-an].
Mo, X.H., *et al.*, 2006, Phys. Lett. B **640**, 18.
Muller, S. E., [KLOE Collaboration], 2009, talk given at International Workshop on e+e- collisions from phi to psi (PHIPSI09), October 13-16, 2009, Beijing, China.
Nakamura, K., *et al.*, 2010, J. Phys. G **37**, 075021.
Napsuciale, M., *et al.*, 2007, Phys.Rev. D **76**, 074012.
Osterheld, A., *et al.* [Crystal Ball Collaboration], 1986, SLAC-PUB-4160.
Pakhlova, G., *et al.* [Belle Collaboration], 2007, Phys. Rev. Lett. **98**, 092001.
Pakhlova, G., *et al.* [Belle Collaboration], 2008a, Phys. Rev. D **77**, 011103.
Pakhlova, G., *et al.* [Belle Collaboration], 2008b, Phys. Rev. Lett. **100**, 062001.
Pakhlova, G., *et al.* [Belle Collaboration], 2008c, Phys. Rev. Lett. **101**, 172001.
Pakhlova, G., *et al.* [Belle Collaboration], 2009, Phys. Rev. D **80**, 091101.
Pakhlova, G.V., P.N. Pakhlov, and S.I. Eidelman, 2010, Physics–Uspekhi **53**, 219.
Pakhlova, G., *et al.* [Belle Collaboration], 2011, Phys. Rev. D **83**, 011101.
Pedlar, T.K., *et al.* [CLEO Collaboration], 2005, Phys. Rev. Lett. **95**, 261803.
http://ific.uv.es/∼rodrigo/phokhara/
Prades, J., E. de Rafael and A. Vainshtein, 2009, eprint arXiv:0901.0306 [hep-ph].
Renard, F.M., 1981, Basics of Electron Positron Collisions, Editions Frontieres, Gif sur Yvette, France.
Rodrigo, G., *et al.*, 2001, Eur. Phys. J. C **22**, 81.
Rodrigo, G., *et al.*, 2002, Eur. Phys. J. C **24**, 71.
Seeman, J.T., *et al.*, 2001, SLAC-PRPRINT-2001-040.
Seth, K.K., 2005, Phys. Rev. D **72**, 017501.
Siegrist, J.L., *et al.* [MARK-I Collaboration], 1976, Phys. Rev. Lett. **36**, 700.
Shen, C.P., *et al.* [Belle Collaboration], 2009, Phys. Rev. D **80**, 031101.
Shifman, M.A., A.I. Vainshtein, and V.I. Zacharov, 1979, Nucl. Phys. B **147**, 385.
Swanson, E.S., 2006, Phys. Rept. **429**, 243.
Thacker, H.B., and J.J. Sakurai, 1971, Phys. Lett. B **36**, 103.
Tsai, Y.S., 1971, Phys. Rev. D **4**, 2821, [Erratum-ibid. 1976, D **13**, 771].
Tzara, C., 1970, Nucl. Phys. B **18**, 246.
Vasserman, I.B., *et al.* [ND Collaboration], 1988, Sov. J. Nucl. Phys. **47** 1035.
Wang, W.F. [BABAR Collaboration], 2009, talk given at International Workshop on e+e- collisions from phi to psi

(PHIPSI09), October 13-16, 2009, Beijing, China.
Wang, X.L., *et al.* [Belle Collaboration], 2007, Phys. Rev. Lett. **99**, 142002.
Yao, W.M., *et al.* [Particle Data Group], 2006, J. Phys. G **33**, 1.
Yuan, C.Z., *et al.* [Belle Collaboration], 2007, Phys. Rev. Lett. **99**, 182004.
Yuan, C.Z., *et al.* [Belle Collaboration], 2008, Phys. Rev. D **77**, 011105.